LARGE CURRENT TERAHERTZ ANTENNA FEEDING USING MICROSTRIP COMBINERS INTEGRATED WITH ARRAYED UNI-TRAVELLING CARRIER PHOTODIODES

サリ, フセイン

LARGE CURRENT TERAHERTZ ANTENNA FEEDING USING MICROSTRIP COMBINERS INTEGRATED WITH ARRAYED UNI-TRAVELLING CARRIER PHOTODIODES

A Thesis Submitted to

The Graduate School of Information Science and Electrical Engineering of

Kyushu University

In Partial Fulfilment of the Requirements for the Degree of Doctor of Philosophy in Electrical and Electronic Engineering, Department of Electrical and Electronic Engineering

By

SSALI HUSSEIN

Supervisor: Prof. Kazutoshi Kato

July 2024

Fukuoka

THESIS COMMITTEE:

1. Prof. Haruichi Kanaya
2. Prof. Osamu Muta
3. Prof. Kazutoshi Kato

ACKNOWLEDGEMENT

I thank the Almighty for enabling me to accomplish this piece of work. I express my earnest appreciation to my supervisor Prof. Kazutoshi Kato for his guidance, mentoring and selfless support throughout my research. I'm grateful to my thesis committee and co-supervisors, Prof. Haruichi Kanaya, Prof. Osamu Muta and Dr. Tadao Ishibashi for their guidance and valuable insights, and to Assistant Professors, Yuya Mikami and Ming Che for their support and cooperation. I thank my colleagues in KATO-LAB especially Yoshiki Kamiura and Ryo Doi for their assistance in setting up the laboratory experiments and discussions.

I would also like to extend my gratitude to Dr. Tatsuro Maeda of Device Technology Research Institute, AIST, Tsukuba-Japan, for providing a platform for device fabrication and Dr. Yoshimasa Sugimoto for his guidance throughout the fabrication process.

Furthermore, I'm grateful to the Japanese government for funding my doctoral studies through the SPRING program.

I must express my heartfelt gratitude to my family for always supporting me. I am profoundly grateful to my wife for all the support and being by my side during my doctoral studies.

To everyone who has contributed to my academic success in anyway, THANK YOU!

ABSTRACT

Recent advancements in semiconductor photonic and electronic devices such as the Uni-travelling-carrier photodiode (UTC-PD), have played a significant role in the development of Terahertz communication technology. However, a major challenge that still persists is the limited power output from a single UTC-PD that is required for practical wireless transmission distances. To enhance the output power, this thesis proposes and demonstrates a novel terahertz wave power combining technique using photomixer devices that comprise of arrayed UTC-PDs monolithically integrated with microstrip line-based T-junction and Wilkinson power combiners, and a rectangular patch antenna optimized for 300 GHz, on a Silicon Carbide (SiC) substrate that has a higher thermal conductivity than the conventional Indium phosphide (InP) substrate. The combiners are designed and fabricated with 2×1, 4×1, and 8×1 configurations exhibiting a power enhancement of about 5.8 dB, 11 dB, and 16 dB respectively. Measurement results are consistent with the theoretical assertion that power can be enhanced by a factor of N^2 if the photocurrent is multiplied by a factor of N. This technology presents a holistic and cutting edge platform for further power multiplication by further increasing the number of arrayed UTC-PDs.

Additionally, it is experimentally demonstrated that the device output is a function of electron velocity overshoot in the depletion layer of the UTC-PD that depends on an optimum bias voltage which is -1 V for the device used in this work that corresponds to an optimal electric field of 80 kV/cm. Moreover, the device saturation is a function of the space charge effect that is as a result of a critical charge density that modulates the electric field in the depletion region.

Furthermore, the research demonstrates up to 4 Gbps data transmission rate with a 4×1 T-junction combiner integrated device and 2 Gbps for a 2×1 Wilkinson combiner integrated device.

Keywords: *Microstrip line; patch antenna; photomixing; terahertz wave; uni-travelling carrier photodiode; T-junction combiner; Wilkinson power combiner; wireless communication.*

要旨

単一走行キャリアフォトダイオード（UTC-PD）などの半導体光デバイスおよび電子デバイスの最近の進歩は、テラヘルツ波通信技術の発展において重要な役割を果たしている。しかし、単一の UTC-PD からの出力電力限界があり、実用的な伝送距離を実現するためには出力電力が不足しているという大きな課題が依然として存在している。本論文では、出力パワーを向上させるため、従来のインジウムリン（InP）基板よりも熱伝導率の高いシリコンカーバイド（SiC）基板上に、マイクロストリップラインベースの T ジャンクションコンバイナおよびウィルキンソンパワーコンバイナとモノリシックに集積されたアレー型 UTC-PD、および 300 GHz に最適化された矩形パッチアンテナで構成されるフォトミキサデバイスを用いた新しいテラヘルツ波パワーコンバイニング技術を提案・実証した。このコンバイナは、2 × 1、4 × 1、8 × 1の構成で設計・製造され、それぞれ約 5.8 dB、11 dB、16 dB のパワー増強を示した。測定結果は、光電流がN 倍になれば、パワーは N^2 倍に向上するという理論的予測と一致している。この技術は、アレー化された UTC-PD の数をさらに増やすことにより、さらなるパワー増強が可能な最先端のプラットフォームである。

また、デバイス出力は、UTC-PD の空乏層における電子速度のオーバーシュートの関数であり、最適バイアス電圧に依存することが実験的に実証された。本研究で使用したデバイスでは、この最適バイアス電圧は-1V であり、80 kV/cm の最適電界に対応する。さらに、デバイス出力の飽和は、空乏領域の電界を減少させるいわゆる空間電荷効果に依存する。

さらに、4 × 1の T ジャンクションコンバイナを用いて集積したデバイスでは最大 4 Gbps、2 × 1のウィルキンソン・コンバイナーを用いて集積したデバイスでは最大 2 Gbps のデータ伝送レートを実現した。

キーワード: マイクロストリップライン；パッチアンテナ；テラヘルツ波；単一走行キャリアフォトダイオード；フォトミキシング； T ジャンクションコンバイナ； ウィルキンソンパワーコンバイナ； ワイヤレス通信.

LIST OF FIGURES

Contents

CHAPTER 1

INTRODUCTION

1.1 BACKGROUND AND MOTIVATION

In modern society, robust and reliable communication systems are extremely important as immediate access to information is essential. Since the advent of multimedia services on the Internet in the 1990s, there has been a steady rise in global traffic, as the number of devices connected to communication networks is rapidly growing. Users now access a plethora of digital services and information through handheld devices like smartphones and tablets. Additionally, the proliferation of personal multimedia devices such as digital cameras and camcorders, coupled with affordable high-capacity storage media, has empowered individuals to actively contribute to the dissemination of multimedia content.

It is now not merely about consuming content provided by service providers, but also about users creating and sharing their own digital content via the internet using smartphones. Consequently, users now expect innovative ways to manage and share data across both stationary and mobile devices, as well as seamless data storage solutions. This has led to a growing demand for wireless connections driven by the need for convenience and mobility. This trend is expected to continue, with projections suggesting a requirement for around 1Tbps data transmission by 2030 as shown in figure 1.1 [1].

To sustain this progress, advanced network architectures are necessary, including the widespread use of small radio cells and strong backhaul infrastructures that utilize high-capacity, high-bandwidth wireless point-to-point links. Additionally, as fifth-generation (5G) mobile communication systems become widely adopted worldwide, there is a growing research focus on Beyond 5G/6G technology. This has created an urgent need to explore new frequency resources in order to meet the future communication's wide bandwidth requirements.

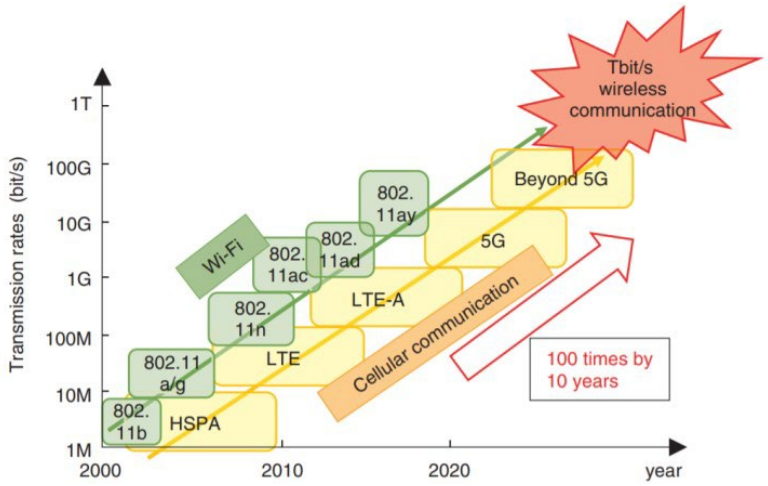

Figure 1.1: Evolution trend of data rates for wireless communications [1]

While advancements in modulation schemes and signal-processing techniques have enhanced data capacity in current wireless systems operating at microwave frequencies, achieving ultrafast data rates remains a formidable challenge due to the inherent limitation of bandwidth. The available spectrum allocated to mobile services, offers limited bandwidth, necessitating unrealistically high spectral efficiencies to transmit >100 Gbps of data.

The 2019 World Radiocommunication Conference (WRC-19), organized by the International Telecommunication Union - Radiocommunication (ITU-R), allocated a substantial spectrum of 13.5 GHz, comprising various high-frequency bands, to be deployed for 5G millimeter-wave wireless communications [2]. Despite the seemingly ample spectrum in millimeter-wave (mm-wave) bands, it may not suffice to meet the escalating demand for ample bandwidth in the coming years. Higher frequencies beyond 300 GHz, previously utilized for diverse applications like remote sensing, radar, and astronomy [3], hold enormous spectral resources. Advancements in radio-frequency devices as well as antenna technology have rendered these frequencies technically feasible for mobile wireless communication, despite their historically unfavorable propagation characteristics [4]. Consequently, future wireless communication systems with Tbps data rates, necessitate access to additional spectral resources, particularly beyond 300 GHz in the terahertz (THz) frequency band and here's why:

1. Spectrum Scarcity of Sub-6 GHz Band: Sub-6 GHz frequencies offer favorable propagation characteristics that enable the utilization of advanced technologies in transmission such as multi-input multi-output (MIMO) [5], non-orthogonal multiple access (NOMA) [6], and high-order

modulation such as 1024-ary quadrature amplitude modulation (1024QAM) for high spectral efficiency. However, spectrum scarcity poses significant challenges to attain the higher data rates. Even if a 1 GHz bandwidth is availed for mobile telecommunications services, a terabit-per-second data link can be realized only under the acute spectral efficiency of 1 Kbit/s/Hz, as per the Shannon's capacity formula $C = B\log(1 + S/N)$. Achieving such a level of performance is currently infeasible, as the peak spectral efficiency specified for 5G is 30 bit/s/Hz [7].

2. Inadequate mm-wave Bandwidth for Tbit/s: The mm-wave band below 100 GHz offers spectral resources of about 13.5 GHz. However, achieving a data rate of 1 Tbit/s would require transmission schemes with a spectral efficiency of about 100 bit/s/Hz, that is unattainable for sub-6 GHz band frequencies at the moment and even quite exacting to implement for mm-wave signals. Thus, achieving Tbit/s data rates relies on abundant bandwidth attainable with frequencies that are over 100 GHz.

3. Practical Limitations of Optical Bands: While optical bands offer vast available spectrum in the infrared (IR), visible light, and ultraviolet frequencies, however, practical limitations hinder the widespread use of optical wireless communications (OWC) for mobile systems in 6G and beyond. These constraints include limitations on transmission power because of hardware limitations, various types of atmospheric attenuation affecting signal propagation such as rain, reflection losses, as well as the effect of misaligned transmitter and receiver, all of which result in limited data rates and short transmission ranges [8].

4. Significant Health Risks of Extremely High Frequency Bands: Radiations, such as X-rays, and ultraviolet (UV) rays, are ionizing and present adverse health risks as they can depose an electron and generate radicals that can cause cancer. While ionizing radiation can be used in fields like radiotherapy and semiconductor manufacturing, it remains very dangerous to be used for personal wireless communication [9]. In contrast, terahertz waves are non-ionizing since they have 0.1 to 12.4 meV photon energy that is not sufficient to dislodge electrons from an atom, where 12 eV photon energy is needed for ionization, making them safer for personal communications.

The reasons mentioned above have spurred research and development efforts towards THz communications, with significant progress made in THz generation (sources), propagation and detection over the past decade. Moreover, initiatives towards standardization and spectrum

regulation above 300 GHz were initiated as early as 2008, indicating a concerted effort to pave the way for THz communication systems. In the realm of THz generation, besides solid-state electronics generation technologies, photonics assisted devices and technologies employing the photomixing technology using a uni-travelling carrier photodiode (UTC-PD) have undergone significant development. These devices can leverage photonics or optoelectronic technologies, offering advantages like tunability, wide bandwidth, and the capability to transmit and process THz signals with minimum losses over a very wide range of frequencies. This is in addition to advancements in antennas designs as well as transceiver architectures designed on novel materials having excellent properties taming significant challenges [10].

1.1.1 THz wave propagation

Before designing any radio communication system, it is crucial to carefully consider the specific conditions of the radio channel. The system specifications must adequately address the characteristics and peculiarities of the underlying radio channel. System parameters that depend on the physics of electromagnetic radio wave propagation, such as link attenuation and the potential for multipath propagation, dictate the properties of the physical layer system design. Without knowledge of the radio channel characteristics, no link budget, modulation scheme, or equalization method can be established. Therefore, a thorough understanding of wave propagation is crucial for any new radio telecommunications technology.

This understanding becomes even more critical for THz communications compared to systems in conventional frequency ranges at 5 GHz or below, for two main reasons. First, the carrier frequency in THz communications is significantly higher spanning from 0.1 THz to 10 THz as shown in figure 1.2. For instance, at 300 GHz, it is 150 times higher compared to the widely used industrial, scientific, and medical (ISM) band at 2.4 GHz. Second, the envisaged bandwidths of 10 GHz and beyond in THz communications exceed the 40 MHz wide bands of WLANs according to IEEE 802.11n by at least 250 times. Due to the very high frequencies involved, wave propagation in the THz range is generally considered to be quasi-optical. These significant differences result in entirely different wave propagation conditions and require different concepts to address the challenges that arise.

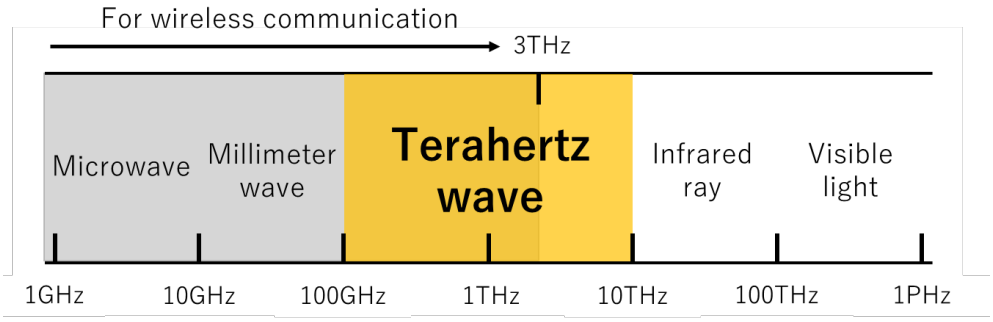

Figure 1.2: The terahertz-wave in the electromagnetic spectrum

To gain a comprehensive understanding of THz wave propagation, this section provides a brief overview of the relevant individual propagation phenomena including path loss, atmospheric absorption and obstruction loss.

1.1.2 Free Space Path Loss (FSPL)

In wireless signal transmission, free-space path loss (FSPL) represents the decrease in power between the transmission and reception of a signal due to the spreading of electromagnetic energy as it propagates through space. This attenuation increases quadratically with the distance traveled by the signal, leading to a reduction in power density.

The relationship between the transmitted signal power (P_{tx}) and the average received power (P_{rx}) can be described using the Friis formula [11], [12], which indicates that the propagation loss is directly proportional to the frequency of the transmitted signal.

$$P_{rx}(dBm) = P_{tx}(dBm) + G_{tx}(db) + G_{rx}(db) + 20\log_{10}\left(\frac{4\pi df}{c}\right) \qquad (1-1)$$

This relationship is illustrated in figure 1.3, which shows the calculated FSPL at different frequencies. It's evident that as the frequency increases from microwave to THz bands, there is a substantial power loss for a given distance.

However, it's important to note that FSPL is a simplistic model that is only accurate for line-of-sight links with stationary antennas in that it does not adequately capture the complexities of wireless propagation in real-world scenarios. In terrestrial wireless communication systems, the environment is not free space but rather characterized by various obstacles and surfaces that reflect, diffract, and scatter electromagnetic waves. This results in non-line-of-sight (NLoS) paths between

transmit and receive antennas, in addition to the direct line-of-sight path. These NLoS paths introduce additional losses in the received signal power because of the differences in power attenuation, phase rotations as well as propagation delays. The multiple copies of the electromagnetic waves that arrive at the receiver, known as multipath components, further contribute to signal degradation. As a result, accurate modeling, and extensive measurements of path loss for different frequencies and propagation environments are essential for understanding and optimizing wireless communication systems.

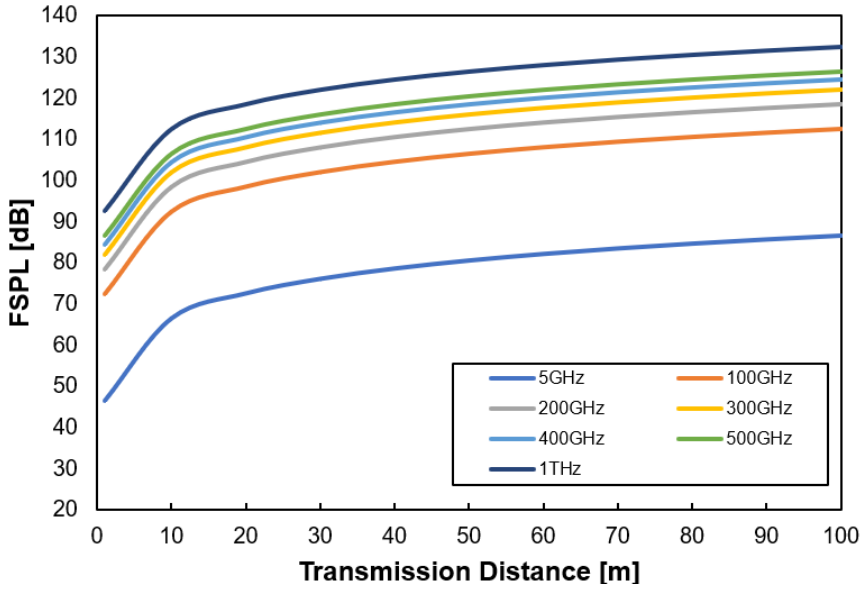

Figure 1.3: Free-space path loss (FSPL) as a function of wireless transmission distance

1.1.3 Atmospheric Absorption

Atmospheric absorption of electromagnetic (EM) waves is a critical factor for wireless communication systems, particularly in the terahertz (THz) band, where absorption losses can be significant. While traditional cellular systems typically ignore atmospheric absorption in the sub-6G band due to its negligible impact, it becomes a major concern for THz waves. The absorption is due to the EM waves interaction with gaseous molecules in the atmosphere [13]. When the wavelength of THz radiation becomes comparable to the size of molecules in the atmosphere, it triggers vibrational shifts in polar molecules. The transformations possess quantum properties, with resonances manifesting at precise frequencies dictated by the internal structure of the molecules, resulting in prominent absorption peaks at particular frequencies [14].

The International Telecommunication Union Radiocommunication Sector (ITU-R) has developed models, such as the ITU-R P.676-12, [15] to estimate gaseous absorption under different atmospheric conditions, incorporating factors like oxygen and water vapor spectral lines, nitrogen absorption, as well as water vapor absorption. Figure 1.4 illustrates the attenuation of signal strength under different atmospheric conditions. The conditions assumed are air pressure of 101.3 kPa, ambient temperature of 20°C and water vapor; 0 g/m^3 for dry air, 7.5 g/m^3 for clear sky and 50 g/m^3 for heavy rain derived from ITU Recommendation ITU-R P.676-12 [16] and ITU-R P.838-3 [17].

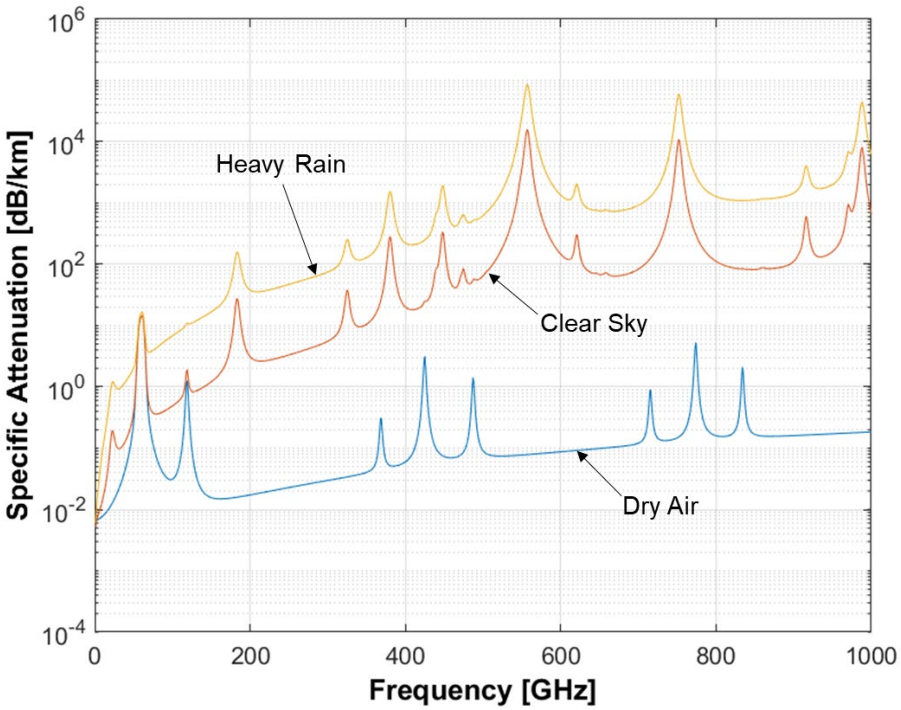

Figure 1.4: Propagation losses for electromagnetic wave of up to 1 THz due to the atmospheric attenuation.

While some studies focus on indoor or nano-communications where atmospheric effects are less significant, for macroscale THz communication, especially outdoors, understanding and mitigating atmospheric absorption is crucial. Recent research projects, have developed algorithms to plan backhaul links considering atmospheric effects [18], [19]. Also, standardization efforts such as in IEEE 802.15.3d [20], are underway to address the challenges of atmospheric absorption in THz communication.

1.1.4 Obstruction Loss

The extremely THz waves small wavelength means that the sizes of common physical objects are relatively large enough to cause scattering, making it challenging to achieve specular reflections on regular surfaces. Consequently, THz systems often rely on narrow pencil beams to effectively propagate signals over distance, necessitating a clear line of sight (LoS) between the transmitter and the receiver. However, this LoS link is vulnerable to obstruction by both large-scale objects like buildings, furniture, vehicles, and foliage, as well as small-scale objects like humans, more so than in the traditional sub-6G band [21]. Even a single obstruction can lead to significant signal loss, sometimes several decibels. The signal loss due to foliage is directly related to the density of vegetation, with losses in the range of tens of decibels [22]. Vehicle blockage loss varies based on vehicle geometry, ranging from 20 dB to 50 [23]. Human body obstruction is particularly impactful due to human movement and close interaction with THz devices, with expected losses of around 40 dB [24]. These losses can significantly degrade signal energy and potentially cause complete signal outage.

Consequently, it is imperative to comprehensively understand the characteristics of blockages and devise effective strategies to either prevent blockages or swiftly restore connectivity in the event of blockage occurrence. Statistical modeling techniques offer a promising avenue for estimating blockage losses, facilitating the development of proactive mitigation strategies. By accurately assessing the impact of various obstructions, engineers can implement robust measures to maintain signal integrity and ensure uninterrupted communication in THz systems.

1.1.5 Potential THz Applications in B5G Era

The extensive spectrum available at THz frequencies creates possibilities for extremely fast wireless communication applications. Additionally, high flexibility in designing mobile systems is realized, as terahertz links can be used for backhaul between base stations, enabling dense architecture, speeding up network deployment, as well as site cost reduction. Because THz signals have tiny wavelengths, antennas can be very miniature, leading to applications such as nanoscale and on-chip communications, as well as the Internet of Nano-Things [25]. Furthermore, THz signals could be used for sensing and imaging [26].

1.1.6 Applications of Terahertz Communications

a) Cellular Terabit Hotspots: : In urban areas with a high density of users and locations such as industrial sites, there is a significant demand for high-throughput networks. The THz band offers vast spectral resources and broad bandwidth, ideal for small cells with limited coverage and high potential for line-of-sight (LoS) passages, enabling terabit per second communication. These small cells support both stationary and mobile users indoors and outdoors, facilitating applications like ultra-high-definition video streaming, high-quality virtual reality, and holographic [27] communications. By integrating conventional low-frequency cellular networks, a heterogeneous network can be created, combining macro-base stations and small cells to provide seamless connectivity and global roaming, meeting the extreme performance needs of future 6G and beyond mobile networks [28] .

b) Terabit Private Networks: THz frequencies enable ultra-high-rate, reliable, and ultra-low-latency wireless connectivity in private networks for applications like Industry 4.0 [29]. This enables seamless interconnection between optical networks and devices with no delay difference. Additionally, ample bandwidths at THz frequencies enable massive connection density [30]. This facilitates the deployment of actuators in factories as well as campus networks having high data-rates, low latency, and reliable connections for equipment for example automated guided vehicles (AGVs) in logistic centers.

c) Terabit Device to Device Connection: Terahertz communications enable direct Tbit/s links between devices that are in close proximity [31]. Device to device links between personal and commercial devices can benefit indoor settings, like offices [32]. Also, applications like multimedia can be supported with Tbit/s links, enabling the transfer of large-size data in a very short period of time. THz communications can also be used in the transfer of high-definition (HD) videos to machine learning-based analytical software platforms. Additionally, Tbit/s device to device links can be used in outdoor scenarios such as vehicle-to-everything [33], providing low-latency and high-throughput connectivity between vehicles and/or between vehicles and nearby infrastructure.

d) Secure Wireless Communication: Large-scale antenna arrays can help in compensation of the path loss and atmospheric attenuation challenges of THz wireless communications, providing high gain and beamforming capabilities for long-distance communications links while minimizing eavesdropping incidents and interference [34]. Furthermore, the utilization of ultra-wide bandwidth and spread spectrum technologies can enhance THz communications security. However, THz communications face unique security challenges that must be addressed, such as the ability of THz waves to penetrate some materials and some types of packaging, which could be exploited by spiteful actors [35].

e) Terabit Wireless Backhaul: Fiber optic installations are often costly and time-consuming, and at times it may not always be feasible to install optical networks in certain buildings or areas. However, the next-generation mobile network is anticipated to be heterogeneous, requiring high-throughput backhaul and fronthaul connectivity between network elements. Directive terahertz links can provide ultra-high-speed wireless backhaul or fronthaul [36], reducing the installation time and cost as well as maintenance whilst enabling flexibility in network architecture [37]. Additionally, mobile service users in remote areas nowadays suffer from low quality of service (QoS). As a wireless backhaul extension of the optical fiber [38], THz wireless links can be an essential building block to guarantee a universal telecommunications service with high-quality, connections anywhere.

f) Terahertz Nano-Communication: The small size of an antenna used for transmitting THz signals can be on the scale of micrometers [39], enabling wireless connections among nanoscale machines and nanomachines utilizing nanoscale antennas for very small equipment that executes tasks at nanoscale, for example biosensors injected in the human blood vessel. Every component of a nanomachine is about a few hundred cubic nanometers, and the entire device is in the order of a few cubic micrometers. Several specific use cases of THz nano-communications are provided by [40], including:

- Health Monitoring: Detecting sodium, and other ions in the blood, , cancer biomarkers, or the presence of different infectious agents using nanoscale biosensors injected into the human body or put under the human skin. A set of biosensors placed within or around the human body, with a body sensor network, can collect relevant physical or biochemical data related to a person's health [41].

- Biological and Chemical Defense: Detecting harmful chemicals and biological threats in a distributed manner using chemical and biological nano-sensors. One of the major benefits of using nano-sensors instead of the classical macroscale or microscale sensors is that a chemical composite could be detected in a low concentration as one molecule and is more timely than classical sensors [42].
- Internet of Nano-Things: Using terahertz nano-communications enables the connection of nanoscale devices in wireless networks [43], and the Internet, making a cyber-physical system that can be termed as the Internet of Nano-Things (IoNT) [44]. The IoNT can enable applications that can reshape the way humans work and live.
- On-Chip Communication: Terahertz communications can provide an efficient approach to inter-core connections in on-chip wireless networks using nanoantenna arrays to enable ultra-high-speed links [45]. This approach is expected to fulfill the strict requirements of the area-limited and communication-intensive on-chip technology by its ultra-high bandwidth and low latency.

1.2 PROBLEM STATEMENT AND RESEARCH SCOPE

The terahertz (THz) band, spanning from 0.1 THz to 10 THz, occupies a unique position in the electromagnetic spectrum, bridging the gap between the microwave and optical bands. Initially dubbed the "terahertz gap", this region remained largely unexplored due to the lack of suitable devices and techniques for generating and detecting THz waves until the mid-1980s [46]. However, significant strides have been made in THz technology research and development over the past few decades, revealing the immense potential of THz waves in various fields such as imaging, spectroscopy, security, and communications.

Pioneering work using pulsed THz waves that generated, and detected using femtosecond-pulse lasers, paved the way for practical applications in spectroscopy and imaging in the early 1990s. The advancement of semiconductor device technologies further expanded the capabilities of THz technology, leading to the development of THz communications systems in the 2000s. The emergence of measurement and testing technologies, such as THz network analyzers and spectrum analyzers, has further accelerated the progress of integrated circuit technologies, enabling the creation of compact and cost-effective THz systems.

While early demonstrations of THz wireless communication links primarily focused on the sub-THz region (100 GHz to 300 GHz), recent advancements have pushed the boundaries of THz technology even further. Photonics-based approaches, which facilitate efficient signal generation and modulation, initially achieved a single-channel data rate of 100 Gbit/s [47]. However, electronics-based systems have since caught up, matching the speed offered by photonics [48]. Table 1.1 summarizes the primary characteristics of the two technical approaches.

Table 1.1: Characteristics of Electronics and Photonics THz wave generation technologies

Parameter	**Electronics-based**	**Photonics-based**
Output power	√ High	Low
Bandwidth	Moderate	√ Large
Data rate	Moderate	√ High
Tunability	Fixed	√ Flexible
Signal quality	Low	√ High
Phase noise	High	√ Low
Integration with fiber	Difficult	√ Easy

The evolution of THz technology has transformed the once-ignored terahertz gap into a realm of immense potential, offering unprecedented capabilities in various fields and paving the way for future advancements in communication and beyond.

However, realizing the full potential of THz technology still requires overcoming significant technical challenges. For instance, electronics-based technologies face acute challenges when it comes to delivering high output power levels at high frequencies [49]. Although radio frequency amplifiers, can partially compensate for these power limitations, they introduce other snags such as higher noise figure and constricted bandwidth. Besides the electronics-based THz generators, photonics-based THz wave emitters using the photomixing technique with a UTC-PD have been widely investigated. These devices can leverage photonics or optoelectronic technologies, offering advantages like tunability, wide bandwidth, and the capability to transmit and process THz signals with minimum losses over a very wide range of frequencies [50-52]. Even so, UTC-PD-based photomixers face the challenge of insufficient power output for practical wireless communication. The salient contributing factor to the low output power is the saturation of UTC-PDs due to space-charge effect in the photodiode carrier transport area, exacerbated by the necessity to increase the bias voltage, causing heat generation [53-55]. Hence, there is a dire need to design and develop devices with reduced space charge to improve thermal dissipation.

Several approaches have been suggested to tackle the power constraints linked to an individual UTC-PD. They include photodiode epi layer optimization [55,56], integrating impedance matching circuits monolithically with UTC-PDs [57,58], as well as power combining. The power combining approach has been particularly implemented by techniques like spatial power combining with planar arrayed antennas [59,60], multi-layer packaging technologies that integrated multiple UTC-PDs monolithically with rectangular waveguide power combiners [61], and planar power combiners [62]. Furthermore, using materials with high thermal conductivity is also considered an effective solution for mitigating thermal challenges, since the poor thermal conductivity of Indium Phosphide presents a significant hurdle to achieve high output power level from a solitary UTC-PD.

This thesis proposes and demonstrates a power combining technology using a microstrip line-based T-junction combiner, a conventional Wilkinson combiner which uses a circular

topology within the $\lambda/4$ section, and a novel coupled line Wilkinson combiner monolithically integrated with a rectangular microstrip patch antenna at 300 GHz, to combine photocurrents from arrayed UTC-PDs, thereby addressing the power limitations inherent in conventional single UTC-PDs. The effectiveness of the Wilkinson combiner for arrayed photodiodes has been demonstrated in the microwave frequency range [63]. Therein, a straight line topology is used in the $\lambda/4$ section whereas in this thesis, a circular topology is used that is effective in reducing the chip area. Furthermore, the use of a novel coupled-line Wilkinson combiner is demonstrated. The coupled-line Wilkinson combiner is easier to fabricate than the conventional Wilkinson combiner and it's $\lambda/4$ lines cover a half area of 0.1×0.055 mm^2 compared to the conventional Wilkinson combiner. Thus, the coupled line Wilkinson combiner can be a better choice for monolithic integration of components at THz frequencies. Also, the microstrip line technology is used which provides more ease to monolithically integrate more photodiodes for large-scale current combining compared to alternative transmission lines like coplanar waveguides (CPWs) reported in [62].

Additionally, the chips are fabricated on Silicon Carbide (SiC), because of its higher thermal conductivity relative to InP. Thermal dissipation capability is an important consideration in the context of output power from UTC-PDs. The utilization of heterogeneous substrates having a high thermal conductivity, like SiC, that has a thermal conductivity that is seven times higher than that of InP, is a promising solution for this challenge. Furthermore, there are significant thermal challenges for the UTC-PD to operate at higher current. For InGaAs/InP devices, the thermal conductivity of the InP substrate (68 W/m/K) is a major limiting factor for high output photocurrent [64]. This limitation is particularly pronounced in vertically illuminated and waveguide photodiodes (WGPD) based on UTC-PDs on InP substrate [65]. The issue is exacerbated by the significantly lower thermal conductivity (5 W/m/K) of the ternary absorber, typically InGaAs, grown on the InP substrate [66]. Consequently, the flow of heat in the conventional absorber region is further impeded, resulting in temperature accumulation and eventual thermal failure. To address this thermal challenge, the utilization of a SiC substrate, characterized by a markedly higher thermal conductivity of 490 W/m/K [67], has been proposed.

Figure 1.5 illustrates a simplistic photonic system configuration of a THz wave transmitter and table 1.2 summarizes the challenges as well as the proposed solutions to enhance the output of THz emitters.

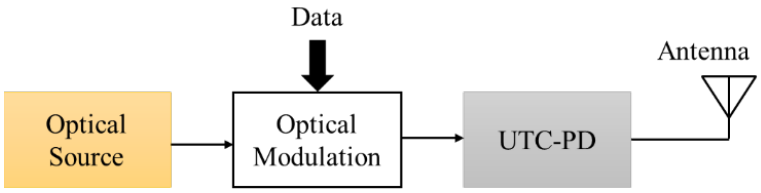

Figure 1.5: A simplistic photonic system configuration of a THz wave transmitter

Table 1.2: Challenges and proposed solutions for THz wave power enhancement.

System component	Current Technology	Challenge	Solution
Optical Source	Free-running laser	Phase noise	Micro-optical Comb
UTC-PD	InP	Saturation (μW range output); insufficient for practical transmission distances.	Use of SiC substrate (wafer bonding), on chip arrayed UTC-PDs, planar combiners.
Antenna	Horn antennas, waveguides, PTFE lenses, Si lenses.	Impedance matching, large bandwidth, high gain, difficulty in device fabrication and packaging.	On-chip impedance matching circuit, microstrip line, planar antenna.

1.3 RESEARCH OBJECTIVES

The primary objective of this thesis is to investigate the integration of arrayed UTC-PDs with microstrip planar combiners, specifically the Wilkinson Combiner and T-Junction combiner. By combining multiple photocurrents generated from the arrayed UTC-PDs using these combiners, the overall photocurrent can be significantly increased, leading to higher emitted THz power.

The specific objectives are as follows:

- Study the existing THz wave generation technologies.
- Design, simulate and optimize a microstrip planar patch antenna and power combiners, including the Wilkinson power Combiner and T-Junction power combiner, with the 2 by 1, 4 by 1, and 8 by 1 configurations, for efficient combining of UTC-PD photocurrents.
- Fabricate the UTC-PDs integrated with power combiners and patch antenna.

- Characterize the fabricated device; frequency response, photocurrent combining coherence, bias voltage dependence, output linearity, frequency response, and radiated THz power enhancement.
- Application of the fabricated device in a wireless communication system.

1.4 THESIS STRUCTURE

The thesis is organized into six chapters. In chapter one, the introduction provides a discussion on the research background, motivation, problem statement, and scope, along with the research objectives.

Moving on to chapter two, a comprehensive study is given on two THz wave generation technologies: electronics-based and photonics-based technologies. Additionally, this chapter delves into the photomixing concept and provides a detailed account of the fundamental principles of a UTC-PD.

Chapter three focuses on the design principles for the devices used in this study. It elucidates the theory of microstrip line technology, patch antenna design, as well as the design of T-junction combiner, conventional Wilkinson combiner, and coupled line Wilkinson combiner.

Chapter four presents the fabrication process and characterization results of a UTC-PD integrated with a bow-tie antenna on Silicon Carbide (SiC) substrate.

In chapter five, a thorough account is given on the fabrication and characterization of arrayed UTC-PDs integrated with a patch antenna and a combiner on SiC substrate. The purpose of this chapter is to verify the concept of on-chip power combining for enhanced radiated THz power. The characterization involves assessing the performance of the fabricated T-junction and Wilkinson combiner, as well as the antenna co-design with 2 by 1, 4 by 1, and 8 by 1 configurations.

Lastly, chapter six provides a summary of the research findings and their implications, along with suggestions for future research directions.

REFERENCES

[1] D. Lee, H. Sasaki, H. Fukumoto, K. Hiraga, and T. Nakagawa, “Orbital Angular Momentum (OAM) Multiplexing: An Enabler of a New Era of Wireless Communications,” IEICE Transactions on Communications, vol. E100-B, No. 7, pp. 1044–1063, 2017

[2] E. Dahlman, S. Parkvall, and J. Sk¨old, 5G NR - The Next Generation Wireless Access Technology. London, the United Kindom: Academic Press, Elsevier, 2021.

[3] U. Demirhan and A. Alkhateeb, “Radar aided proactive blockage prediction in real-world millimeter wave systems,” in Proc. IEEE Int. Conf. on Commun. (ICC), 2022, pp. 4547–4552.

[4] T. Nagatsuma et al., “Advances in terahertz communications accelerated by photonics,” Nature Photonics, vol. 10, no. 6, pp. 371–379, 2016.

[5] W. Jiang and H. D. Schotten, “Cell-free massive MIMO-OFDM transmission over frequency-selective fading channels,” IEEE Commun. Lett., vol. 25, no. 8, pp. 2718 – 2722, Aug. 2021.

[6] Y. Liu et al., “Developing NOMA to next generation multiple access: Future vision and research opportunities,” IEEE Wireless Commun. Mag., vol. 29, no. 6, pp. 120–127, 2022.

[7] ITU-R M.2410, “Minimum requirements related to technical performance for IMT-2020 radio interface(s),” ITU-R, Recommendation M.2410-0, Nov. 2017.

[8] I. F. Akyildiza, J. M. Jornet, and C. Han, “Terahertz band: Next frontier for wireless communications,” Physical Communication, vol. 12, pp. 16 – 32, Sep. 2014.

[9] T. S. Rappaport et al., “Wireless communications and applications above 100 GHz: Opportunities and challenges for 6G and beyond,” IEEE Access, vol. 7, pp. 78 729 – 78 757, Jun. 2019.

[10] A.-A. A. Boulogeorgos et al., “Terahertz technologies to deliver optical network quality of experience in wireless systems beyond 5G,” IEEE Commun. Mag., vol. 56, no. 6, pp. 144 – 151, Jun. 2018.

[11] H. T. Friis, “A note on a simple transmission formula,” in Proceedings of the IRE, Vol. 34, no. 5, pp. 254–256, 1946.

[12] T. Schneider, A. Wiatrek, S. Preussler, M. Grigat, and R. P. Braun, “Link budget analysis for terahertz fixed wireless links,” IEEE Transactions on Terahertz Science and Technology, vol. 2, no. 2, pp. 250–256, 2012.

[13] D. V. der Weide, J. Murakowski, and F. Keilmann, “Gas-absorption spectroscopy with electronic terahertz techniques,” IEEE Trans. Microwave Theory Tech., vol. 48, no. 4, pp. 740 – 743, Apr. 2000.

[14] D. M. Slocum et al., “Atmospheric absorption of terahertz radiation and water vapor continuum effects,” J. Quant. Spectroscopy Radiative Transfer, vol. 127, pp. 49–63, Sep. 2013.

[15] D. M. Slocum et al., “Atmospheric absorption of terahertz radiation and water vapor continuum effects,” J. Quant. Spectroscopy Radiative Transfer, vol. 127, pp. 49–63, Sep. 2013.

[16] International Telecommunication Union, “Recommendation ITU-R P.676-12: Attenuation by atmospheric gases”, 2019.

[17] International Telecommunication Union, “Recommendation ITU-R P.838-3: Specific attenuation model for rain for use in prediction methods”, 2005.

[18] B. K. Jung et al., “Link-level and system-level simulation of 300 GHz wireless backhaul links,” in Proc. Int. Symp. Antennas Propag. (ISAP), Osaka, Japan, Jan. 2021, pp. 619 – 620.

[19] B. K. Jung and T. K¨urner, “Automatic planning algorithm of 300 GHz backhaul links using ring topology,” in Proc. Eur. Conf. Antennas Propag. (EuCAP), Dusseldorf, Germany, Mar. 2021, pp. 1 – 5.

[20] V. Petrov et al., “IEEE 802.15.3d: First standardization efforts for sub-terahertz band communications toward 6G,” IEEE Commun. Mag., vol. 58, pp. 28 – 33, Nov. 2020.

[21] T. S. Rappaport et al., Millimeter wave wireless communications. Englewood Cliffs, NJ, USA: Pearson Education, Sep. 2014.

[22] P. F. M. Smulders and L. M. Correia, “Characterisation of propagation in 60 GHz radio channels,” Electronics and Commun. Engineering J., vol. 9, no. 2, pp. 73 – 80, Apr. 1997

[23] V. Petrov et al., “The effect of small-scale mobility on terahertz band communications,” in Proc. 5th ACM Int. Conf. Nanoscale Comput. Commun., New York, NY, USA, Sep. 2018, pp. 1 – 2.

[24] C. Slezak et al., “Empirical effects of dynamic human-body blockage in 60 GHz communications,” IEEE Commun. Mag., vol. 56, pp. 60 – 66, Dec. 2018.

[25] F. Lemic et al., “Survey on terahertz nanocommunication and networking: A top-down perspective,” IEEE J. Sel. Areas Commun., vol. 39, no. 6, pp. 1506 – 1543, Jun. 2021.

[26] H. Sarieddeen et al., “Next generation Terahertz communications: A rendezvous of sensing, imaging, and localization,” IEEE Commun. Mag., vol. 58, no. 5, pp. 69 – 75, May 2020.

[27] W. Jiang et al., “The road towards 6G: A comprehensive survey,” IEEE Open J. Commun. Society, vol. 2, pp. 334–366, Feb. 2021.

[28] K. M. S. Huq et al., “Terahertz-enabled wireless system for beyond-5G ultra-fast networks: A brief survey,” IEEE Netw., vol. 33, no. 4, pp. 89 – 95, Jul. 2019

[29] G. Fettweis, “The tactile internet: Applications and challenges,” IEEE Veh. Technol. Mag., vol. 9, no. 1, pp. 64–70, Mar. 2014.

[30] C. Han et al., “Terahertz wireless channels: A holistic survey on measurement, modeling, and analysis,” IEEE Commun. Surv. Tutor., vol. 24, no. 3, pp. 1670 – 1707, Jun. 2022, third Quarter.

[31] S. Ju and T. S. Rappaport, “Sub-terahertz spatial statistical MIMO channel model for urban microcells at 142 GHz,” in Proc. 2021 IEEE Global Commun. Conf. (Globecom), Madrid, Spain, Feb. 2021, pp. 1 – 6.

[32] J. G. Ponce et al., “THz band channel measurements and statistical modeling for urban D2D environments,” IEEE Trans. Wireless Commun., vol. 22, no. 3, pp. 1466 – 1479, Mar. 2023.

[33] K. Guan et al., “Channel sounding and ray tracing for train-to-train communications at the THz band,” in Proc. Eur. Conf. Antennas Propag. (EuCAP), Krakow, Poland, Apr. 2019, pp. 1 – 5.

[34] I. B. Djordjevic, “Oam-based hybrid free-space optical-terahertz multidimensional coded modulation and physical-layer security,” IEEE Photonics Journal, vol. 9, no. 4, pp. 1–12, 2017.

[35] J. Ma et al., “Security and eavesdropping in terahertz wireless links,”Nature, vol. 563, p. 89–93, Oct. 2018.

[36] B. K. Jung et al., “Simulation and automatic planning of 300 GHz backhaul links,” in Proc. Int. Conf. Infrared Millimeter THz Waves (IRMMW-THz), Paris, France, Sep. 2019, pp. 1 – 3.

[37] K. Rikkinen et al., “THz radio communication: Link budget analysis toward 6G,” IEEE Commun. Mag., vol. 58, no. 11, pp. 22 – 27, Nov. 2020.

[38] A.-A. A. Boulogeorgos et al., “Terahertz technologies to deliver optical network quality of experience in wireless systems beyond 5G,” IEEE Commun. Mag., vol. 56, no. 6, pp. 144 – 151, Jun. 2018.

[39] J. M. Jornet and I. F. Akyildiz, “Graphene-based plasmonic nanoantenna for Terahertz band communication in nanonetworks,” IEEE J. Sel. Areas Commun., vol. 31, no. 12, pp. 685 – 694, Dec. 2013.

[40] I. F. Akyildiza, J. M. Jornet, and C. Han, “Terahertz band: Next frontier for wireless communications,” Physical Communication, vol. 12, pp. 16 – 32, Sep. 2014

[41] Q. H. Abbasi et al., “Nano-communication for biomedical applications: A review on the state-of-the-art from physical layers to novel networking concepts,” IEEE Access, vol. 4, pp. 3920 – 3935, Jul. 2016.

[42] A. A. Mamrashev et al., “Detection of nuclear spin isomers of water molecules by terahertz time-domain spectroscopy,” IEEE Trans. Terahertz Sci. Techno., vol. 8, no. 1, pp. 13 – 18, Jan. 2018.

[43] J. M. Jornet and I. F. Akyildiz, “Channel modeling and capacity analysis for electromagnetic wireless nanonetworks in the terahertz band,” IEEE Trans. Wireless Commun., vol. 10, no. 10, pp. 3211 – 3221, Oct. 2011.

[44] I. F. Akyildiz and J. M. Jornet, “The Internet of nano-things,” IEEE Wireless Commun. Mag., vol. 17, no. 6, pp. 58 – 63, Dec. 2010

[45] Y. Yang et al., “Terahertz topological photonics for on-chip communication,” Nature Photonics, vol. 14, p. 446–451, Oct. 2020.

[46] K. Tekbıyık et al., “Terahertz band communication systems: Challenges, novelties and standardization efforts,” Physical Commun., vol. 35, p. 100700, 2019.

[47] S. Koenig, D. Lopez-Diaz, J. Antes, F. Boes, R. Henneberger, A. Leuther, A. Tessmann, R. Schmogrow, D. Hillerkuss, R. Palmer, T. Zwick, C. Koos, W. Freude, O. Ambacher, J. Leuthold, and I. Kallfass, "Wireless sub-THz communication system with high data rate," Nat. Photonics, vol. 7, pp. 977-981 (2013).

[48] H. Hamada, T. Tsutsumi, H. Matsuzaki, H. Sugiyama, and H. Nosaka, "Ultra-high-speed 300-GHz InP IC technology for beyond 5G," NTT Technical Review, vol. 19, no. 5, pp. 74-82 (2021).

[49] H. Elayan, O. Amin, B. Shihada, R. M. Shubair and M. -S. Alouini, "Terahertz Band: The Last Piece of RF Spectrum Puzzle for Communication Systems," in IEEE Open Journal of the Communications Society, vol. 1, pp. 1.32, 2020.

[50] K. Sengupta, T. Nagatsuma, and D.M. Mittleman, “Terahertz integrated electronic and hybrid electronic–photonic systems,” *Nat Electron, vol.* **1**, pp. 622–635 (2018).

[51] A. Wakatsuki, Y. Muramoto, T. Ishibashi, “Development of Terahertz wave Photomixer Module Using a Uni-traveling-carrier Photodiode,” Feature Articles: Imag. and Sens. Techn. for Safety and Security, vol 12 **2012.**

[52] T. Ishibashi, N. Shimizu, S. Kodama, H. Ito, T. Nagatsuma, and T. Furuta, "Uni-Traveling-Carrier Photodiodes," Ultrafast Electronics and Optoelectronics, M. Nuss and J. Bowers, eds., vol. 13 of OSA Trends in Optics and Photonics Series (Optica Publishing Group, 1997), paper UC3.

[53] T. Ishibashi and H. Ito, "Uni-Traveling Carrier Photodiodes: Development and Prospects," in IEEE Journal of Selected Topics in Quantum Electronics, vol. 28, no. 2: Optical Detectors, pp. 1.6, March-April 2022.

[54] T. Ishibashi, H. Ito, ‘Uni-traveling-carrier photodiodes*,”* J. Appl. Phys*.,* 127, 2020.

[55] T. Ishibashi, Y. Muramoto, T. Yoshimatsu and H. Ito, "Unitraveling-Carrier Photodiodes for Terahertz Applications," in IEEE Journal of Selected Topics in Quantum Electronics, vol. 20, no. 6, pp. 79-88, Nov.-Dec. 2014.

[56] X. Dong, K. Liu, Y. Huang, X. Duan, Q. Wang and X. Ren, "Design of High-Speed UTC-PD With Optimization of Its Electron Transit Performance and Parasitic Capacitance," in IEEE Photonics Journal, vol. 15, no. 1, pp. 1.9, Feb. 2023

[57] H. Ito, T. Nagatsuma, A. Hirata, T. Minotani, A. Sasaki, Y. Hirota, T. Ishibashi, “High-power photonic millimetre wave generation at 100 GHz using matching-circuit-integrated uni-travelling-carrier photodiodes,” IEEE Proc. Optoelectron, 150, 138–142 2003.

[58] C. C. Renaud, M. Natrella, C. Graham, J. Seddon, F. Van Dijk and A. J. Seeds, "Antenna Integrated THz Uni-Traveling Carrier Photodiodes," in IEEE Journal of Selected Topics in Quantum Electronics, vol. 24, no. 2, pp. 1.11, March-April 2018.

[59] M. Che, K. Kondo, H. Kanaya and K. Kato, "Arrayed Photomixers for THz Beam-Combining and Beam-Steering," Journal of Lightwave Technology, vol. 40, no. 20, pp. 6657-6665, 15 Oct.15, 2022

[60] Y. Koyama et al., "A High-Power Terahertz Source Over 10 mW at 0.45 THz Using an Active Antenna Array With Integrated Patch Antennas and Resonant-Tunneling Diodes," IEEE Transactions on Terahertz Science and Technology, vol. 12, no. 5, pp. 510-519, Sept. 2022

[61] S. Makhlouf et al., "Novel 3-D Multilayer Terahertz Packaging Technology for Integrating Photodiodes Arrays and Rectangular Waveguide-Power Combiners," IEEE Transactions on Microwave Theory and Techniques, vol. 68, no. 11, pp. 4611.4619, Nov. 2020

[62] H. -J. Song, K. Ajito, Y. Muramoto, A. Wakatsuki, T. Nagatsuma and N. Kukutsu, "Uni-Travelling-Carrier Photodiode Module Generating 300 GHz Power Greater Than 1 mW," IEEE Microwave and Wireless Components Letters, vol. 22, no. 7, pp. 363-365, July 2012

[63] Y. Fu, H. Pan, Z. Li and J. Campbell, "High linearity photodiode array with monolithically integrated Wilkinson power combiner," 2010 IEEE International Topical Meeting on Microwave Photonics, Montreal, QC, Canada, pp. 111-113, 2010.

[64] K. J. Williams and R. D. Esman, “Design considerations for high-current photodetectors”, Journal of Lightwave Technology, IEEE, vol. 17, no. 8, pp. 1443–1454, Aug. 1999.

[65] J. Klamkin *et. al.*, “High output saturation and high-lineaity uni-traveling-carrier waveguide photodiodes”, IEEE Photonic Technology Letter, vol. 19, no. 3, pp. 149–151, Feb. 2007

[66] S. Adachi, “Lattice thermal conductivity of group-IV and III-V semiconductor alloys”, Journal of Applied Physics, vol. 102, no. 6, Sep. 2007

[67] M. Takenaka and S. Takagi, "InP-based photonic integrated circuit platform on SiC wafer," Opt. Express 25, 29993-30000 2017.

CHAPTER 2

TERAHERTZ WAVE GENERATION TECHNOLOGIES

The THz band is far much higher than the microwave band while is lower than the optical bands. On one hand, electronic oscillators are striving to reach the high frequencies whereas on the other hand, photonic devices are not able to produce such low frequencies. Hence, researchers are exploring both electronic and photonic approaches to generate THz waves. Initially, due to component limitations, earlier THz research focused on imaging or spectrometry applications [1]. This emphasis stemmed from two key reasons:

i. These applications necessitated a relatively high signal output power although were not particularly demanding on the side of the receiver, as the signal's amplitude, instead of its phase, serves as the information carrier.
ii. System size or specific operational conditions were not limiting factors.

Conversely, THz communications demand accurate recovery of the signal phase, especially for digital modulation where both in-phase and quadrature (IQ) components are utilized. Additionally, compactness and low energy consumption are crucial. Therefore, semiconductor-based integrated circuits offer advantages for THz communications applications in beyond 5G or 6G systems. This chapter discusses the state-of-the-art advances of both electronic and photonic technologies for THz wave generation.

2.1 ELECTRONIC TERAHERTZ SOURCES

The electronic realization of terahertz sources is promising in terms of compactness, system efficiency and robustness. Additionally, electronics can be easily produced by scalable and cost-effective integrated circuit technics and processes. The limitation with electronic THz generators is the speed of the active devices, which is a function of the electron transit time as well as the parasitic RC-time constants. This has significantly challenged the application of electronic-based devices to generate THz frequencies.

2.1.1 CMOS-based THz Sources

Novel THz systems, used in communication and sensing need compact and cost-effective active components. Technologies such as nanoscale CMOS as well as Silicon-Germanium bipolar CMOS (SiGe BiCMOS) are ideal due to their high integration density and seamless compatibility with digital logic. They have become the preferred choice for the development of high-performance and low-cost electronic terahertz integrated circuits. The pioneer CMOS THz source was using a push-push oscillator in 45 nm CMOS technology, achieving a power output of approximately −42 dBm at a frequency of 410 GHz [2]. Since then, CMOS technology has seen significant advancements in maximum frequency (f_{max}), DC-to-RF efficiency as well as output power.

CMOS THz sources can be categorized into multiplier-chains, free-running oscillators, and locked oscillators. For instance, a phase-locked frequency multiplier chain with integrated antennas reported in [3], can generate signals up to around 1.46 THz. However, they are constrained by poor DC-to-RF conversion efficiency, requiring high input power, particularly challenging to obtain beyond 100 GHz, and resulting in low output power. Another reported example is a multiplier chain of 65 nm CMOS that achieved an output power of −15.1 dBm at a frequency of 607.5 GHz [4] and −22.7 dBm at 1.33 THz [3]. It is needful to note that for higher output power, SiGe BiCMOS is preferred over CMOS, due to its advantages such as higher f_T/f_{max} and higher breakdown voltage. For example, using a SiGe HBT 250 nm BiCMOS , an output power of about −17 dBm at a frequency of 823 GHz was achieved [5]. Similarly, an output power of approximately −17.3 dBm at a frequency of 928 GHz was reported using a 130 nm SiGe BiCMOS process [6].

In contrast, oscillator-based CMOS THz generators have high DC-to-RF conversion efficiency, providing higher output power below 300 GHz, but dropping to microwatt (μW) levels for higher frequencies without power combining techniques. As an example, a 65 nm CMOS THz source with a single ring antenna provided output powers of −2.74 dBm and −23 dBm at frequencies of 293 GHz and 615.3 GHz, respectively [7], [8]. Coherent spatial power combining of arrayed mutual coupling oscillators has also been reported to enhance the radiated power of CMOS THz sources [9], [10], [11], [12], [13]. Every oscillator resonates at a fundamental

frequency and is synchronized with other oscillators, causing harmonic signals to radiate in phase thereby combining to create a highly directive beam. A high-power arrayed source using 65 nm bulk CMOS technology consisting of harmonic oscillators coupled via quadrature oscillators delivered 0.5 dBm at 260 GHz [14].

Free-space coherent power combining has also mitigated the rapid roll-off of CMOS sources with a single-antenna [9], achieving an output power of about −3 dBm at a frequency 694 GHz. However, most radiators are limited to frequencies below 500 GHz because oscillator-based radiators above 500 GHz need a high of fundamental oscillation frequency to maximum oscillation frequency ratio (f_{osc}/f_{max}). In [15], a two-dimensional synchronized oscillator array of 42 coherent radiators achieved an output power of about −10.7 dBm at a frequency of1.01 THz.

2.1.2 Heterojunction Bipolar and High Electron Mobility Transistors

The rapid proliferation of devices has resulted in significant advancements in gain cutoff frequencies in both SiGe heterojunction bipolar transistors (HBTs) and InP HBT devices. SiGe HBTs have achieved gain cutoff frequencies of approximately 700 GHz with an emitter width of around 70 nm [16], while InP HBT devices have exceeded 1 THz with an emitter width of about 130 nm [17]. These bipolar technologies exhibit considerable scaling potential compared to CMOS, which is constrained to approximately 10 nm.

High gain cutoff frequencies in HBTs are attained through various factors. One crucial factor is the reduction of the total base resistance (R_B). This reduction is accomplished through highly p-doping in the base material, which is only feasible with an emitter-base heterojunction. This heterointerface serves as an effective energy barrier in the valence band, impeding the hole diffusion from the heavily p-doped base to the emitter. This sustains higher emitter injection efficiency and consequently higher current gain with a heavily doped base. The heterojunction is established between the SiGe base material and the Si emitter material, or the InGaAs base and the InP emitter.

The cutoff frequency of the power gain (f_{max}) is important for the circuit's operating frequency. The unity power gain frequency (f_{max}) in the bipolar transistor as can be approximated

$$f_{max} \approx \sqrt{\frac{f_t}{8\pi R_B C_{BC}}} \qquad (2-1)$$

where f_t is the current gain cutoff frequency related to the transit time τ_F through the base and the collector. f_t restricts the instantaneous bandwidth for the amplifier circuit. In order to reduce f_t of a transistor, it is necessary to have a thin base and a fully depleted collector. The thickness of the collector can be adjusted to balance the trade-off between the maximum frequency of oscillation (f_{max}) and f_t, which has an inverse effect on the breakdown voltage.

$$\frac{1}{2\pi f_t} \approx \tau_F + (C_{BE} + C_{BC}) \cdot \frac{kT}{qI_C} + C_{BC} \cdot (R_E + R_C) \qquad (2-2)$$

The reduction of capacitance through lateral device scaling is crucial, as indicated by the above equations: the base-collector capacitance (C_{BC}) acts as the negative feedback capacitance. The intrinsic capacitance of the base-collector (BC) junction and the extrinsic capacitive structures must be minimized. Additionally, series resistances (R_E and R_C) should be kept to a minimum. The diffusive capacitance of the forward-biased base-emitter junction requires to be counteracted by a larger collector current (IC), resulting in higher current densities [18]. Technological limitations for scaling are determined by the minimum emitter width, minimum contact resistance, which is close to the physical limit and requires extremely clean interfaces, as well as the trade-off between base sheet conductivity and base transit time.

SiGe HBTs utilizing high-order harmonic extraction have demonstrated operation up to about 1 THz [15], with an output power of about −11 dBm in an arrayed configuration. The BiCMOS process allows for monolithic integration of FMCW radar front-ends achieving a power output of −16.5 dBm and a bandwidth of 45 GHz [19]. At 420 GHz, a SiGe chip with spatial modulation capability achieved a radiated power of 10.3 dBm [20]. Electronic THz pulse generators with high bandwidth can be achieved by reverse recovery of p-i-n diodes, that are part of BiCMOS processes. Additionally, frequency combs have been demonstrated, providing an EIRP between −10 dBm and −60 dBm for 200 GHz to 1100 GHz with a patch antenna of 24.6 dBi to 32 dBi directivity for 330 GHz to 780 GHz [21].

For InP material devices, the narrow-band base can be fabricated using GaAsSb instead of InGaAs. By utilizing an optimized base-emitter structure, recent demonstrations have shown f_{max} exceeding 1.2 THz, along with a $V_{BD,CEO}$ of over 5 [22].

InP high electron mobility transistors (HEMTs) have achieved the highest fmax of approximately 1.5 THz, attributed to the high electron mobility within the 2D electron gas confined vertically in the InAs channel. This advancement led to the successful operation of a nine-stage amplifier at a frequency of 850 GHz [23] and a ten-stage amplifier at a frequency of 1 THz [24].

Metamorphic HEMT devices featuring an InAs channel and a gate with a length of 20 nm on a GaAs substrate have demonstrated fmax exceeding 1.1 THz [25]. InP HEMTs are recognized for their exceptional noise performance, particularly beneficial in mm-wave and sub-THz mixers, as well as low-noise amplifiers (LNA) for radio astronomy at cryogenic temperatures [26]. A recent demonstration showcased an integrated mixer-amplifier InP HEMT source producing 1.8 mW output power at a frequency of 680 GHz, with a DC-to-RF conversion efficiency of 0.1% [27].

In general, InP devices exploit the high electron mobility as well as velocity found in III/V compounds devices. The efficiency of converting direct current (DC) to radio frequency (RF) in transistor sources is closely tied to the ratio of the device's breakdown voltage to the voltage drop at the knee. The elevated electron velocity found in InP allows for a more relaxed device structure. This, combined with a higher breakdown field, leads to a substantial device breakdown voltage and this advantage is particularly evident in the vertical HBT structures, which experience less surface breakdown as compared to the HEMTs.

In the context of future 6G communications, the performance of power amplifiers operating at a frequency of 300 GHz demonstrates the superiority of InP technologies, especially InP HBT, within a broader available database [28]. InP HBT technology also holds promise for THz generation, as InP HBT oscillators have been successfully demonstrated up to around 570 GHz, delivering nearly 10 μW of RF power [29]. Taking into account, the system's reliance on oscillators, precise control of phase and frequency is crucial. Recently, an injection-locked InP HBT oscillator was showcased, achieving a conversion efficiency of 1.7% and an output power exceeding 0.5

mW at 420 GHz. With a transistor f_{max} of 450 GHz, this development enables the realization of efficient THz sources through transistor scaling [30].

2.1.3 Resonant Tunneling Diodes

Besides the realm of transistor technology, resonant tunneling diodes (RTDs) serve as fundamental oscillators characterized by an incredibly short transit time, due to the minimal distance of a few nanometers between the adjacent energy wells within the resonant tunnel diode structure.

By integrating a chip-based narrowband antenna (either in a patch antenna or slot antenna design) that can be adjusted to match the complex impedance of the RTD, highly compact electronic THz sources can be achieved. To date, InP-bases RTD sources have been able to achieve fundamental oscillation frequencies of approximately 2 THz, making them the fastest solid-state oscillators currently available [31]. In various system applications, like wireless communication and spectroscopy, precise control over the oscillator frequency is essential. To address this need, subharmonic injection locking has been successfully demonstrated in RTD devices operating beyond 0.5 THz, resulting in a relatively narrow linewidth and the capability to fine-tune the frequency of oscillation within the locking range [32].

In addition to controlling the frequency as well as the phase of individual sources, and the injection locking process can also be utilized to establish mutual coupling between adjacent RTDs or antenna pixels, enabling the realization of phased arrays operating at terahertz frequencies. An example recently reported includes a 6 × 6 array that emitted close to about 12 mW at a frequency of 450 GHz with a 1% conversion efficiency [33]. The fixed phase relationship between the pixels leads to beamforming, resulting in a directivity gain of approximately 24 dB.

It is anticipated that further enhancements in terms of higher frequency and increased radiated power can be achieved by boosting the dissipated power in the arrays by at least tenfold before reaching thermal limits, as well as at least quadrupling the oscillation frequency.

2.1.4 Schottky-Barrier Diodes

Schottky-barrier diode (SBD) frequency multipliers are commonly used to generate powerful signals in the THz domain, as high-power amplifier technology is currently limited to frequencies close to 100 GHz. These SBDs offer attractive properties that include compactness, reliable performance, and relatively low power consumption [34], [35]. The epitaxial layers of SBDs is typically grown on GaAs or GaN substrates. There are two types of SBDs based on the Schottky contact: whisker-contacted and planar diodes. Whisker-contacted SBDs were initially used for THz frequency generation in the lower THz frequency band [36], [37]. However, their assembly and integration were complicated due to the fragility of the whisker contacts, limiting their widespread use. Planar SBDs, on the other hand, feature a planar Schottky contact that overcomes this drawback. There are two types of planar SBDs; quasi-vertical planar SBDs [38] and surface channel planar SBDs [39]. Quasi-vertical planar SBDs have been limited in their implementation for THz frequency generation due to high parasitic capacitance [40].

Planar channel Schottky barrier diodes (SBDs) have lower parasitic capacitance compared to quasi-vertical planar SBDs, rendering them suitable to generate terahertz frequencies up to about 8.7 THz [41], [42]. The RF performance of these devices showed a series resistance of approximately 15.4 Ω, a junction capacitance of about 1.46 femtofarads, and a cut-off frequency of approximately 7 THz. SBDs have been used effectively as frequency doublers and triplers for THz signal generation due to their nonlinear characteristics. Frequency doublers are generally simpler in design and have higher conversion efficiency compared to frequency triplers. Various SBD frequency multipliers for terahertz applications have been reported. For example, a study integrated GaAs-based SBDs with a quartz-based microstrip-line (MSL) antenna to develop a 332 GHz frequency doubler, achieving a maximum conversion efficiency of 4.7% at 332.8 GHz [43]. Another study showcased THz frequency triplers operating at 220 GHz and 440 GHz, with conversion efficiencies of 16% and 12% respectively [44]. The design and realization of THz frequency triplers were facilitated by implementing stepped-impedance microstrip low-pass filters to bias the diodes and couple the signal from the WR6-input (110–170 GHz) to the output WR2-output (330–500 GHz).

Passive frequency multiplication technologies have made significant advancements in the past decade. These technologies have achieved conversion efficiencies of up to 30% for THz doublers and 20% for triplers, with a bandwidth of 15-18% [45]. However, as the frequency increases, the circuit size tend to decrease, leading to higher losses in hybrid integration technology. To mitigate this issue, extensive efforts have been made to integrate the antenna and the DC-biasing circuitry monolithically with the SBDs on the same substrate, known as monolithic integration. This approach aims to achieve higher output power levels at higher frequencies. For instance, a high-efficiency frequency tripler capable of generating terahertz signals with frequencies between 540 GHz - 640 GHz has been reported in [46]. This design utilized a 12 μm thick GaAs substrate and achieved an efficiency ranging from 4.5% to 9% at room temperature. Another study [47] demonstrated the generation of a THz signal with frequencies between 2.48-2.75 THz utilizing an integrated GaAs SBDs frequency cascaded tripler. By cascading SBD frequency doublers and triplers, THz signals up to 2.75 THz can be generated [48].

A 1.5 terahertz source comprising of a chain of four frequency doublers having a fundamental frequency of about 90 GHz was reported in [49]. The maximum realized output power for this setup was about 40 μW. Additionally, a four-channel source operating at a frequency of 1.9 THz was demonstrated in [50]. This setup utilized a fundamental signal generator of about 30-40 GHz along with two frequency doublers as well as two frequency triplers. Similar to the previous example, the reported power output was about 40 μW.

Cascaded multipliers have also been used to generate THz signals in the WR3-band. A 270-320 GHz source having an output power of 40 mW and an impressive conversion efficiency of over 25% was reported in [51]. Another study [52] reported an active multiplier chain with an output power of 250 mW at 260 GHz. However, the power-handling capabilities of the reported multiplier modules remains a significant limitation. This limitation primarily arises from the inefficient dissipation of thermal energy under relatively high power conditions. Various research groups around the world have tackled the thermal challenges associated with SBDs. Some scholars have opted for the use of sub-mounts with high thermal conductivities, such as Si and AlN [53], [54]. On the other hand, some have experimented with bonding a diamond layer on the backside of the diode [55], [56], leading to a significant enhancement in heat dissipation and consequently, the power-handling capacity of the multiplier.

A novel technological advancement has emerged recently, involving the utilization of SBDs with monolithically integrated diamond heat sinks [57], [58]. This innovative approach is applicable for discrete diode production and for the development of THz-MICs. These MICs are fully integrated circuits incorporating Schottky diodes and passive components such as filters and matching networks, as well as mechanical support elements such as a carrier substrate and a diamond heat sink. These integrated structures are particularly advantageous for frequencies exceeding 600 GHz, where the accuracy of assembling discrete diodes on sub-mounts may not be sufficient to ensure consistent outcomes.

It is a well-established fact that there exists a trade-off between the conversion efficiency and the bandwidth of frequency multipliers. Multipliers with high efficiency are designed to maximize output power, while broadband multipliers aim to cover the entire WR frequency bands. As a result, different types of multiplier sources are utilized for specific applications. Broadband sources are typically used in measurement equipment, while high-power sources are employed in applications where the output power plays a crucial role in achieving the desired application goal, such as dynamic range. Nevertheless, recent advancements in on-chip power combiner technique have led to the development of broadband multipliers with significantly improved output power, up to ten times greater [59]. These advancements have resulted in achieved frequency ranges of 0.16 THz - 1.6 THz, with corresponding output power ranging from 50 mW to 0.7 mW.

2.2 PHOTONIC TERAHERTZ SOURCES

2.2.1 Quantum Cascade Lasers (QCLs)

These are a type of semiconductor lasers that are specifically engineered to emit photons with low energy in the far-infrared and THz frequency range [60], [61]. Generally, QCLs function at frequencies above 2-3 THz. Although they can generate output powers of several hundred mWs when operated at extremely low temperatures, there is still a major challenge in achieving similar power levels at room temperature [62], [63]. This obstacle greatly restricts the practical use of QCLs.

2.2.2 Photoconductive antennas (PCAs)

Another technique to down convert optical signals to the THz band relies on the use of photoconductive antennas [64], [65]. A photoconductive antenna generally consists of a conventional THz metallic antenna printed on top of a photoconductive substrate. When illuminated by an optical signal (normally an optical pulse), photocarriers are excited at the gap of the antenna. A DC bias field is then used to accelerate the carriers along the antenna structure, resulting in the emission of THz photons. The main challenge of this technique relates to the low conversion efficiency and the resulting low emitted power (less than a milliwatt at hundreds of GHz).

2.2.3 Photomixing

Photomixing is an optoelectronic technology that enables the conversion of two lightwaves with different frequencies into an alternating current with a frequency equal to the frequency difference of the two lightwaves using a photodiode or a photoconductor.

Three commonly used photomixing devices include low temperature growth (LTG) GaAs photoconductors (LTG-GaAs), p-i-n PDs, and UTC-PDs. The photoconductor, which is the most fundamental photomixer, is composed of a semiconductor material placed between two electrodes. When the semiconductor is exposed to a laser beam with energy equal to or greater than the band gap of the semiconductor, electron-hole pairs are produced. By applying an electric field to these charges, a closed circuit is established, generating a current proportional to the laser power. The combination of two laser beams with similar wavelengths results in a current at the beat frequency of the two lasers. To achieve optimal performance of the photoconductors, it is crucial to use semiconductor materials with short carrier lifetimes and high carrier drift rates. LT-GaAs photomixers are specifically designed for operation at a wavelength of 800 nm, making them less suitable for optical communications at 1550 nm wavelength. Attempts have been made to develop photoconductors based on InGaAs [66]. However, as shown in figure 2.1 [67], they still exhibit lower performance levels compared to GaAs photoconductors, p-i-n, and UTC-PD photodiodes. Additionally, the design process of InGaAs photoconductors is a bit challenging due to requirements that are at variance such as high resistance, high absorption, high mobility, short carrier lifetime, and high breakdown field [66].

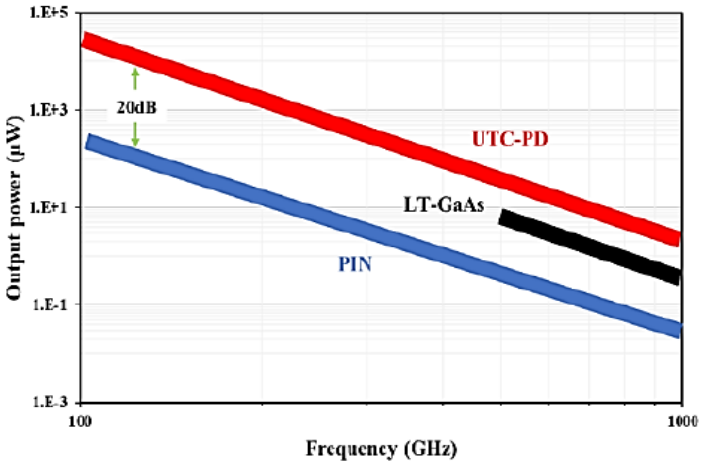

Figure 2.6: Photomixing devices performance in terms of output power [67].

Conventional p-i-n photodiodes (PDs) consist of an intrinsic semiconductor layer positioned between p- and n-doped semiconductors, which absorbs the desired wavelength. Within the depletion region of p-i-n PDs, the generation of electron-hole pairs takes place when exposed to light, and these pairs then drift in the presence of an electric field created by the semiconductor junction. The dynamics of electron-hole drift, as well as the intrinsic resistance and capacitance (RC) of the photodiode, determine its bandwidth. A thinner depletion region results in a shorter transit time, but it also leads to increased capacitance, which limits the photodiode's bandwidth and responsivity. Moreover, the trade-off between the width of the intrinsic region and the RC component is further constrained by the lower velocity of holes compared to electrons.

The responsivity of p-i-n PDs is primarily limited by the transit time of holes through the intrinsic region whereas in UTC-PDs the response is a function of the electron drift velocity . In UTC-PDs, absorption and carrier collection occur as separate processes. Absorption takes place in the p-doped region, where holes, being the majority carriers, recombine due to dielectric relaxation. Consequently, only electrons drift through the depletion region, resulting in a higher 3-dB bandwidth. Additionally, UTC-PDs exhibit superior saturation characteristics compared to p-i-n PDs since there is no accumulation of holes in the depletion region.

Figure 2.2 shows the photomixing concept also known as optical heterodyning using a photodiode to generate THz waves. In a photomixing setup, two lasers with different frequencies are combined and photoelectrically converted at the photodiode to generate an alternating current with the same frequency as that of the frequency difference of the two lightwaves. When the

electric fields for the two lightwaves are E_1 and E_2, the power P of the lightwaves detected by the photodiode, is proportional to the square of the total electric fields of the two lightwaves and are expressed as

$$E_1 = A_1 exp\{i(2\pi f_1 t + \varphi_1 - k_1 x_1)\} \quad (2-3)$$

$$E_2 = A_2 exp\{i(2\pi f_2 t + \varphi_2 - k_2 x_2)\} \quad (2-4)$$

$$P \propto |E_1 + E_2|^2 \quad (2-5)$$

thus

$$P = A_1^2 + A_2^2 + 2A_1A_2 \cos\{2\pi(f_2 - f_1)t + (\varphi_2 - \varphi_1) - (k_2x_2 - k_1x_1)\} \quad (2-6)$$

where A_1 and A_2 are amplitudes of the electric field of lightwaves, f_1 and f_2 are the frequencies, k_1 and k_2 are the wavenumbers, φ_1 and φ_2 are the phases of the light waves, and x_1 and x_2 are the optical path lengths. As a result of the square-law detection at the PD (lightwaves are detected as energy), an alternating current with frequency $f_2 - f_1$ and phase $-(k_2x_2 - k_1x_1) + (\varphi_2 - \varphi_1)$ is generated.

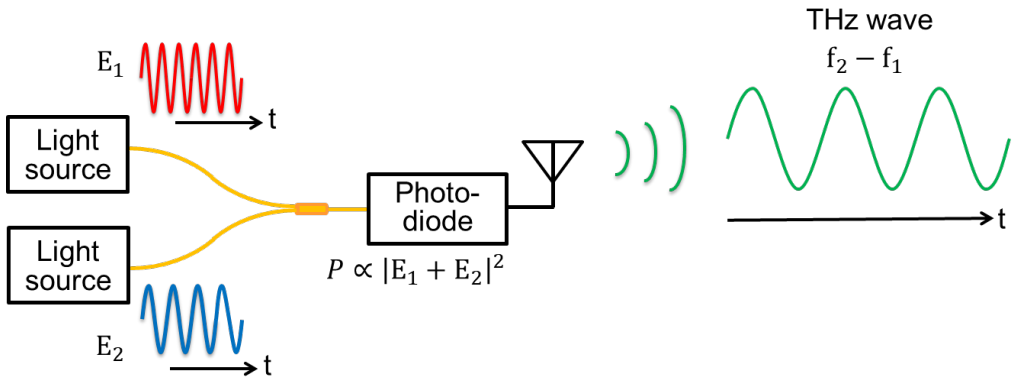

Figure 7.2: Photomixing concept

As it will be discussed in detail in Chapter 5, arrayed PDs which generate terahertz waves with the same phase can be combined to enhance the radiated power. To tune the phase of the terahertz waves, either $(\varphi_2 - \varphi_1)$ or $-(k_2x_2 - k_1x_1)$ should be varied. The former corresponds to changing the phase of each lightwave when the two lightwaves are in different optical paths

while the latter corresponds to changing the optical path length when the two lightwaves are in the same optical path.

In the former case, the same amount of phase change as that of the lightwave can be applied to the terahertz wave. For example, if a phase change of π is applied to the lightwave, the generated terahertz wave will also have a phase change of π. Since an optical phase modulator can change the phase of a lightwave by about π within an operating voltage, it is easy for the phase of terahertz waves to be changed by π. However, the former method requires the use of optical components with optical fibers, such as optical phase modulators, and therefore phase stabilization technology is also required to suppress phase fluctuations in the optical fiber. This means that, for the former case, a phase control device without optical fibers is required.

In the latter case, when both the path lengths are changed by Δx, which corresponds to a "real time delay", the change of the phase difference between the two lightwaves is given by the following equation,

$$-(k_2 - k_1)\Delta x = 2\pi\left(\frac{1}{\lambda_1} - \frac{1}{\lambda_2}\right)\Delta x \qquad (2-7)$$

where λ_1 and λ_2 are the wavelengths of the two lightwaves. In the air, for two lightwaves in the 1550-nm band with an optical frequency difference of 300 GHz (wavelength difference of 2.4 nm), the value in parentheses is about 1 mm^{-1}. If an optical delay line (ODL) is used which changes the air gap between two collimator lenses, for example, to change both x_1 and x_2 by 1 mm ($\Delta x = 1\ mm$), the phase of a terahertz wave is changed by 2π, or one wavelength of a 300-GHz wave.

Figure 2.3 [68], summarizes the THz sources as a function of frequency. Conventional sources are represented by solid lines. Also, for most of the sources, the displayed power is continuous wave (cw) power at room temperature. THz-QCL power is at cryogenic temperatures. MMIC stands for microwave monolithic integrated circuit and DFG is generated by the difference frequency.

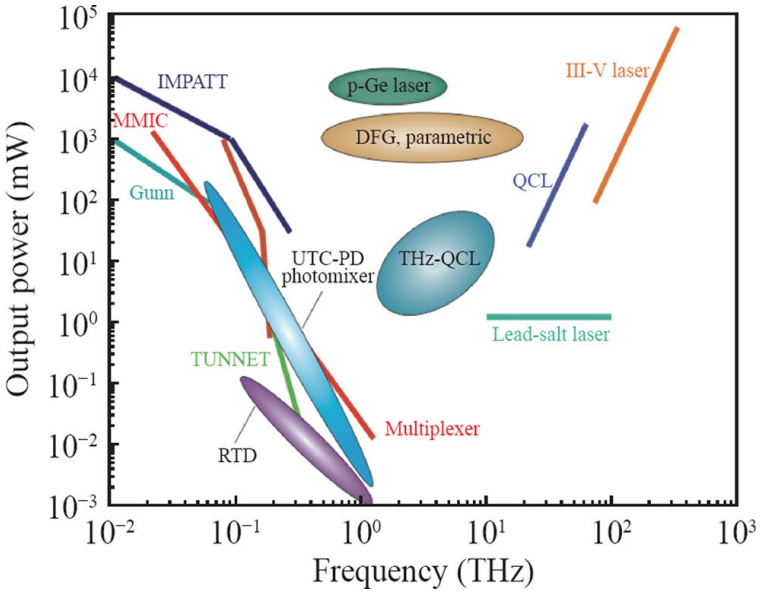

Figure 2.8: THz sources as a function of frequency [68]

2.3 FUNDAMENTALS OF A UTC-PD

In this section, the concept and the fundamental theory of a UTC-PD is introduced first, then a brief literature review of the technological progress that has been made to improve the performance of the UTC-PDs in terms of responsivity and bandwidth is presented.

2.3.1 Basic device structure

The basic device structure of a UTC-PD is illustrated in figure 2.4 showing that it has similarities to a p-i-n diode. One key difference is the presence of a diffusion block layer on the left side of the absorption region before the p-contact. This layer prevents the movement of holes towards the p-contact, allowing only electrons to proceed towards the n-contact. The UTC-PD consists of an active region with a p-type light absorption layer and a lightly doped n-type carrier-collection layer. The widths of the absorption and collection layers are represented as W_A and W_C in figure 2.4, respectively. Other structures have been developed to reduce dark current [69] and diode capacitance [70], but they are not considered ultrafast photo-response diodes due to their limited bandwidth and speed. The doping densities of the UTC-PD absorption and collection regions are $p = 1\text{x}10^{24}$ m^{-3} and $n = 1\text{x}10^{22}$ m^{-3} respectively [71]. The absorption layer is made of $In_{0.53}Ga_{0.47}As$, which has a lattice match with the InP collection layer on InP substrate. The band gap, which is the difference between the conduction band and valence band edges, is relatively

narrow at 0.75 eV for InGaAs compared to the 1.35 eV InP collector. This narrow band gap material can absorb optical signals at a wavelength of 1550 nm, creating electron-hole pairs, while the wide band gap material remains transparent to the illuminated light.

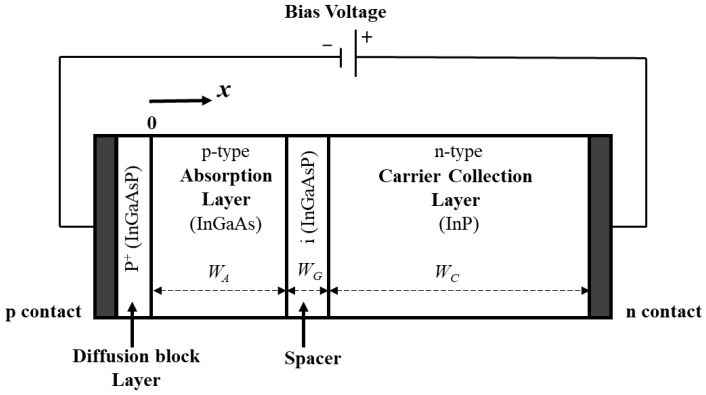

Figure 2.9: UTC-PD basic structure

The UTC-PD utilizes a hetero-junction which is formed between two lattice-matched semiconductors with different band gaps. This hetero-junction plays a crucial role in the optical confinement during the absorption process, thanks to the difference in band gaps between the absorption and collection layers. Additionally, the hetero-junction helps in reducing the dark current. Specifically, the InGaAs/InP hetero-junction employed in the UTC-PD is of type-i. In this type of hetero-junction, the conduction band (CB) and valence band (VB) edges of the material with the smaller band gap lie between the material with the larger band gap, resulting in an abrupt junction due to band discontinuity. As a result, electrons move through the hetero-junction from the semiconductor with the higher Fermi-level to the one with the lower Fermi-level. To balance this transfer, a potential spike is introduced at the junction. However, the presence of this potential spike at the hetero interface tends to decrease the speed of the photogenerated active carriers. To overcome this issue and enhance the device's speed, it is necessary to smoothen the junction potential. This can be achieved by inserting an intermediate very thin intrinsic type grading layer made of $In_{0.75}Ga_{0.25}As_{0.53}P_{0.47}$ material, which has a band gap of 1 eV. This spacer grading layer of 10 nm has a step-graded band gap profile and is positioned between the absorber and the collector to smoothen the energy band discontinuities. As illustrated in figure 2.4, its width is denoted by W_G. The UTC-PD band diagram is shown in figure 2.5.

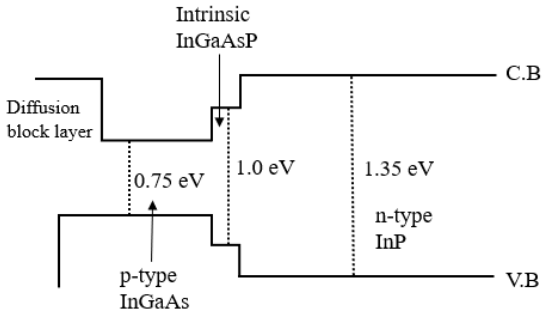

Figure 2.10: Basic UTC-PD band diagram

2.3.2 UTC-PD Operating principle

The UTC-PD is an opto-electronic device that operates under reverse bias conditions. In this configuration, the positive terminal of the external bias voltage is connected to the n-contact, while the negative terminal is connected to the p-contact side. When a 1550 nm wavelength light is directed at the UTC-PD, only the narrow band gap InGaAs absorption layer absorbs the light, generating electron-hole pairs when there is optical excitation. The photogenerated electrons occupy energy states in the conduction band (CB) of the active region material, leaving holes in the valence band (VB). However, due to the presence of a p-n junction, an inherent electric field is formed at the junction even without any external bias. This electric field effectively separates the photogenerated electrons in the CB and the holes in the VB, preventing them from recombining.

When a reverse bias is applied externally to the UTC-PD, the electrons in the CB move towards the n-contact, while the holes in the VB tend to move towards the p-contact. However, the higher doping concentration (p+) diffusion block layer at the p-contact side hinders the movement of holes, preventing them from reaching the p contact. Consequently, the holes cannot contribute to the photo-generated current in the external circuitry. This is the main distinction in operating principle of the UTC-PD as compared to other conventional p-i-n photodiode. The diffusion block layer causes the confined photogenerated majority carrier holes to relax without transport, following the dielectric relaxation time (τ_R). The holes near the p-contact side accumulate within the absorption region, creating a quasi-neutral state. This accumulation of holes leads to the development of a unique electric field called the self-induced field in the quasi-neutral absorption region. The nature of this internal self-induced field and its advantages in UTC-PD operation is further discussed in section 2.3.4. On the other hand, the photogenerated minority electrons diffuse through the absorption layer and drift to the collection layer. Electrons are

collected at the n-contact, and they are the only active carriers that can contribute to the external current. Due to high velocity active carrier electrons, UTC-PD offers very high speed and high bandwidth. In case of pin photodiode both electrons and holes contribute to the carrier transport in the absorption layer. As electrons and holes both travel independently in a pin photodiode, the device response is the aggregate of both current components. Due to the significant difference in carrier velocities, the low velocity holes control the response to limit the bandwidth of the pin diode. A brief discussion on the advantages of a UTC-PD over conventional photodiodes is given in the next section.

2.3.3 Advantages of the UTC-PD over the conventional p-i-n photodiode

1. The primary benefit of UTC-PD lies in its enhanced device operation speed, attributed to the significant disparity in carrier transport properties between electrons and holes. With an average electron velocity ranging from $4x10^7$ cm/s to $6x10^7$ cm/s [79], which is ten orders of magnitude higher than the hole drift velocity of $5x10^6$ cm/s in the depletion layer, the UTC-PD achieves remarkable speed. Figure 2.6 that compares the measured and calculated frequency dependence of THz-wave output at 6 mA photocurrent and a bias voltage of -0.4 V for effective electron velocities between 1 x 10^7 cm/s to 6 x 10^7 cm/s. It was found that static saturation velocity, 1 x 10^7 cm/s to 2 x 10^7 cm/s, never fitted the measured output variation with frequency but rather a reasonable fitting was obtained 4 x 10^7 cm/s to 6 x 10^7 cm/s.

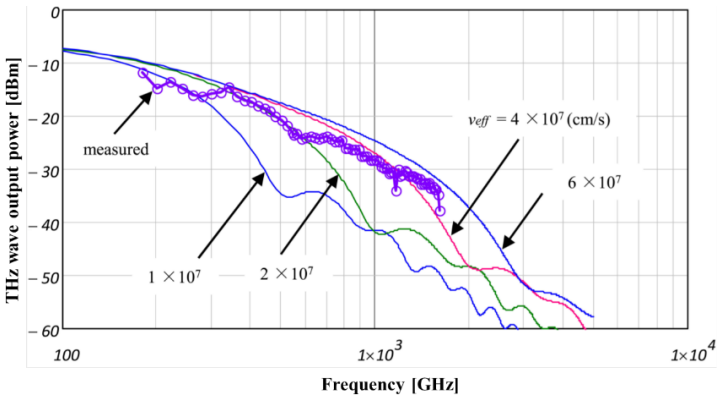

Figure 2.11: Bow-tie integrated UTC-PD measured and calculated frequency response for different effective electron velocity [79]

2. The UTC-PD structure allows for independent design of a small photo-absorption region and a comparatively wide carrier collection layer, thereby optimizing its performance. The reduced

carrier transit time is facilitated by the small absorption layer, while the thick collection layer contributes to a large junction capacitance. Consequently, the UTC-PD can achieve an extremely high bandwidth by utilizing a very thin absorption layer without compromising the charging time of the capacitance-resistance (CR) circuit. This advantage sets it apart from the pin PD, where the carrier generation and collection regions are the same, resulting in a significantly longer CR charging time even with reduced absorption layer thickness to minimize carrier transit time [72].

3. The UTC-PD offers another advantage in the form of a higher output saturation current at high optical power. This is attributed to the reduced space charge effect in the depletion layer, which is a result of the decrease in electron velocity within the depletion layer. In figure 2.7 (a) and (b), the carrier distributions in the UTC-PD and pin photodiode are depicted under low optical illumination. Additionally, figure 2.8 (a) and (b) illustrate the band bending that occurs at high carrier injection levels for both the UTC-PD and pin photodiode structures, respectively. Under high optical illumination, a significant number of photogenerated carriers are produced and travel towards the contact sides. In the pin photodiode, the slow velocity positively charged holes primarily accumulate at the n-contact side within the absorption layer, resulting in a modified band profile as shown in figure 2.8 (b).

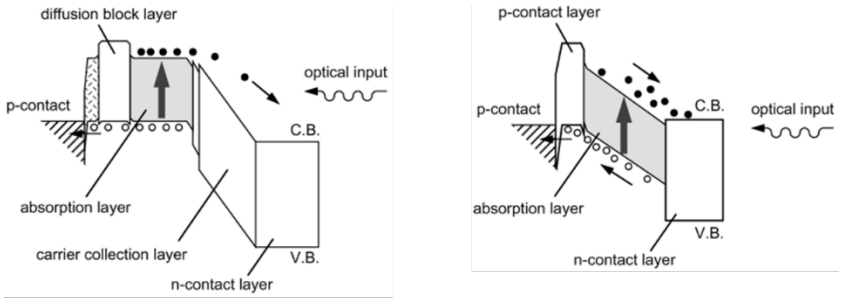

Figure 2.12: Band profile for low optical input of (a) UTC-PD and (b) pin photodiode [72]

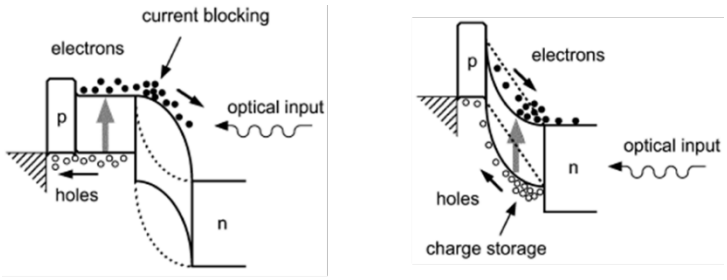

(a) (b)

Figure 2.13: Modified band bending for high optical input of (a) UTC-PD and (b) pin photodiode [72]

In contrast, the space charge in the UTC-PD consists solely of high velocity electrons, which are uniformly distributed under high-excitation conditions. Figure 2.8 (a) demonstrates the band bending caused by the accumulation of negative space charge at the collector junction in the UTC-PD under high input. Even with a decreased electric field, the electron velocity at overshoot in the UTC-PD remains significantly higher than the drift velocity of holes in the pin photodiode. As a result, the UTC-PD's output current does not saturate until the current density reaches an order of magnitude higher than that of the pin photodiode.

4. The decrease in hole velocity in pin photodiodes can cause output saturation, even at low current densities. However, in UTC-PD, the reduction in electron velocity and output saturation only occurs when the electric field decreases significantly [73]. As a result, UTC-PD has a wider linearity range compared to conventional pin photodiodes, making it a suitable option for photonic transmitter applications.

5. In addition to its high speed and high bandwidth capabilities, another significant advantage of UTC-PD is the ability to maintain high-saturation output at a low (or even zero) bias voltage [74]. This is made possible by the high electron velocity in the depletion layer, which can be sustained with a relatively low applied bias [73], or, in the absence of bias, an induced electric field is created at the absorption region due to hole accumulation. Consequently, the high-speed performance of the UTC-PD remains unaffected even when no bias voltage is present [74]. A lower operating voltage offers various benefits, including reduced power consumption, simplified heat dissipation, lower biasing circuit expenses, and enhanced reliability.

2.3.4 The Electric Field Profile of the UTC-PD

The electric field profile in a UTC-PD is similar to that of a p-n junction however, it's modified in the absorption layer because of the diffusion block layer. An internal field originating from the accumulation of holes is known as self-induced field and is denoted by $E_{ind}(x)$. The variation of $E_{ind}(x)$ in the quasi-neutral absorption region of the UTC-PD is linear [75] and is given as

$$E_{ind}(x) = E_{ind0}\left(1 - \frac{x}{W_A}\right) \qquad (2-8)$$

where E_{ind0} is the maximum induced electric field at the edge of the absorption layer ($x = 0$). The self-induced field then decays towards the p-n junction and becomes zero ($E_{ind}(x) = 0$) at ($x = W_A$). This implies that $E_{ind}(x)$ dominates and controls the carrier velocity within the absorption region and the photo-generated minority electrons are accelerated mainly by this internally generated induced electric field. Under such conditions, the electron transport shifts from diffusion to drift motion [72], and this is the reason why the UTC-PD can work with a very low external bias (even at 0 V) [74] which is not possible in a conventional p-i-n photodiode.

The variation of the total electric field E which is a combination of $E_{ind}(x)$ and $E_b(x)$ along the device length is illustrated in figure 2.9.

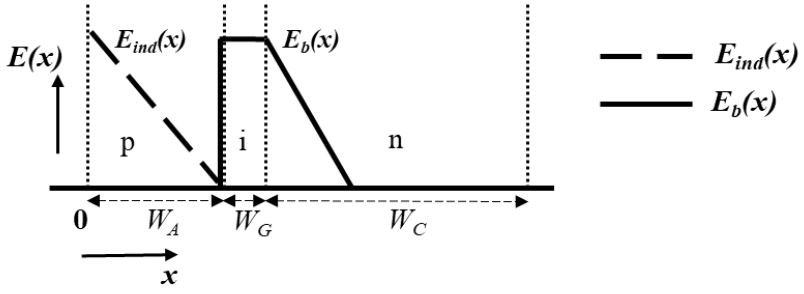

Figure 2.14: Electric field profile in a UTC-PD

The solid line represents the bias field $E_b(x)$ caused by the external bias V_b, while the dashed line represents the variation of the self-induced field $E_{ind}(x)$. The acceptor and donor doping concentrations in the absorption and collection regions are high, resulting in a maximum bias field in the intrinsic layer. This bias field decreases on both sides of the intrinsic grading layer.

Due to the narrow width of the intrinsic grading layer, which can be as low as 10 nm to 15 nm, the maximum value of $E_b(x)$ is observed at the input of the collector junction. The electric field at the collector input is denoted by E_C which can be given as [76]

$$E_C = \frac{V_{op}}{W_C} + qW_C\left(\frac{N-n}{2\varepsilon_0\varepsilon_r}\right) \qquad (2-9)$$

where the electronic charge $q = 1.6 \times 10^{-19}C$, the free space permittivity $\varepsilon_0 = 8.85 \times 10^{-12}F/m$ and $\varepsilon_r = 9.61$ is the relative permittivity of InP material at high frequencies [77]. N is the donor density, n is the electron carrier density, and V_{op} is operating voltage across the photodiode which is a function of bias voltage. Hence the value of E_C is fixed for a given bias voltage, input optical power, doping density in the collection layer and width of the collection layer.

2.3.5 The Space-Charge Effect

The space-charge effect is a crucial factor that impacts the output linearity and device saturation. It is characterized by a decrease in the electric field E_C at the collector junction input when there is high current injection. This effect, caused by the presence of photo-generated carriers, is always present in a photodiode and is influenced by factors such as current density, carrier velocities, applied bias voltage, and the type of traveling carriers (electrons or holes). The density of space charge tends to increase with higher levels of light injection. At high optical intensities, mobile charges can accumulate in the depletion region, leading to a decrease in the electric field. This decrease in electric field reduces carrier velocity, resulting in the accumulation of space charge, further reducing the electric field in a detrimental feedback loop. This process, known as the space-charge effect, can cause the electric field in the absorption region to collapse under sufficient illumination, leading to strong output saturation and an increase in nonlinear photo-response.

2.3.6 Frequency response

The frequency response of UTC-PD can be calculated from its schematic layout in figure 2.4. The total diode current J_{tot} is the sum of electron current J_e, hole current J_h and displacement current $\varepsilon\frac{\partial E}{\partial t}$ integrated over the total diode thickness W.

$$J_{tot} = \frac{1}{W}\int_0^W \left[J_e + J_h + \varepsilon\frac{\partial E}{\partial t}\right] dx \qquad (2-10)$$

where W is the sum of absorption layer width W_A and collection layer width W_C. $\varepsilon = \varepsilon_0\varepsilon_r$. The conduction current in the collection layer consists of only electron current which is equal to the injection current $J_e(W_A)$ from the absorption layer. In short circuit condition, the integration of $\frac{\partial E}{\partial t}$ over the diode length is 0 as $\int_0^W E\,dx$ is a constant.

Accordingly, equation $(2-10)$ can be separated into two terms as

$$J_{tot} = \frac{1}{W}\int_0^{W_A} (J_e + J_h)\,dx + \frac{1}{W}\int_{W_A}^{W_C} J_e\,dx \qquad (2-11)$$

where the 1st and 2nd terms are the responses for the absorption and carrier collection layers respectively.

The relationship between the hole current density and electric field is given as

$$J_h = qp\mu_n E \qquad (2-12)$$

where μ_n is the mobility of electrons in the absorption region.

Let us assume that the electric field E has a small signal perturbation that temporarily varies as $\exp(j\omega t)$, where ω is the angular frequency. From the current continuity relation $J_e + J_h + \varepsilon\frac{\partial E}{\partial t} = constant$, we can have

$$\frac{\partial}{\partial x}(J_e + J_h) = -j\omega\frac{\partial E}{\partial x} \qquad (2-13)$$

The dielectric relaxation time τ_R of the photogenerated holes in the absorption layer can be expressed as

$$\tau_R = \frac{\varepsilon}{qp\mu_n} \qquad (2-14)$$

Hence, using equation $(2-11)$, $\frac{\partial}{\partial x}(J_e + J_h)$ can be rewritten as

$$\frac{\partial}{\partial x}(J_e + J_h) = \frac{j\omega\tau_R}{1 + j\omega\tau_R}\frac{\partial J_e}{\partial x} \qquad (2-15)$$

Integrating both side of equation $(2-14)$ over the absorption length with boundary conditions, $J_e(W_A)$ and $J_h = 0$ at $x = W_A$ we get the total current density as

$$J_e + J_h = J_e(W_A)\left[1 - \frac{j\omega\tau_R}{1 + j\omega\tau_R}\left(1 - \frac{J_e(x)}{J_e(W_A)}\right)\right] \qquad (2-16)$$

From the above equation, it is ascertained that the hole conduction current vanishes at frequency $\omega \gg \frac{1}{\tau_R}$. For instance, considering a typical p-type InGaAs with p = 1x10^{24} m^{-3} lattice matched to InP, $\frac{1}{\tau_R}$ can be as high as 30 THz. Hence, the dielectric relaxation process of holes does not limit the frequency response of UTC-PD.

In small signal condition, the induced collector current can be reduced to [78]

$$\int_{W_A}^{W_C} J_e\, dx = \frac{W_C}{W} J_e(W_A, \omega)\frac{\sin\left(\frac{\omega\tau_C}{2}\right)}{\left(\frac{\omega\tau_C}{2}\right)} exp\left(-\frac{j\omega\tau_C}{2}\right) \qquad (2-17)$$

where $\tau_C = \frac{W_C}{v_e}$ is the electron traveling time through the collector at a constant velocity of electrons v_e.

Finally, the UTC-PD frequency response can be formulated from equation $(2-11)$ by substituting the values of $J_e + J_h$ and $\int_{W_A}^{W_C} J_e\, dx$ as

$$J_{tot}(\omega) = \frac{1}{W}\int_0^{W_A}\left[J_e(W_A, \omega)\left\{1 - \frac{j\omega\tau_R}{1 + j\omega\tau_R}\left(1 - \frac{J_e(x, \omega)}{J_e(W_A, \omega)}\right)\right\}\right] dx + \frac{W_C}{W} J_e(W_A, \omega)\frac{\sin\left(\frac{\omega\tau_C}{2}\right)}{\left(\frac{\omega\tau_C}{2}\right)} exp\left(-\frac{j\omega\tau_C}{2}\right) \qquad (2-18)$$

2.4 CHRONOLOGICAL DEVELOPMENT OF UTC-PDs

UTC-PDs have been the subject of continuous investigation in order to enhance their performance. This research is particularly active in the fields of microwave and terahertz photonics. Additionally, the packaging technology for UTC-PDs has posed a significant challenge. Currently, fiber-pigtailed UTC-PD modules with various output interfaces, such as coaxial, rectangular-waveguide, or integrated planar antenna, are available, covering a wide frequency range of up to approximately 4.5 THz [72], [79], [80].

Prior to the proposal of the UTC-PD concept, similar structures incorporating depleted InP material had already been reported. The previous objectives were to reduce dark current and increase the voltage amplitude during operation [69], [70]. Therefore, while the UTC design was not entirely unique, its key message emphasized the elimination of hole transport in photodiode operation, relying solely on electron transport for superior high-speed and high-output performance. This argument is valid only if the device exhibits quasi-ballistic electron transport or velocity overshoot. In comparison to holes in InGaAs, electrons in InGaAs and InP can drift at significantly higher velocities, thanks to their quasi-ballistic nature, by an order of magnitude. Moreover, the relatively large energy separation from Γ- to L-valley minima in InP provides an important advantage. The potential of this quasi-ballistic electron transport in III-V materials was already considered in the 1990s, although it was not necessarily acknowledged as a realistic phenomenon. Furthermore, in order to maintain a fast photo-response speed, the minority electron transport in the p-type absorption layer, typically composed of InGaAs, must not pose a significant limitation.

In the initial phase of development, the sensitivity of a UTC-PD was not considered a critical aspect. Nonetheless, the introduction of a design concept incorporating a combined p-type neutral and depleted absorber, derived from UTC design principles, quickly gained prominence. Traditional UTC-PD designs were utilized for zero-bias operation, resulting in successful 100-GHz operation [81].

A schematic representation in figure 2.10 [82] illustrates the UTC-PD and modified UTC-PD (MUTC-PD) structures. The modification involves the replacement of a section of the wide-gap depletion layer in a UTC structure with a depleted absorber. Due to the proximity of the

depleted absorber to the p-type absorber, the electron current continues to dominate the overall induced current, preserving the characteristic features of UTC-PD.

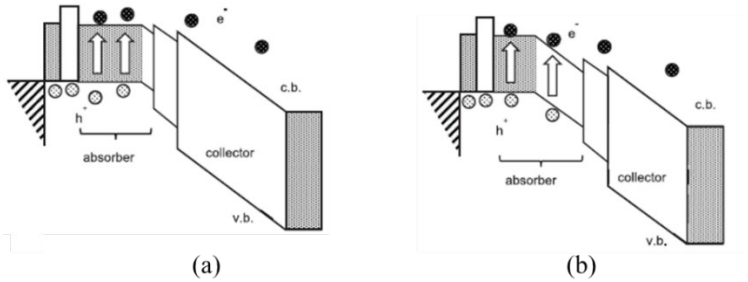

Figure 2.15: Schematic band diagrams for UTC-PD and modified UTC-PD

The speed at which minority electrons drift/diffuse in a p-type neutral absorber is much slower than in a depleted absorber. Therefore, dividing the absorber thickness W_A into W_{AN} for a neutral and W_{AD} for a depleted thickness can reduce the original delay time. Even though hole current adds to electron current, this additional hole current does not necessarily slow down the response. As a result, the modified (or hybrid absorber, maximum induced current, partially depleted, near ballistic, etc.) design offers the crucial advantage of optimizing overall performance. For instance, with a given absorber volume W_A and junction capacitance, adjusting W_{AN} and W_{AD} can maximize the bandwidth of an MUTC-PD. A set of absorber partitions determined in this manner simultaneously provides the highest responsivity for a target (required) bandwidth or f_{3dB} of photo-response [79]. To further enhance photodiode performance, it remains important to understand their output linearity or output saturation due to the carrier space charge effect. Recent publications have discussed output power levels and how diode structures are linked to output saturation [83–87]. The carrier space charge effect, especially in a modified UTC-PD, exhibits a behavior that is highly complex to predict accurately. This complexity arises from the nonlinear response of drifting carriers and electron/hole currents in large signal conditions [82].

2.5 Conclusion

This chapter has provided a comprehensive review of the two THz wave generation technologies: electronics-based and photonics-based technologies. State of the art advances in the electronic implementation of THz sources including CMOS technology, HBTs and HEMTs, RTDs, as well as SBDs have been discussed. Even so, challenges and limitations associated with these

electronic sources including issues related with drastic power decrement at higher frequencies, have been highlighted.

Furthermore, a thorough account on photonic THz sources has been given. The chapter has delved into the photomixing concept, an optoelectronic technology that enables the conversion of two lightwaves with different frequencies into an alternating current with a frequency equal to the frequency difference of the two lightwaves using a photodiode or a photoconductor. This technology has been used throughout the experimental work conducted in this research. Lastly, a detailed account of the fundamental principles and chronological development of a UTC-PD establishing a theoretical foundation for the experimental work presented in Chapters 4 and 5.

REFERENCES

[1] C. Zandonella, “Terahertz imaging: T-ray specs,” Nature, vol. 424, no. 6950, p. 721, Aug. 2003.

[2] E. Seok et al., “A 410GHz CMOS push-push oscillator with an on-chip patch antenna,” in Proc. IEEE Int. Solid-State Circuits Conf. Tech. Papers, 2008, pp. 472–629.

[3] Z. Ahmad, M. Lee, and K. O. Kenneth, “20.5 1.4 THz,− 13dBm-EIRP frequency multiplier chain using symmetric- and asymmetric-CV varactors in 65nm CMOS,” in Proc. IEEE Int. Solid-State Circuits Conf., 2016, pp. 350–351.

[4] B. Khamaisi, S. Jameson, and E. Socher, “A 0.58–0.61 THz single on-chip antenna transceiver based on active X30 LO chain on 65nm CMOS,” in Proc. IEEE 11th Eur. Microw. Integr. Circuits Conf., 2016, pp. 97–100.

[5] E. Öjefors, J. Grzyb, Y. Zhao, B. Heinemann, B. Tillack, and U. R. Pfeiffer, “A 820GHz SiGe chipset for terahertz active imaging applications,” in Proc. IEEE Int. Solid-State Circuits Conf., 2011, pp. 224–226.

[6] H. Aghasi, A. Cathelin, and E. Afshari, “A 0.92-thz SiGe power radiator based on a nonlinear theory for harmonic generation,” IEEE J. Solid-State Circuits, vol. 52, no. 2, pp. 406–422, Feb. 2017.

[7] S. Jameson and E. Socher, “High efficiency 293 GHz radiating source in 65 nm CMOS,” IEEE Microw. Wireless Compon. Lett., vol. 24, no. 7, pp. 463–465, Jul. 2014.

[8] B. Khamaisi, S. Jameson, and E. Socher, “0.61 THz radiating source with on-chip antenna on 65nm CMOS,” in Proc. IEEE 11th Eur. Microw. Integr. Circuits Conf., 2016, pp. 389–392.

[9] L. Gao and C. H. Chan, “A 0.68–0.72-thz 2-D scalable radiator array with–3-dBm radiated power and 27.3-dBm EIRP in 65-nm CMOS,” IEEE J. Solid-State Circuits, vol. 57, no. 10, pp. 3114–3124, Oct. 2022.

[10] H. Jalili and O. Momeni, “A 0.46-thz 25-element scalable and wideband radiator array with optimized lens integration in 65-nm CMOS,” IEEE J. Solid-State Circuits, vol. 55, no. 9, pp. 2387–2400, Sep. 2020.

[11] Y. Tousi and E. Afshari, “A high-power and scalable 2-D phased array for terahertz CMOS integrated systems,” IEEE J. Solid-State Circuits, vol. 50, no. 2, pp. 597–609, Feb. 2015.

[12] Y. Zhao et al., “A 0.54-0.55 THz 2× 4 coherent source array with EIRP of 24.4 dBm in 65nm CMOS technology,” in Proc. IEEE MTT-S Int. Microw. Symp., 2015, pp. 1–3.

[13] R. Han and E. Afshari, “A CMOS high-power broadband 260-GHz radiator array for spectroscopy,” IEEE J. Solid-State Circuits, vol. 48, no. 12, pp. 3090–3104, Dec. 2013.

[14] G. Guimarães and P. Reynaert, “A 670-GHz 4× 2 oscillator–radiator array achieving 7.4-dBm EIRP in 40-nm CMOS,” IEEE J. Solid-State Circuits, vol. 56, no. 11, pp. 3399–3411, Nov. 2021.

[15] Z. Hu, M. Kaynak, and R. Han, “High-power radiation at 1 THz in silicon: A fully scalable array using a multi-functional radiating mesh structure,” IEEE J. Solid-State Circuits, vol. 53, no. 5, pp. 1313–1327, May 2018.

[16] B. Heinemann et al., “SiGe HBT with fx/fmax of 505 GHz/720 GHz,” in Proc. IEEE Int. Electron Devices Meeting, 2016, pp. 3.1.1–3.1.4.

[17] M. Urteaga, R. Pierson, P. Rowell, V. Jain, E. Lobisser, and M. J. W. Rodwell, “130nm InP DHBTs with ft>0.52 thz and f max>1.1 THz,” in Proc. IEEE 69th Device Res. Conf., 2011, pp. 281–282.

[18] M. J. Rodwell, M. Le, and B. Brar, “InP bipolar ICs: Scaling roadmaps, frequency limits, manufacturable technologies,” in Proc. IEEE, vol. 96, no. 2, pp. 271–286, Feb. 2008.

[19] J. Wittemeier, F. Vogelsang, D. Starke, H. Rücker, and N. Pohl, “A SiGe based 0.48 THz signal source with 45 GHz tuning range,” in Proc. IEEE 51st Eur. Microw. Conf., 2022, pp. 869–872.

[20] R. Jain, P. Hillger, E. Ashna, J. Grzyb, and U. R. Pfeiffer, “A 64-pixel 0.42-THz source SoC with spatial modulation diversity for computational imaging,” IEEE J. Solid-State Circuits, vol. 55, no. 12, pp. 3281–3293, Dec. 2020.

[21] S. Razavian and A. Babakhani, “Silicon integrated THz comb radiator and receiver for broadband sensing and imaging applications,” IEEE Trans. Microw. Theory Techn., vol. 69, no. 11, pp. 4937–4950, Nov. 2021.

[22] A. M. Arabhavi et al., “InP/GaAsSb double heterojunction bipolar transistor emitter-fin technology with f MAX= 1.2 THz,” IEEE Trans. Electron Devices, vol. 69, no. 4, pp. 2122–2129, Apr. 2022.

[23] W. Deal, K. Leong, A. Zamora, V. Radisic, and X. B. Mei, “Recent progress in scaling InP HEMT TMIC technology to 850 GHz,” in Proc. IEEE MTT-S Int. Microw. Symp., 2014 pp. 1–3.

[24] X. Mei et al., “First demonstration of amplification at 1 THz using 25-nm InP high electron mobility transistor process,” IEEE Electron Device Lett., vol. 36, no. 4, pp. 327–329, Apr. 2015.

[25] A. Leuther et al., “20 nm metamorphic HEMT technology for terahertz monolithic integrated circuits,” in Proc. IEEE 9th Eur. Microw. Integr. Circuit Conf., 2014, pp. 84–87.

[26] G. Chattopadhyay et al., “A 340 GHz cryogenic amplifier based spectrometer for space based atmospheric science applications,” in Proc. IEEE 42nd Int. Conf. Infrared , Millimeter , Terahertz Waves, 2017, pp. 1–2.

[27] A. Zamora et al., “A high efficiency 670 GHz x36 InP HEMT multiplier chain,” in Proc. IEEE MTT-S Int. Microw. Symp., 2017, pp. 977–979.

[28] H. Wang et al., “Power amplifiers performance survey 2000-present,” Georgia Tech Electronics and Micro-System Lab (GEMS), version-6 release, Aug. 2021.

[29] M. Seo et al., “InP HBT IC technology for terahertz frequencies: Fundamental oscillators up to 0.57 THz,” IEEE J. Solid-State Circuits, vol. 46, no. 10, pp. 2203–2214, Oct. 2011.

[30] A. Possberg et al., “An injection-lockable InP-DHBT source operating at 421 GHz with− 2.4 dBm output power and 1.7% DC-to-RF efficiency,” in Proc. IEEE/MTT-S Int. Microw. Symp., 2022, pp. 336–339.

[31] T. Maekawa, H. Kanaya, S. Suzuki, and M. Asada, “Oscillation up to 1.92 THz in resonant tunneling diode by reduced conduction loss,” Appl. Phys. Exp., vol. 9, no. 2, 2016, Art. no. 024101.

[32] K. Arzi et al., “Subharmonic injection locking for phase and frequency control of RTD-based THz oscillator,” IEEE Trans. Terahertz Sci. Technol., vol. 10, no. 2, pp. 221–224, Mar. 2020.

[33] Y. Koyama et al., “A high-power terahertz source over 10 mW at 0.45 THz using an active antenna array with integrated patch antennas and resonant-tunneling diodes,” IEEE Trans. Terahertz Sci. Technol., vol. 12, no. 5, pp. 510–519, Sep. 2022. [

34] I. Mehdi, J. V. Siles, C. Lee, and E. Schlecht, “THz diode technology: Status, prospects, and applications,” Proc. IEEE, vol. 105, no. 6, pp. 990–1007, Jun. 2017.

[35] W. Kou et al., “A review of Terahertz sources based on Planar Schottky Diodes,” Chin. J. Electron., vol. 31, no. 3, pp. 467–487, 2022.

[36] T. Takada and M. Ohmori, “Frequency triplers and quadruplers with GaAs Schottky-barrier diodes at 450 and 600 GHz,” IEEE Trans. Microw. Theory Techn., vol. MTT-27, no. 5, pp. 519–523, May 1979.

[37] J. W. Archer, “Millimeter wavelength frequency multipliers,” IEEE Trans. Microw. Theory Techn., vol. MTT-29, no. 6, pp. 552–557, Jun. 1981.

[38] W. L. Bishop, K. McKinney, R. J. Mattauch, T. W. Crowe, and G. Green, “A novel whiskerless Schottky diode for millimeter and submillimeter wave application,” in Proc. IEEE MTT-S Int. Microw. Symp., 1987, pp. 607–610.

[39] A. Maestrini, D. Pukala, F. Maiwald, E. Schlecht, G. Chattopadhyay, and I.Mehdi, “Cryogenic operation of GaAs based multiplier chains to 400 GHz,” in Proc. 8th Int. Conf. THz Electron., Sep. 2000, pp. 81–84.

[40] C.-I. Lin et al., “Anti-parallel planar Schottky diodes for subharmonically-pumped 220 GHz/mixer,” in Proc. 10th Int. Symp. Space Terahertz Technol., 1999, Art. no. 85.

[41] S. Martin et al., “Fabrication of 200 to 2700 GHz multiplier devices using GaAs and metal membranes,” in Proc. IEEE MTT-S Int. Microw. Symp., 2001, pp. 1641–1644.

[42] L. Qian, A. Ning, and X. Tong, “Planar Schottky barrier diode with cut-off frequency of 8.7 THz,” J. Terahertz Sci. Electron. Inf. Technol., vol. 13, no. 5, pp. 679–683, 2015.

[43] H. Liu, J. Powell, C. Viegas, A. A. Cairns, and B. Alderman, “A 332GHz frequency doubler using flip-chip mounted planar schottky diodes,” in Proc. IEEE Asia-Pacific Microw. Conf., 2015, pp. 1–3.

[44] D. W. Porterfield, “High-efficiency terahertz frequency triplers,” in Proc. IEEE/MTT-S Int. Microw. Symp., 2007, pp. 337–340. [

45] Accessed: [Online]. Available: www.acst.de

[46] A. Maestrini et al., “A 540-640-GHz high-efficiency four-anode frequency tripler,” IEEE Trans. Microw. Theory Techn., vol. 53, no. 9, pp. 2835–2843, Sep. 2005.

[47] A. Maestrini et al., “Design and characterization of a room temperature all-solid-state electronic source tunable from 2.48 to 2.75 THz,” IEEE Trans. Terahertz Sci. Technol., vol. 2, no. 2, pp. 177–185, Mar. 2012.

[48] J. C. Pearson et al., “Demonstration of a room temperature 2.48–2.75 THz coherent spectroscopy source,” Rev. Sci. Instrum., vol. 82, no. 9, 2011, Art. no. 093105.

[49] G. Chattopadhyay et al., “An all-solid-state broad-band frequency multiplier chain at 1500 GHz,” IEEE Trans. Microw. Theory Techn., vol. 52, no. 5, pp. 1538–1547, May 2004.

[50] J. V. Siles et al., “A multi-pixel room-temperature local oscillator subsystem for array receivers at 1.9 THz,” Proc. SPIE, vol. 9147, pp. 2275–2280, 2014.

[51] D. Moro-Melgar, O. Cojocari, and I. Oprea, “High power high efficiency 270–320 GHz source based on discrete Schottky diodes,” in Proc. IEEE 15th Eur. Radar Conf., 2018, pp. 337–340.

[52] E. Bryerton, S. Retzloff, and J. Hesler, “High-power submillimeter wave solid-state sources,” in Proc. IEEE 12th Glob. Symp. Millimeter Waves, 2019, pp. 29–31.

[53] N. Alijabbari, M. F. Bauwens, and R. M. Weikle, “Design and characterization of integrated submillimeter-wave quasi-vertical Schottky diodes,” IEEE Trans. Terahertz Sci. Technol., vol. 5, no. 1, pp. 73–80, Jan. 2014.

[54] B. Alderman et al., “High power frequency multipliers to 330 GHz,” in Proc. IEEE 5th Eur.Microw. Integr. Circuits Conf., 2010, pp. 232–233.

[55] C. Lee et al., “Diamond heat-spreaders for submillimeter-wave GaAs Schottky diode frequency multipliers,” in Proc. 20th Int. Symp. Space Terahertz Technol., 2009, pp. 43–46.

[56] A. Y. Tang et al., “Steady-state and transient thermal analysis of high-power planar Schottky diodes,” in Proc. 22nd Int. Symp. Space Terahertz Technol., 2011, pp. 1–7.

[57] O. Cojocari, I. Oprea, H. Gibson, and A.Walber, “SubMM-wave multipliers by film-diode technology,” in Proc. IEEE 46th Eur. Microw. Conf., 2016, pp. 337–340.

[58] D. Moro-Melgar, O. Cojocari, I. Oprea, M. Hoefle, and M. Rickes, “Reliability and reproducibility of discrete Schottky diodes- based sources up to 370 ghz,” in Proc. IEEE 30th Int. Symp. Space THz Technol., 2019, p. 26.

[59] J. V. Siles, K. B. Cooper, C. Lee, R. H. Lin, G. Chattopadhyay, and I. Mehdi, “A new generation of room-temperature frequency-multiplied sources with up to 10× higher output power in the 160-GHz–1.6-THz range,” IEEE Trans. Terahertz Sci. Technol., vol. 8, no. 6, pp. 596–604, Jun. 2018.

[60] B. S. Williams, “Terahertz quantum-cascade lasers,” Nature Photon., vol. 1, no. 9, pp. 517–525, 2007.

[61] X. Wang et al., “High-power terahertz quantum cascade lasers with 0.23 W in continuous wave mode,” AIP Adv., vol. 6, no. 7, Jul. 2016, Art. no. 075210.

[62] Q. Lu, F. Wang, D. Wu, S. Slivken, and M. Razeghi, “Room temperature terahertz semiconductor frequency comb,” Nature Commun., vol. 10, no. 1, pp. 1–7, Dec. 2019.

[63] A. Khalatpour, A. K. Paulsen, C. Deimert, Z. R. Wasilewski, and Q. Hu, “High-power portable terahertz laser systems,” Nature Photon., vol. 15, no. 1, pp. 16–20, Jan. 2021.

[64] N. M. Burford and M. O. El-Shenawee, “Review of terahertz photoconductive antenna technology,” Opt. Eng., vol. 56, no. 1, Jan. 2017, Art. no. 010901.

[65] N. T. Yardimci and M. Jarrahi, “Nanostructure-enhanced photoconductive terahertz emission and detection,” Small, vol. 14, no. 44, Nov. 2018, Art. no. 1802437.

[66] M. Martin and E. R. Brown, “Critical comparison of GaAs and InGaAs THz photoconductors,” in Terahertz Technology and Applications V, 2012, vol. 8261.

[67] T. Nagatsuma, “Photonic generation of millimeter waves and its applications,” in Optics InfoBase Conference Papers, 2012.

[68] M. Tonouchi, “Cutting-edge terahertz technology,” Nature Photonics, vol.1, no.2, pp.97–105, 2007.

[69] T. P. Pearsall, M. Piskorski, A. Brochet, and J. Chevrier, “A Ga0.47In0.53As/InP heterophotodiode with reduced dark current”, IEEE J. Quantum Electron., vol. QE-17, no.2, pp. 255-259, 1981.

[70] G. A. Davis, R. E. Weiss, R. A. LaRue, K. J. Williams, and R. D. Esmann, “A 920-1650-nm high-current photodetector”, IEEE Photon. Technol. Lett., vol. 8, no. 10, pp. 1373-1375, 1996.

[71] T. Ishibashi, T. Furuta, H. Fushimi, S. Kodama, H. Ito, T. Nagatsuma, N. Shimizu, and Y. Miyamoto, “InP/InGaAs uni-traveling-carrier photodiodes”, IEICE Trans. Electron., vol, E83-C, no. 6, pp. 938–949, 2000.

[72] H. Ito, S. Kodama, Y. Muramoto, T. Furuta, T. Nagatsuma, and T. Ishibashi, “High-speed and high-output InP–InGaAs uni-traveling carrier photodiodes”, IEEE J. Quantum Electron., vol. 10, no. 4, pp. 709–727, Jul./Aug. 2004.

[73] T. Ishibashi, “High speed heterostructure devices”, in Semiconductors and Semimetals. San Diego, CA: Academic, vol. 41, ch. 5, p. 333, 1994.

[74] H. Ito, T. Furuta, S. Kodama, and T. Ishibashi, “Zero-bias high-speed and high-output-voltage operation of cascade-twin uni-travelling-carrier photodiode,” Electron. Lett., vol. 36, pp. 2034–2036, Nov. 2000.

[75] S. Khanra and A. Das Barman, “Photo response haracteristics from computationally efficient dynamic model of uni-traveling carrier photodiode”, Optical and Quantum. Electronics, Springer, vo. 48, no. 2, pp. 1.11, Dec. 2015.

[76] M. Chtioui, A. Enard, D. Carpentier, S. Bernard, B. Rousseau, F. Lelarge, F. Pommereau, and M. Achouche, “High-power high-linearity uni-traveling-carrier photodiodes for analog photonic links”, IEEE Photonics Tech. Lett., vol. 20, no. 3, pp. 202–204, 2008.

[77] http://www.ioffe.ru/SVA/NSM/Semicond/InP/basic.html.

[78] T. Ishibashi, S. Kodama, N. Shimizu, and T. Furuta, “High speed response of uni-traveling carrier photodiodes”, Jpn. J. Appl. Phys., vol. 36, no. 10, pp. 6263-6268, 1997.

[79] T. Ishibashi, Y. Muramoto, T. Yoshimatsu, and H. Ito, “Uni-travelingcarrier photodiodes for terahertz applications,” IEEE J. Sel. Topics Quantum Electron., vol. 20, no. 6, Nov./Dec. 2014.

[80] D. Fukuoka, K.Muro, and K. Noda, “Coherent THz light source based on photo-mixing with a UTC-PD and ASE-free tunable diode lasers,” Proc. SPIE, vol. 9747, pp. 974717–131–974717–7, 2016.

[81] T. Umezawa, K. Akahane, N. Yamamoto, A. Kanno, K. Inagaki, and T. Kawanishi, “Aero-bias operational ultra-bradband UTC-PD abve 100GHz for high symbol rate PD-array in high-density photonic integration,” in Proc. Opt. Fiber Commun. Conf. Exhib., Mar. 2015, Art. no. M3C.7.

[82] T. Ishibashi and H. Ito, "Uni-Traveling Carrier Photodiodes: Development and Prospects," in IEEE Journal of Selected Topics in Quantum Electronics, vol. 28, no. 2: Optical Detectors, pp. 1.6, March-April 2022

[83] A. J. Seeds, H. Shams, M. J. Fice, and C. C. Renaud, “Terahertz photonics for wireless communications,” J. Lightw. Technol., vol. 33, no. 3, pp. 579–587, Feb. 2015.

[84] A. Beling, X. Xie, and J. Campbell, “High-power, high-linearity photodiodes,” Optica, vol. 3, no. 3, pp. 328–338, 2016.

[85] K. Sun and A. Beling, “High-speed photodetectors for microwave photonics,” Appl. Sci., vol. 9, 2019, Art. no. 623.

[86] B.Wang et al., “Toward high-power, high-coherence, integrated photonic mmWave platform with mirocavity solitons,” Light: Sci. Appl., vol. 10, 2021, Art. no. 4.

[87] J. Li et al., “Ultrafast dual-drifting layer uni-traveling carrier photodiode with high saturation current,” Opt. Exp., vol. 24, no. 8, pp. 8420–8428, 2016.

CHAPTER 3

DEVICE DESIGN

3.1 MICROSTRIP LINE TECHNOLOGY

Microstrip line (MSL) is a widely used type of planar transmission line technology primarily because it can be easily fabricated by photolithographic processes and as well miniaturized and integrated with passive and active devices. As depicted in figure 3.1 (a), a microstrip line consists of three primary components: a thin conductor, a dielectric substrate, and a conducting ground plane. The space above the thin conductor is typically air, causing the electric field between the two conductors to traverse two distinct media. Consequently, the electric field *fringes* along the edges.

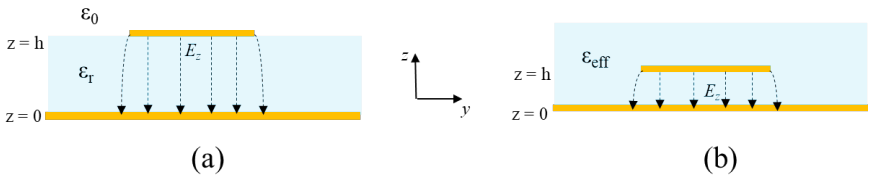

Figure 3.16: Microstrip transmission line; (a) actual configuration, (b) equivalent homogeneous medium

To simplify the analysis of such structures, we need to transform the problem from a field that propagates in two different media (air and substrate) into a field that propagates in a homogeneous medium. As depicted in figure 3.1 (b), this transformation can be done if we assume that the two media are equivalent to a single medium with a specific dielectric constant that is interpreted as the effective dielectric constant ε_{reff} that can be approximated as

$$\varepsilon_{reff} = \frac{(\varepsilon_r+1)}{2} + \frac{(\varepsilon_r - 1)}{2}\left[1+12\frac{h}{W_c}\right]^{-\frac{1}{2}} \qquad (3-1)$$

where h is the substrate thickness and ε_r is its dielectric constant. W_c is the width of the conductor. It should be noted that in simulation, the actual configuration (figure 3.1 (a)) was used.

3.2 PATCH ANTENNA DESIGN

For an efficient radiator, a practical patch width W_p that leads to good radiation efficiencies can be calculated as [1]-[2]:

$$W_p = \frac{C}{2f_0\sqrt{\frac{(\varepsilon_r+1)}{2}}} \qquad (3-2)$$

where, C is the speed of light in free space and f_0 is the design frequency.

Additionally, for a microstrip patch antenna to radiate, modifications needs to be made to the transmission line. Referring to figure 3.2, where a rectangular patch of metal is atop the substrate, two properties are required;

i. The ground plane blocks the radiation in the $-z$ and steers it towards $+z$.
ii. In the far field, the fringing field around $y = 0$ adds up in phase with the fringing field around $y = L$. Therefore, maximum radiation is in the $+z$ direction.

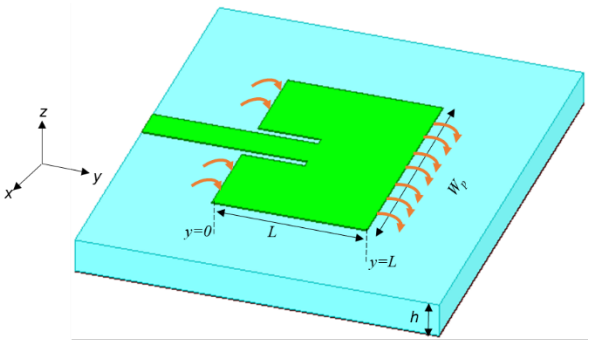

Figure 3.17: Patch antenna. Red arrows show the fringing fields.

The TM_{10} mode which is shown in figure 3.3 guarantees the above properties. The fringing field shown in figure 3.3 makes the electric length a little bit longer than the physical length as depicted in figure 3.4. The fringing length ΔL can be expressed as

$$\Delta L = 0.412h\frac{(\varepsilon_{reff}+0.3)(\frac{W_p}{h}+0.264)}{(\varepsilon_{reff}-0.258)(\frac{W_p}{h}+0.8)} \qquad (3-3)$$

It can be inferred from equation $(3-3)$ above that increasing ε_{reff} will increase the fringing length if W_p and h are kept constant. If $L = \frac{\lambda}{2\sqrt{\varepsilon_r}}$, resonance will occur and thus the patch will start to radiate. However, because of the fringing field, the effective electric length needs to be half the wavelength. Therefore, the required physical length to achieve resonance will be modified to

$$L = L_e - 2\Delta L = \frac{\lambda_m}{2} - 2\Delta L \qquad (3-4)$$

where L_e is the electrical length, $\lambda_m = \frac{\lambda}{\sqrt{\varepsilon_{reff}}}$ and the factor of "2" is from the fact that there are fringing effects around both $y = 0$ as well as $y = L$.

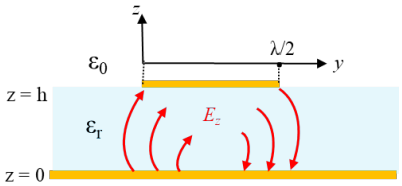

Figure 3.18: TM10 electric field distribution along the patch length

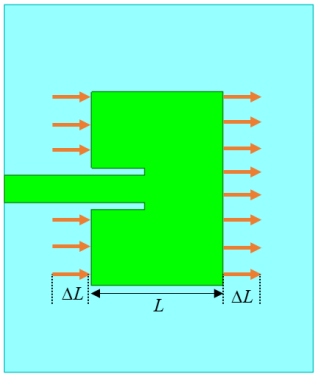

Figure 3.19: Patch antenna electrical length, L + 2ΔL.

Using the transmission line model, the patch is analyzed as two radiating slots that are separated by a low impedance transmission line of length approximately $\frac{\lambda_m}{2}$. As shown in figure 3.5, the radiating slots form a two-element array that is linearly polarized in the feed line direction *(in this case, the electric field polarization is on the y-direction)*. Therefore, it can be asserted that with reference to figure 3.5, patch antennas are linearly polarized. The yz plane is called the E-plane while the xz plane is called the H-plane.

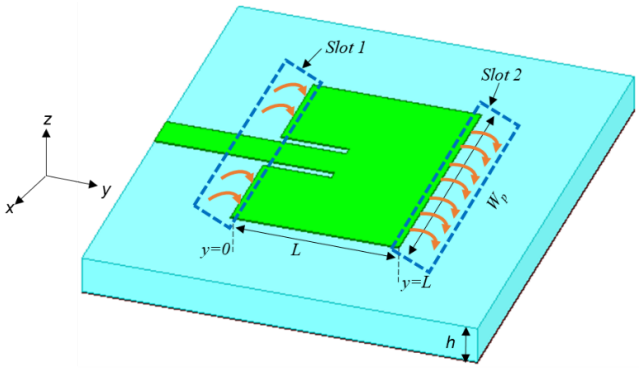

Figure 3.20: Patch antenna model with a two-slot array.

There are multiple techniques to feed patch antennas that include; edge, probe, and inset feed. The impedance of the patch antenna at the edge Z_e is large as can be inferred from equation $(3-5)$, and it is required to match it to a standard transmission line of 50 Ω.

$$Z_e = 90\frac{\varepsilon_r{}^2}{\varepsilon_r - 1}\left(\frac{L}{W_p}\right)^2 \qquad (3-5)$$

The inset-feed technic is used in this work and the inset length, L_i is approximated as:

$$L_i = \frac{\left(\cos^{-1}\sqrt{\frac{Z_0}{Z_e}}\right)L}{\pi} \qquad (3-6)$$

For better antenna performance, the ground plane and the substrate are required to be larger than the patch by at least six times the substrate thickness [3]. Otherwise, a small ground plane may cause stronger back-lobes.

It is needful to note that from a communication perspective the bandwidth of a patch antenna same as it is for resonant antennas such as dipoles, is small (they are inherently narrow-band antennas). The bandwidth BW of the patch is given by

$$BW = f_r\left(3.77\frac{\varepsilon_r - Wh}{\varepsilon_r^2 L\lambda}\right) \qquad (3-7)$$

where f_r, is the resonant frequency.

The performance of the microstrip patch antenna on a 32 μm SiC substrate was assessed using a full wave 3D simulator, ANSYS High Frequency Structure Simulator (HFSS) at 300 GHz. The optimized width W_p was 0.2132 mm, the length L was 0.147 mm, the feed line width (50 Ω) was 0.0306 mm, and the inset length and width were 0.059 mm and 0.0459mm respectively. The signal line and the ground metal were considered to be gold. The figures of merit were the return loss (S_{11}) and the radiation pattern. As shown in figure 3.6 (a), the patch antenna exhibits a narrow bandwidth where a —10 dB bandwidth at 300 GHz is about 11.72 GHz (4 %). Additionally, the half power beamwidth is 97 degrees in the xz (solid) and yz (dashed) planes as depicted in figure 3.6 (b).

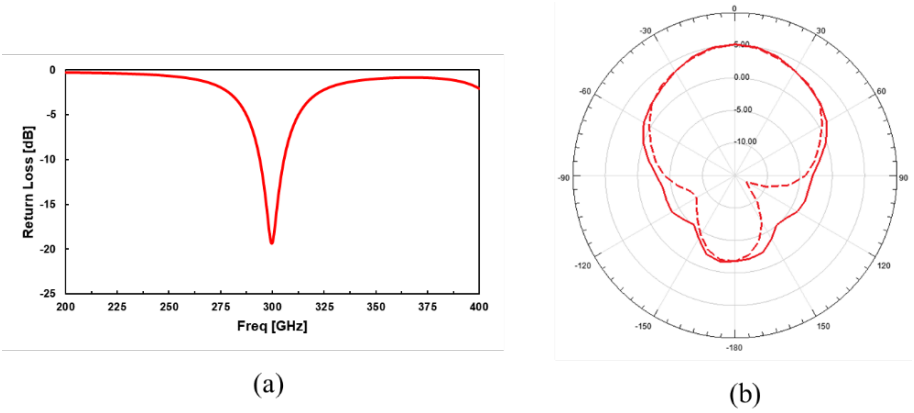

Figure 3.21: Patch antenna simulation results; (a) return loss, (b) radiation pattern.

3.3 COMBINER DESIGN

Power combiners and dividers are passive devices employed for either combining or dividing power. A power combiner merges two or more input signals at an output port, while a power divider splits an input signal into two (or more) output signals with reduced power. This work focuses on the application of power combiners. These devices can feature three ports, four ports, or more, and are typically designed to be lossless. Three-port networks take the form of T-junctions and other types of power combiners.

3.3.1 Three-Port Networks

A three-port network is a network with two inputs and one output. The scattering matrix of an arbitrary three-port network has the following nine independent elements;

$$[S] = \begin{bmatrix} S_{11} & S_{12} & S_{13} \\ S_{21} & S_{22} & S_{23} \\ S_{31} & S_{32} & S_{33} \end{bmatrix} \quad (3-8)$$

If the device is passive and has no anisotropic materials, then it must be reciprocal, and its scattering matrix will be symmetric ($S_{ij} = S_{ji}$). To avoid power loss, it is required to have a network that is lossless and matched at all ports. However, it is not possible to construct a three-port network that is lossless, reciprocal and matched at all ports. If all the network ports are matched, then $S_{ii} = 0$, and if the network is reciprocal, then the scattering matrix above becomes

$$[S] = \begin{bmatrix} 0 & S_{12} & S_{13} \\ S_{21} & 0 & S_{23} \\ S_{31} & S_{32} & 0 \end{bmatrix} \quad (3-9)$$

If the network is lossless, the energy conservation principles requires that the scattering matrix is unitary, which leads to the following:

$$|S_{12}|^2 + |S_{13}|^2 = 1, \quad (3-10a)$$

$$|S_{12}|^2 + |S_{23}|^2 = 1, \quad (3-10b)$$

$$|S_{13}|^2 + |S_{23}|^2 = 1, \quad (3-10c)$$

$$S_{13}^* S_{23} = 0, \quad (3-10d)$$

$$S_{23}^* S_{12} = 0, \quad (3-10e)$$

$$S_{12}^* S_{13} = 0, \quad (3-10f)$$

Equations $(3-10d)$ to $(3-10f)$ indicate that at least two of the parameters (S_{12}, S_{13}, S_{23}) must be zero. However, this requirement is contradictory to one of the equations $(3-10a)$ to $(3-10c)$, suggesting that a three-port network cannot simultaneously be lossless, reciprocal, and matched at all ports. Relaxing any of these conditions allows for the possibility of a physically realizable device.

3.3.2 T-junction combiner

The T-junction power combiner is a simple three-port network that can be used for power combining, and it is adaptable for use in practically any type of transmission line medium. As discussed in the preceding section, such junctions cannot be matched simultaneously at all ports. The lossless T-junction combiner can be modeled as a junction of three transmission lines, as shown in figure 3.7 [1]. In broad terms, the presence of fringing fields and higher-order modes at such a junction can result in the accumulation of stored energy, which can be quantified through the inclusion of a lumped susceptance, denoted as B, in the analysis. In order for the combiner to be matched to the output line of characteristic impedance Z_0, it is required that

$$Y_{in} = jB + \frac{1}{Z_1} + \frac{1}{Z_2} = \frac{1}{Z_0} \qquad (3-11)$$

If the transmission lines are assumed to be lossless, then the characteristic impedances are real. If it is also assumed that $B = 0$, then equation $(3-11)$ reduces to

$$\frac{1}{Z_1} + \frac{1}{Z_2} = \frac{1}{Z_0} \qquad (3-12)$$

In practical applications, when the value of B is not insignificant, methods such as employing discontinuity compensation or introducing a reactive tuning element are typically employed to mitigate this susceptance, particularly within a limited frequency band.

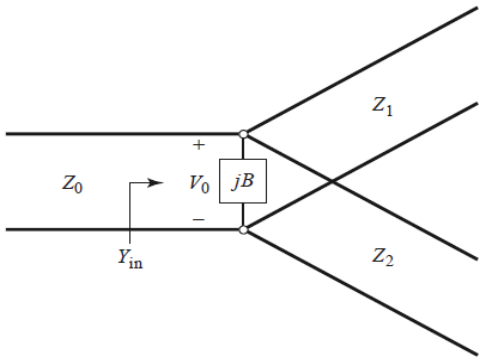

Figure 3.22: T-junction combiner/divider model.

The input line impedances, Z_1 and Z_2, can be selected to provide various power combining or splitting ratios. Thus, for 50 Ω output line, a 3 dB (equal combining) power combiner can be made by using two 100 Ω output line as given in the analysis below.

If the voltage V_0 at the junction is as shown in figure 3.7, the power at ports 0, 1 and 2 will respectively be

$$P_0 = \frac{1}{2}\frac{V_0^2}{Z_0}, \qquad (3-13a)$$

$$P_1 = \frac{1}{2}\frac{V_1^2}{Z_1} = \frac{1}{2}P_0, \qquad (3-13b)$$

$$P_2 = \frac{1}{2}\frac{V_2^2}{Z_2} = \frac{1}{2}P_0. \qquad (3-13c)$$

For $Z_0 = 50\ \Omega$, the characteristic impedances at ports 1 and 2 will be

$$Z_1 = 2Z_0 = 100\ \Omega \qquad (3-14a)$$

$$Z_2 = 2Z_0 = 100\ \Omega \qquad (3-14b)$$

If necessary as it is for our case, a quarter-wave transformer line of $\sqrt{2}Z_0 = 70.71\ \Omega$ can be used to bring the output line impedances back to 50 Ω as shown in figure 3.8. The corresponding line widths for 50 Ω and 70.71 Ω for a 32 μm SiC substrate ($\varepsilon_r = 10$) are 30.6 and 13.3 μm respectively. In case the input lines are matched, then the output line will be matched. There will be no isolation between the two input ports, and there will be a mismatch looking into the input ports.

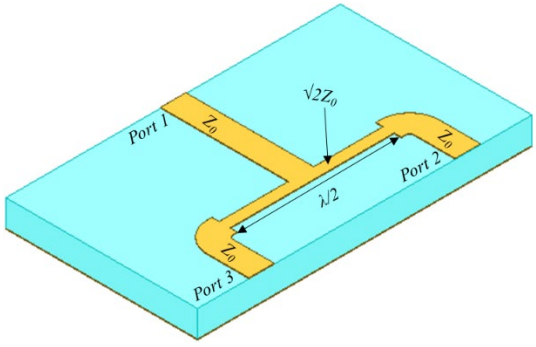

Figure 3.23: Microstrip line T-junction combiner/divider.

The performance of the microstrip 2×1 T-junction combiner at 300 GHz was assessed using a full wave 3D simulator ANSYS HFSS. The signal line and the ground metal were considered to be gold. The figures of merit were; return loss (S_{11}, S_{22}, S_{33}), insertion loss (S_{12}, S_{13}), and isolation (S_{23}). From the simulation results depicted in figure 3.9, $S_{11} = -22\ dB$, $S_{22/33} = -7\ dB$, which implies there is a mismatch looking into these ports. $S_{12/13} = -3.2\ dB$, whereas $S_{23} = -6\ dB$ implying poor isolation between the two ports. It is worth noting that arbitrary configurations can be formed from the 2×1 such as 4×1, 8×1, etc.

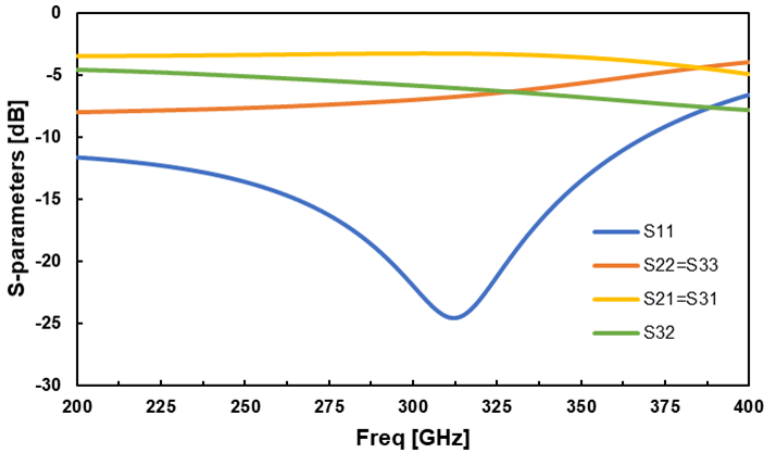

Figure 3.24: Simulated T-junction combiner S-parameters versus frequency

3.3.3 The Wilkinson Combiner

The lossless T-junction combiner is characterized by unmatched ports and lacks isolation between its output ports. Conversely, a lossy three-port network can be engineered to feature matched ports with isolation between output ports. The Wilkinson power combiner/divider [4] exemplifies such a network, showcasing the unique property of appearing lossless when its output ports are matched, implying that only the reflected power from these ports is dissipated. The Wilkinson power combiner can be configured to accommodate arbitrary power inputs/outputs, although our focus initially will be on the equal 2×1 case. Typically implemented in microstrip line, as illustrated in figure 3.10 (a), its corresponding transmission line circuit is provided in figure 3.10 (b). For a two-way Wilkinson combiner using a quarter-wave $(\frac{\lambda}{4})$ impedance transformer having a characteristic impedance of $\sqrt{2}Z_0$ and a lumped isolation resistor of $2Z_0$ with all three ports matched, high isolation between the output ports is obtained. Design for 50 Ω input and output

lines requires the isolation resistor to be $2Z_0 = 100\ \Omega$ and the impedance of the quarter-wave line to be $\sqrt{2}Z_0 = 70.71\ \Omega$.

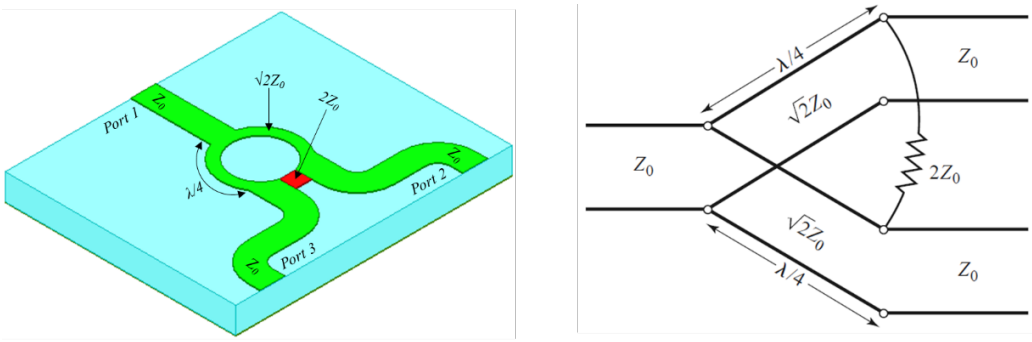

(a) (b)

Figure 3.25: The Wilkinson combiner/divider; (a) equal split MSL structure, (b) equivalent transmission line circuit.

3.3.3.1 Derivation of scattering parameters

The circuit shown in figure 3.10 (b) is analyzed by reducing it to two simpler circuits driven by symmetric and antisymmetric sources at the output ports using the "even-odd" mode analysis technique [1]. All impedances are normalized to the characteristic impedance Z_0, and the circuit of figure 3.10 (b) is redrawn with voltage generators at the output ports as shown in figure 3.11. The network is drawn in a form that is symmetric across the mid-plane; the two source resistors of normalized value 2 combine in parallel to give a resistor of normalized value 1, representing the impedance of a matched source. The quarter-wave lines have a normalized characteristic impedance Z, and the shunt resistor has a normalized value of r. For equal power combiner/divider, these values should be $Z = \sqrt{2}$ and $r = 2$.

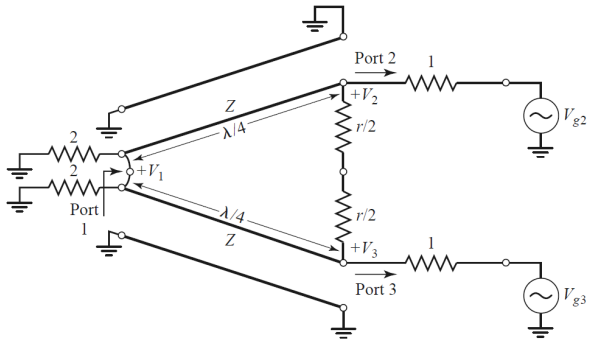

Figure 3.26: Normalized and symmetric form of the Wilkinson combiner/divider circuit [1].

Two separate modes of excitation for the circuit of figure 3.11 are defined; the *even mode*, where $V_{g2} = V_{g3} = 2V_0$, and the *odd mode*, where $V_{g2} = -V_{g3} = 2V_0$. The superposition of these two modes gives an excitation of $V_{g2} = V_{g2} = 4V_0$ and $V_{g3} = 0$, from which the scattering parameters of the network can be derived.

a) Even mode excitation

For even-mode excitation, $V_{g2} = V_{g3} = 2V_0$, so $V_2^e = V_3^e$ and hence no current flows through the $r/2$ resistors or the short circuit between the inputs of the two transmission lines at port 1. Therefore, the network in figure 3.11 can be bisected with open circuits at these points to get the network in Figure 3.12 (a) with the grounded side of the *λ*/4 line not shown. Since the transmission line is like a quarter-wave transformer, looking into port 2 the impedance will be

$$Z_{in}^e = \frac{Z^2}{2}. \qquad (3-15)$$

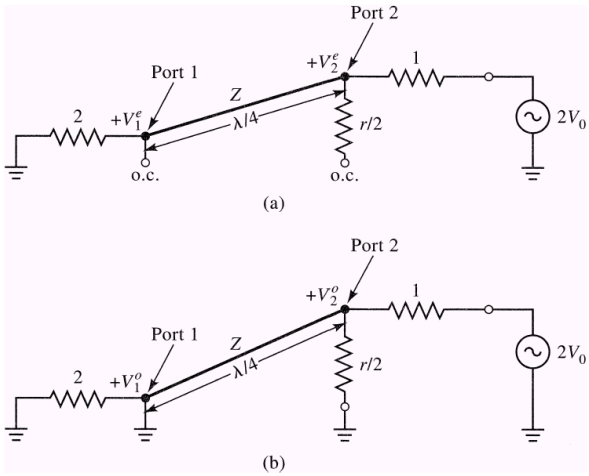

Figure 3.27: Wilkinson combiner circuit; (a) even mode excitation, (b) odd mode excitation.

Thus, if $Z = \sqrt{2}$, port 2 will be matched for even-mode excitation; then $V_2^e = V_0$ since $Z_{in}^e = 1$ and *r*/2 is superfluous since one end is open-circuited. V_1^e can be found from the transmission line equations. If $x = 0$, at port 1 and $x = -\lambda/4$ at port 2, the voltage on the transmission line section can be expressed as

$$V(x) = V^+\left(e^{-jBx} + \Gamma e^{jBx}\right). \qquad (3-16)$$

Hence

$$V_2^e = V(-\lambda/4) = jV^+(1-\Gamma) = V_0, \qquad (3-17a)$$

$$V_1^e = V(0) = V^+(1+\Gamma) = jV_0\frac{\Gamma+1}{\Gamma-1}. \qquad (3-17b)$$

The reflection coefficient Γ at port 1 looking towards the resistor of normalized value 2 is expressed as

$$\Gamma = \frac{2-\sqrt{2}}{2+\sqrt{2}}, \qquad (3-18)$$

then

$$V_1^e = -jV_0\sqrt{2}. \qquad (3-19)$$

b) Odd mode excitation

For odd-mode excitation, $V_{g2} = -V_{g3} = 2V_0$, so $V_2^o = V_3^o$, and there is a voltage null in the middle of the circuit in figure 11.3. The circuit can be bisected by grounding it at two points on its midplane to have the network in figure 3.12 (b). Looking into port 2, there is an impedance of $r/2$ since the length of the parallel-connected transmission line is $\lambda/4$ and shorted at port 1, and hence it is like an open circuit at port 2. If $r = 2$, port 2 will be matched for odd-mode excitation. Then $V_2^o = V_0$ and $V_1^o = 0$; for this excitation mode, all power is delivered to the $r/2$ resistors, and none to port 1. To find the input impedance at port 1 when ports 2 and 3 are terminated in matched loads, the circuit shown in figure 3.13 (a) is used, that is similar to an even mode of excitation since $V_2 = V_3$. The resistor of normalized value 2 can be eliminated since no current flows through it, resulting into the circuit in figure 3.13 (b). Hence, we have a parallel connection of two quarter-wave transformers terminated in loads of unity (normalized). The input impedance will then be

$$Z_{in} = \frac{1}{2}\left(\sqrt{2}\right)^2 = 1. \qquad (3-20)$$

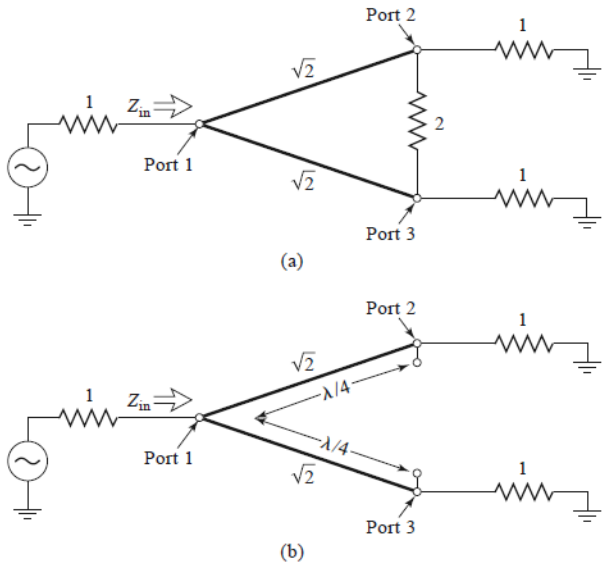

Figure 3.28: Wilkinson combiner analysis to get S11; (a) combiner terminated, (b) circuit (a) bisected.

The scattering parameters are thus:

$S_{11} = 0$ ($Z_{in} = 1$ at port 1)

$S_{22} = S_{33} = 0$ (ports 2 and 3 matched for even and odd modes)

$S_{12} = S_{21} = \frac{V_1^e + V_1^o}{V_2^e + V_2^o} = -j\sqrt{2}$ (symmetry due to reciprocity)

$S_{13} = S_{31} = -j\sqrt{2}$ (symmetry of ports 2 and 3)

$S_{23} = S_{32} = 0$ (due to short or open at bisection)

The S-matrix can therefore be written as:

$$[S] = \frac{1}{\sqrt{2}}\begin{bmatrix} 0 & j & j \\ j & 0 & 0 \\ j & 0 & 0 \end{bmatrix}. \qquad (3-21)$$

The performance of the microstrip 2×1 Wilkinson combiner at 300 GHz was also assessed using ANSYS HFSS. The figures of merit are; return loss (S_{11}, S_{22}, S_{33}), insertion loss (S_{12}, S_{13}), and isolation (S_{23}). From the simulation results shown in figure 3.14, the return loss, $S_{11/22/33} < -15\ dB$, which implies there is matching at all ports. $S_{12/13} = -3.4\ dB$, whereas $S_{23} < -15\ dB$ implying a good isolation between the two ports. It is worth noting that arbitrary number can be formed from the 2×1 to give configurations such as 4×1, 8×1, etc.

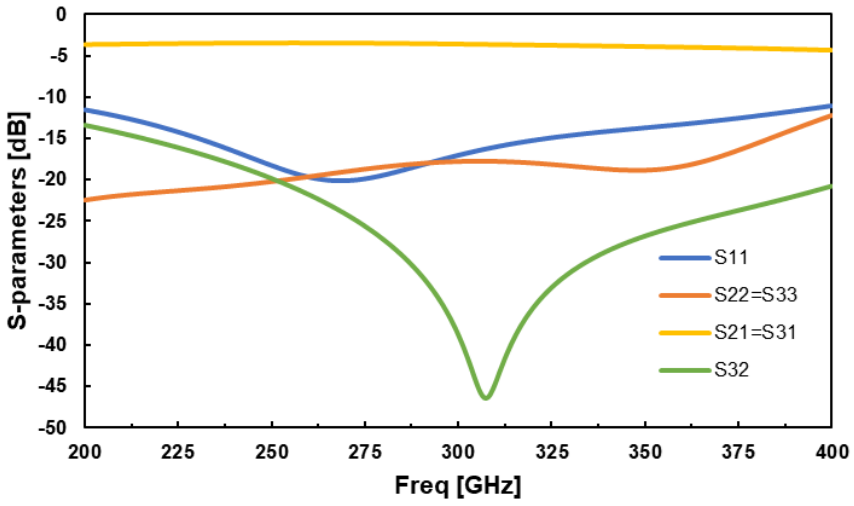

Figure 3.29: Simulated Wilkinson combiner S-parameters versus frequency.

3.3.4 Coupled Line Wilkinson Combiner

To reduce the size of the conventional Wilkinson combiner/divider discussed in the previous section, coupled lines can be used. A theoretical analysis on how the even and odd mode impedance (Z_{0e} and Z_{0o}) of the coupled lines affects the S-parameters when used as a divider is presented, which, due to the principle of reciprocity, is analogous to its application as a combiner. In a coupled-line Wilkinson divider, the input is primarily influenced by the even-mode impedance (Z_{0e}). Upon setting Z_{0e} to match the input port, the matching and isolation of the output ports become dependent on Z_{0o}. Decreasing Z_{0o} reduces the spacing between the coupled lines, leading to a more compact divider layout. However, there are tradeoffs to consider as Z_{0o} decreases. These design tradeoffs are thoroughly discussed in [5].

3.3.4.1 Theoretical analysis

Figure 3.15 (a) shows a Wilkinson power divider/combiner with coupled lines and figure 3.15 (b) shows the input port (port 1) analysis. Note that in this analysis, the divider application is considered and because of reciprocity, all is the same when used as a combiner.

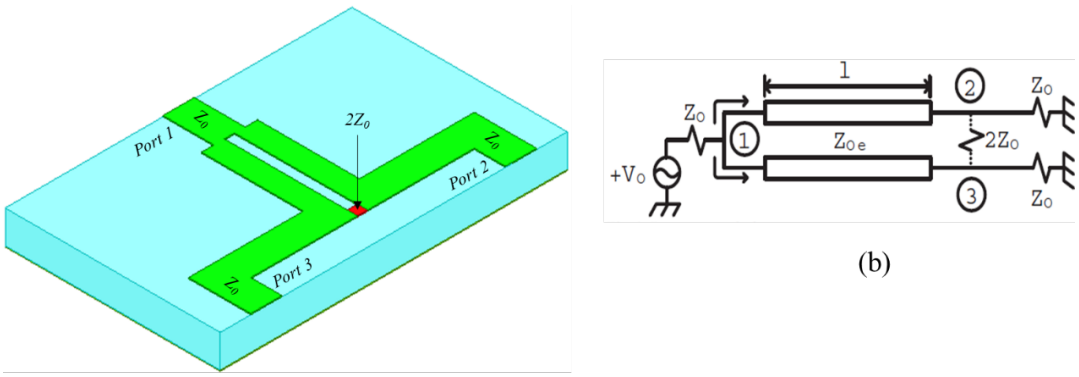

(a) (b)

Figure 3.30: Coupled line Wilkinson combiner/divider; (a) MSL structure, (b) port 1 analysis.

The input signal from port 1 is symmetrically split between the two output ports and the isolation resistor is not seen from Port 1. Thus, the normalized input impedance can be expressed as

$$\overline{Z}_{in1} = 0.5\overline{Z}_{0e}\frac{1 + j\overline{Z}_{0e}\tan\beta l}{\overline{Z}_{0e} + j\tan\beta l}. \qquad (3-22)$$

Since S_{11} is a function of the input impedance Z_{in1}, it is therefore a function of Z_{0e}. If we assume that the coupled lines are lossless, then the transmitted power is directly related to the returned power and the relation can be written as

$$|S_{21}|^2 = |S_{31}|^2 = 0.5(1 - |S_{11}|^2). \qquad (3-23)$$

From the analysis above, S_{11}, S_{21} and S_{31} are affected by Z_{0e} only. To ensure a perfect matching at the input port, Z_{0e} is fixed as $\sqrt{2}Z_0$,and hence the above three S-parameters are fixed.
The analysis of the output ports (Port 2 and 3) is shown in figure 3.16 [5].

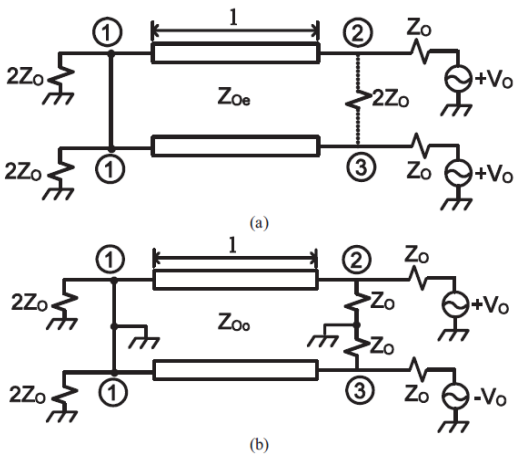

Figure 3.31: Output port analysis; (a) even mode analysis, (b) odd mode analysis.

Because the two output ports are symmetrical, only Port 2 is analyzed. The normalized input impedances as seen from Port 2 for the even and the odd mode are

$$\overline{Z}_{in2}^{e} = 0.5\overline{Z}_{0e}\frac{2 + j\overline{Z}_{0e}\tan\beta l}{\overline{Z}_{0e} + j2\tan\beta l}, \qquad (3-24a)$$

$$\overline{Z}_{in2}^{o} = 0.5\overline{Z}_{0e}\frac{1 + j\overline{Z}_{0e}\tan\beta l}{\overline{Z}_{0e} + j\tan\beta l}. \qquad (3-24b)$$

The reflection coefficients for both modes are expressed as

$$\Gamma_2^{e,o} = \frac{\overline{Z}_{in2}^{e,o} - 1}{\overline{Z}_{in2}^{e,o} + 1} \qquad (3-25)$$

and S_{22} is given as

$$S_{22} = \frac{1}{2}(\Gamma_2^e + \Gamma_2^o). \qquad (3-26)$$

Additionally, the isolation between Port 2 and Port 3 can be calculated as

$$|S_{32}|^2 = 1 - 2\left|\frac{\overline{Z}_{in2}^{o}}{\overline{Z}_{in2}^{o} + 1}\right|^2 - |S_{22}|^2 - |S_{21}|^2. \qquad (3-27)$$

where the second item on the right side is the power loss in the isolation resistor of $\sqrt{2}Z_0$.

From the analysis above, it can be deduced that generally, S_{22} and S_{32} are affected by both the even and odd mode impedance of the coupled lines. However, note that at the center frequency, when $\beta l = \pi/2$, the reflection coefficient becomes zero, and therefore S_{22} and S_{32} are determined by Z_{0e} only and this implies that once, Z_{0e} is fixed as $\sqrt{2}Z_0$, the divider's center frequency is also fixed. By adjusting the widths and spacings of the coupled lines, it is possible to achieve different characteristic impedances Z_{0e} and Z_{0o}. When the spacing is fixed, a desired Z_{0e} can be achieved by varying the values of Z_{0o}. However, changes in frequency can affect the matching and isolation of the output ports, which are influenced by Z_{0o}.

A synthesis method using Akhtarzad's technique of coupled lines design [6-7] is adopted for the coupled line Wilkinson combiner used in this work. Since our input/output characteristic impedance is 50 Ω, and the even mode characteristic impedance Z_{0e} is fixed as $\sqrt{2}Z_0 \approx 70.71\ \Omega$. The odd mode characteristic impedance $Z_{0o} = 35\ \Omega$ from the approximation that

$$Z_0 \approx \sqrt{Z_{0e}Z_{0o}}. \qquad (3-28)$$

The approximation in equation $(3-28)$ holds for applications where coupling between the lines needs to be as low as possible ($> -10\ dB$) which is our case.

With, the Akhtarzad's technique, "single" microstrip even and odd mode characteristic impedances are calculated first, as

$$Z_{0se} = \frac{Z_{0e}}{2} \approx 35\ \Omega \qquad (3-29)$$

and

$$Z_{0so} = \frac{Z_{0o}}{2} \approx 18\ \Omega \qquad (3-30)$$

The corresponding microstrip line widths for 35 Ω and 18 Ω on a SiC substrate ($\varepsilon_r = 10$) are 0.06 mm and 0.154 mm respectively. Hence for a 32 μm substrate with $h = 32\ \mu m$, the approximate values for single microstrip even and odd mode width to height ratio are respectively equal to

$$(W/h)_{se} = 2, \qquad (3-31a)$$

$$(W/h)_{so} = 5. \qquad (3-31b)$$

Using the graph in figure 3.17, we first select the broken (even-mode) curve, with $(W/h)_{se} = 2$ and then, select the solid (odd-mode) curve, which has parameter $(W/h)_{so} = 5$. The intersection of these two curves represents the design point, and its coordinates indicate the results:

$$W/h = 0.85, \qquad (3-32a)$$

$$S/h = 0.25. \qquad (3-32b)$$

where W is the width of each of the coupled lines, S is their spacing and h is the substrate height. Since h is fixed as 0.032 mm, then $W \approx 0.0225\ mm$ and $S \approx 0.01\ mm$.

The length of the coupled lines L_c can be approximated as

$$L_c = \frac{(\lambda_{ge} + \lambda_{go})}{8} \qquad (3-33)$$

where λ_{ge} and λ_{go} are the even and odd mode wavelength and can be approximated as

$$\lambda_{ge} \approx \left(\frac{300}{f}\right)\left(\frac{Z_{0e}}{Z_{1e}}\right)\ mm, \qquad (3-34a)$$

$$\lambda_{go} \approx \left(\frac{300}{f}\right)\left(\frac{Z_{0o}}{Z_{1o}}\right)\ mm, \qquad (3-34b)$$

where f is the frequency (300 GHz) and Z_{1e} and Z_{1o} are the free space even mode and odd mode characteristic impedances and can be obtained from Bryant and Weiss' curves shown in figure 3.18 applicable to $\varepsilon_r = 1$ as 185 Ω and 75 Ω respectively. Hence, $\lambda_{ge} \approx 0.38\ mm$, $\lambda_{go} \approx 0.48\ mm$, and $L_c \approx 0.1\ mm$.

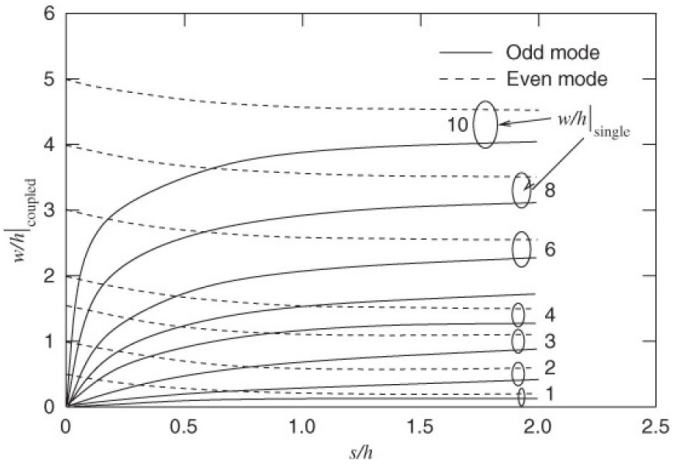

Figure 3.32: Akhtarzad's curves to determine W/h and S/h [6,7].

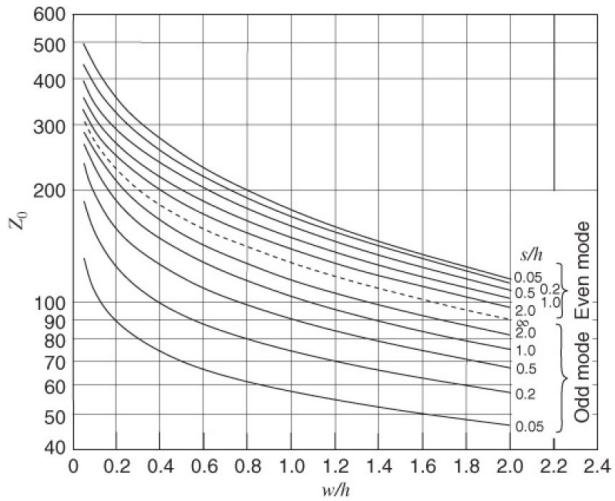

Figure 3.33: Bryant and Weiss' curves to determine the free space even mode and odd mode characteristic impedances [6,8].

It is important to note that the above analysis gives approximate results, and a synthesis procedure is required with a full-wave simulator to optimize the design. ANSYS HFSS software was used to optimize the combiner used in this work. The figures of merit were; return loss (S_{11}, S_{22}, S_{33}), insertion loss (S_{12}, S_{13}), and isolation (S_{23}). From the simulation results shown in figure 3.19, the return loss, $S_{11/22/33} < -20\ dB$, which implies there is matching at all ports. $S_{12/13} = -3.3\ dB$, whereas $S_{23} < -20\ dB$ implying good isolation between the two ports. It is worth noting that arbitrary configurations can be formed from the 2×1 such as 4×1, 8×1, etc.

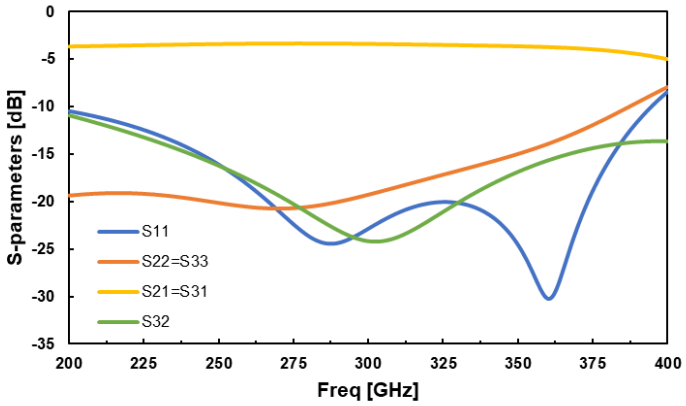

Figure 3.34: Simulated Coupled line Wilkinson combiner S-parameters versus frequency.

3.3.5 Antenna-Combiner integrated design

Figure 3.20 depicts the simulation results for the radiated power of the 2×1 integrated devices (shown in the respective inset pictures) as a function of the angle theta (θ) using Ansys HFSS with signal sources modelled as current sources referring to a UTC-PD. Table 3.1 summarizes the maximum radiated power for each device at 300 GHz. It can be deduced from the results that when the number of sources is multiplied by a factor of N, the radiated power will be enhanced by N^2.

Table 3.3: Maximum radiated power for integrated devices at 300 GHz.

Antenna Integrated device	**I_1 (mA)**	**I_2 (mA)**	**Radiated Power (dBm)**
2 × 1 T-junction combiner	1	1	-6.1
	1	0.5	-8.6
	1	0	-12
2 × 1 Conventional Wilkinson	1	1	-7.2
	1	0.5	-9.7
	1	0	-13
2 × 1 Coupled line Wilkinson	1	1	-6.4
	1	0.5	-8.9
	1	0	-12.2

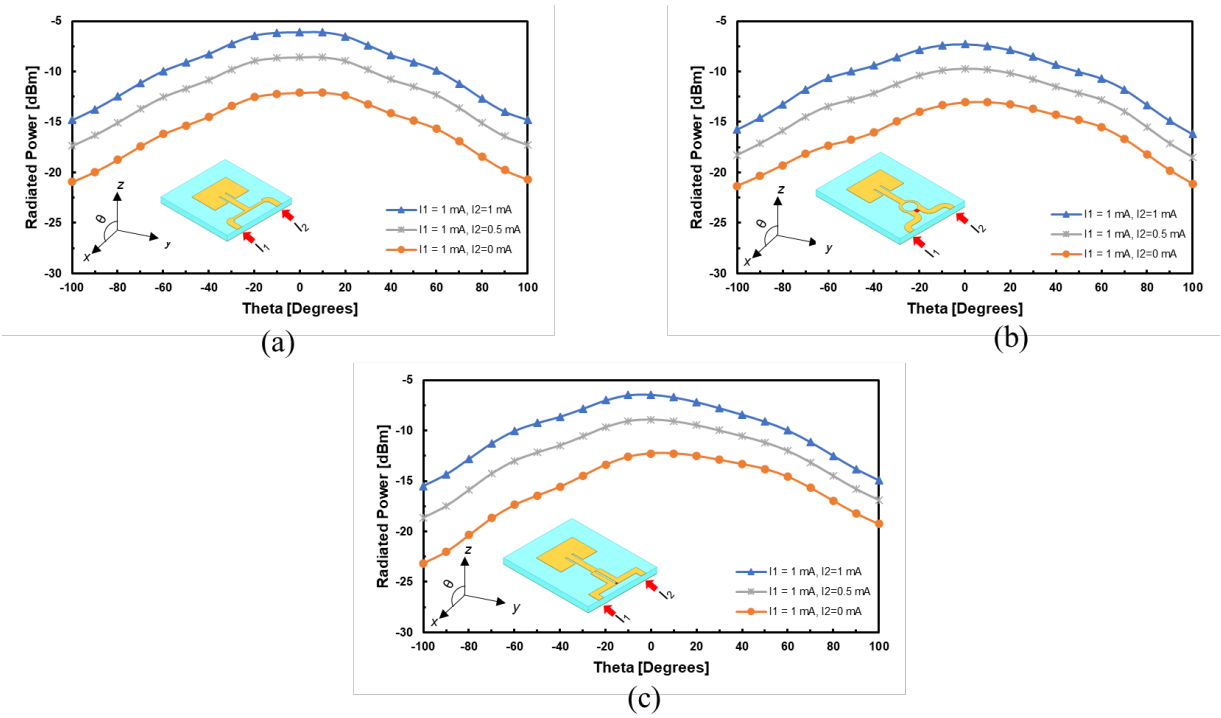

Figure 3.35: Antenna-combiner integrated device radiated power: (a) T-junction, (b) conventional Wilkinson, (c) coupled line Wilkinson.

3.3.6 Low Pass Filter Design

A five-section stepped-impedance low pass filter (LPF) having a high impedance of 110 Ω and a low impedance 25 Ω, and a radial stub having a 92 Ω impedance line were used as RF chokes in the UTC-PD bias circuits to prevent RF signal leakage into the DC bias lines. The simulated filter frequency response, shown in figure 3.21, showed that the stepped-impedance LPF has an attenuation that is over 10 dB, whereas the radial stub has approximately 7.5 dB attenuation at 300 GHz. Additionally, the radial stub could also help to compensate for the photdiode junction capacitance.

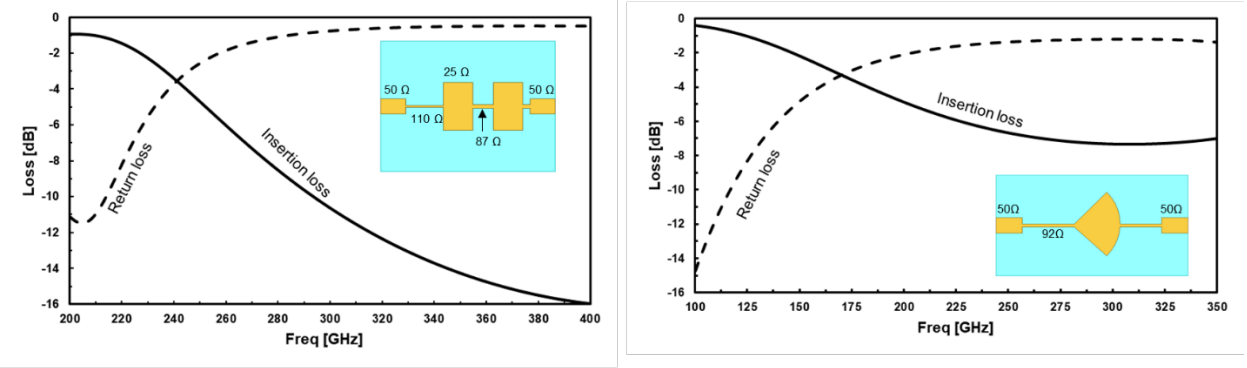

(a) (b)

Figure 3.36: . Low pass filter frequency response: (a) Stepped impedance; (b) Radial Stub

3.3.7 Radiation Efficiency

Furthermore, for microstrip design, losses (conductor loss and dielectric loss) need to be taken into account as they affect the radiation efficiency of the antenna. Simulation results suggest that the T-junction integrated device radiated more power than the two Wilkinson combiner integrated devices as this is due to its better radiation efficiency as illustrated in figure 3.22.

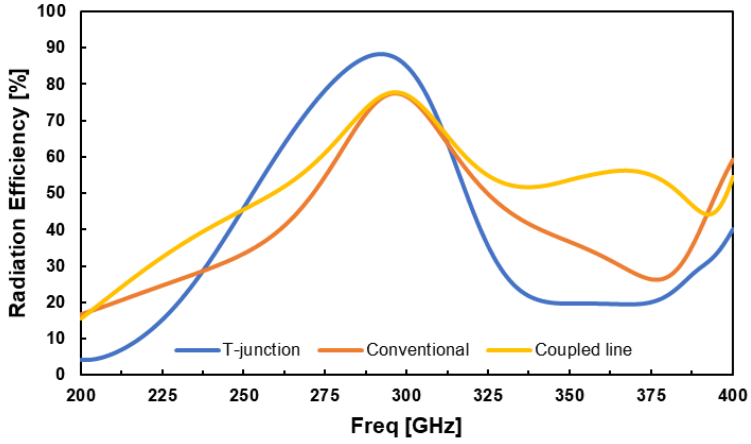

Figure 3.37: Integrated device radiation efficiency

3.3.8 Higher order modes

To prevent the excitation of higher-order modes in a microstrip, it is required to maintain the operating frequency below the cutoff frequency corresponding to the first higher-order mode. The cutoff frequency f_c for a microstrip line is defined by the expression provided in [9] as

$$f_c = \frac{c}{\sqrt{\varepsilon_r}(2W + 0.8h)}, \qquad (3-35)$$

where c is the speed of light in free space, ε_r is the substrate dielectric constant, W is the line width and h is the substrate thickness.

For the widest line (50 Ω), the cutoff frequency of the first higher-order mode appears above 1 THz for the 32 µm SiC substrate. This is far beyond the highest design frequency of 300 GHz. Figure 3.23 shows the cutoff frequency of the first higher-order mode for the microstrip widths of 0.0306 mm, 0.0225 mm, and 0.0133 mm.

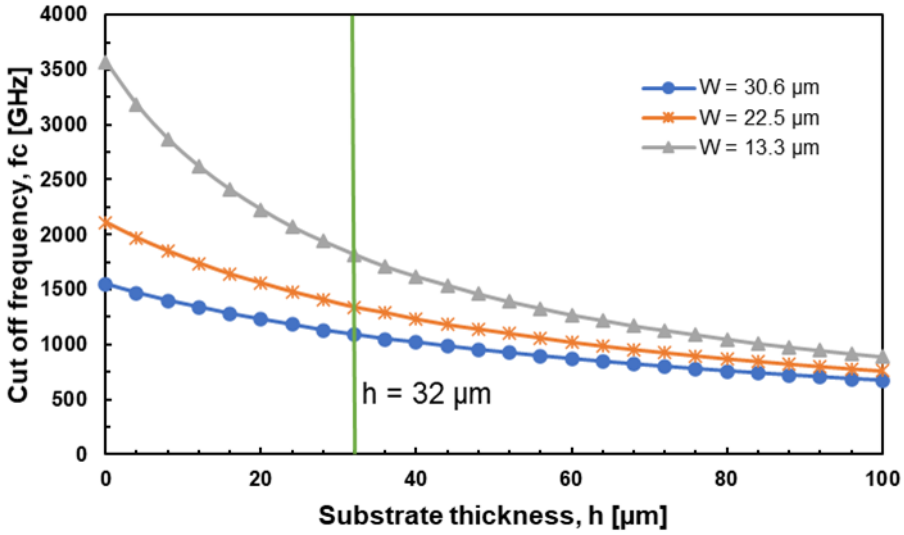

Figure 3.38: Cut-off frequency versus substrate thickness for different MSL widths

3.4 Conclusion

This chapter has focused on the theoretical framework pertaining to the design of the devices used in this research. The theory of microstrip line technology, patch antenna design, as well as the design of the T-junction combiner, the conventional Wilkinson combiner, and the coupled line Wilkinson combiner has been presented. Simulation results using Ansys HFSS for the optimized designs of all passive components prior to fabrication have been presented in this chapter. The figures of merit for combiner simulation include return loss, insertion loss and port isolation whereas radiated power is considered for antenna-combiner integrated design simulation to analyze the theoretical assertion that incase of current sources, increasing the number of sources

by N factor results in radiated power enhancement by N^2. Moreover, it has been shown that the novel coupled line Wilkinson combiner proposed in this work has a comparable performance with the conventional Wilkinson combiner while whilst it is easier to fabricate than the conventional Wilkinson combiner and it's λ/4 lines cover a half area of 0.1 × 0.055 mm2 compared to the conventional Wilkinson combiner. Thus, the coupled line Wilkinson combiner can be a better choice for monolithic integration of components at THz frequencies.

Additionally, design considerations including radiation efficiency and higher order modes have also been discussed. Simulation results have shown that the T-junction combiner integrated device exhibits better radiation efficiency than the Wilkinson combiner integrated device and hence radiates more power. Moreover, the first higher-order mode appears above 1 THz for all the microstrip widths used in this work.

REFERENCES

[1] D.M. Pozar, Microwave Engineering, Fourth Edition, John Wiley & Sons: Hoboken, 2012.

[2] C. A. Balanis, Antenna Theory: Analysis and Design, New York: J. Wiley & Sons, 2005.

[3] T. A. Milligan, Modern Antenna Design, 2nd edition, New Jersey: J. Wiley & Sons, 2005

[4] E.J. Wilkinson, "An N-way Power Divider", IRE Trans. on Microwave Theory and Techniques, vol. 8, p. 116-118, Jan. 1960.

[5] X. Tang and K. Mouthaan, "Analysis and design of compact two-way Wilkinson power dividers using coupled lines," 2009 Asia Pacific Microwave Conference, Singapore, December 2009.

[6] T. C. Edwards and M. B. Steer, Foundations for Microstrip Circuit Design, 4th Edition, West Sussex: J. Wiley & Sons, 2016.

[7] S. Akhtarzad, T. Rowbotham, and P. Johns, "The design of coupled microstrip lines," IEEE Trans. on Microwave Theory and Techniques, vol. 23, no. 6, pp. 486–492, Jun. 1975.

[8] T. Bryant and J. Weiss, "Parameters of microstrip transmission lines and of coupled pairs of microstrip lines," IEEE Trans. on Microwave Theory and Techniques, vol. 16, no. 12, pp. 1021–1027, Dec. 1968.

[9] H. -J. Song, M. J. Lancaster, Microstrip Filters for RF/Microwave Applications, John Wiley & Sons, Inc., 2001.

CHAPTER 4

BOW-TIE ANTENNA INTEGRATED DEVICE

In this chapter a detailed account of the fabrication process and characterization of a UTC-PD integrated with a bow-tie antenna on Silicon Carbide (SiC) substrate to generate THz waves is given. The characterization entails assessing the device frequency response, the effect of the fabricated device area by considering the mesa diameter as well as the length between the two *arms* of the bow-tie antenna.

4.1 UTC-PD FABRICATION

Recent studies have demonstrated the efficacy of epitaxial layer transfer of III-V materials onto SiC substrates for mitigating temperature increase of semiconductor devices [1–3]. SiC has a thermal conductivity of 490 W/m/K whereas InP has 68 W/m/K. This implies that SiC devices can be operated at higher photocurrents to have more output power.
If we consider that

$$P_{out} \propto I_{pp}^2 \times R_L = I_{pp} \times V_{pp} \qquad (4-1)$$

and

$$P_{diss} \propto I_{pp} \times (0.75 + V_{bias}) \qquad (4-2)$$

This suggests that the output power P_{out} is proportional to the square of the peak current I_{pp} and load resistance R_L. Moreover, power dissipation P_{diss} is proportional to the peak current and the bias voltage.

The temperature rise (ΔT) in a semiconductor substrate due to power dissipation can be estimated as

$$\Delta T = \frac{P_{diss} d}{kA} \qquad (4-3)$$

where d is the thickness of the substrate, A is the area through which heat is conducting, and k is the thermal conductivity. This implies that for the same power dissipation, the temperature will

rise at a rate that is seven times higher in InP devices than in SiC devices. Additionally, SiC exhibits low-loss characteristics at extremely high frequencies [4], possesses a Young's modulus more than three times greater than that of silicon [5], and boasts a larger dielectric constant compared to quartz. Therefore, we posit that the SiC substrate represents a promising platform for the fabrication of THz-wave devices using transferred epitaxial layers. Nonetheless, it is needful to note that in terms of power transmission and radiation efficiency, although SiC has been reported to have a low loss tangent of about 10^{-3} at 100 – 600 GHz [4], its high dielectric constant presents the challenge of increased surface-wave power and consequently leading to decreased efficiency.

In this work, the InP/InGaAs UTC-PD epi-layers were initially grown on a (100)-oriented semi-insulating (SI) InP substrate by metal organic chemical vapor deposition (MOCVD) at low-pressure. Table 4.1 shows the layer structure of the fabricated UTC-PD. A composite structure incorporating field control layers was employed to reduce electron transit time within the device [6].

Table 4.4: Layer structure of the fabricated UTC-PD.

Material	**Thickness**	**Eg (eV)**
p^+-InGaAs (p-contact)	32	
p^+-InGaAlAs (diff. barrier)	30	0.9
p-InGaAs graded	60	
i-InGaAs (depleted)	60	
p-InGaAs (first field contact)	10	
i-InGaAs spacer	5	
i- InGaAlAs (spacer)	10	0.9
i- InGaAlAs (spacer)	15	1.05
i-InP spacer	5	
n-InP field control	7	
i-InP collector	100	
n^+-InP collector buffer	20	
n^+- InGaAlAs etch stop	20	0.9
n^+-InP n contact	600	

The hetero-interface was step-graded in composition to eliminate potential barriers in the conduction band, while a portion of the absorption layer was graded in doping to introduce a built-in field. Additionally, an n-type InGaAlAs etch-stop layer (20 nm) was included to streamline the fabrication process.

The UTC-PD epitaxial wafer, with an InP substrate, was then fixed onto a glass supporting substrate and the InP substrate was removed completely by mechano-chemical polishing and chemical etching on the InP/InGaAs interface. Thereafter, an amorphous Si layer that was 10 nm thick was deposited onto the surface. The substrate was then wafer-bonded to the SiC substrate which was then thinned to 32 µm. This whole process was conducted at room temperature and high pressure of about 20 MPa to avoid any potential device characteristics deterioration [7]. Lastly, the glass substrate was ultimately detached from the UTC-PD epi-layers, leaving only the UTC-PD epi-layers on the SiC substrate, having the same order as they had been grown on InP substrate as illustrated in figure 4.1.

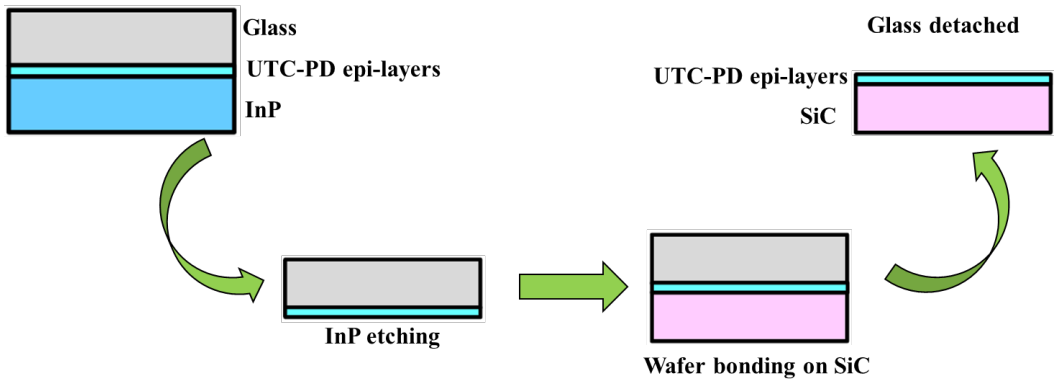

Figure 4.39: Epi-layer layer transfer from InP to SiC substrate.

Figure 4.2 illustrates the fabrication process after UTC-PD epi layer transfer on SiC substrate.

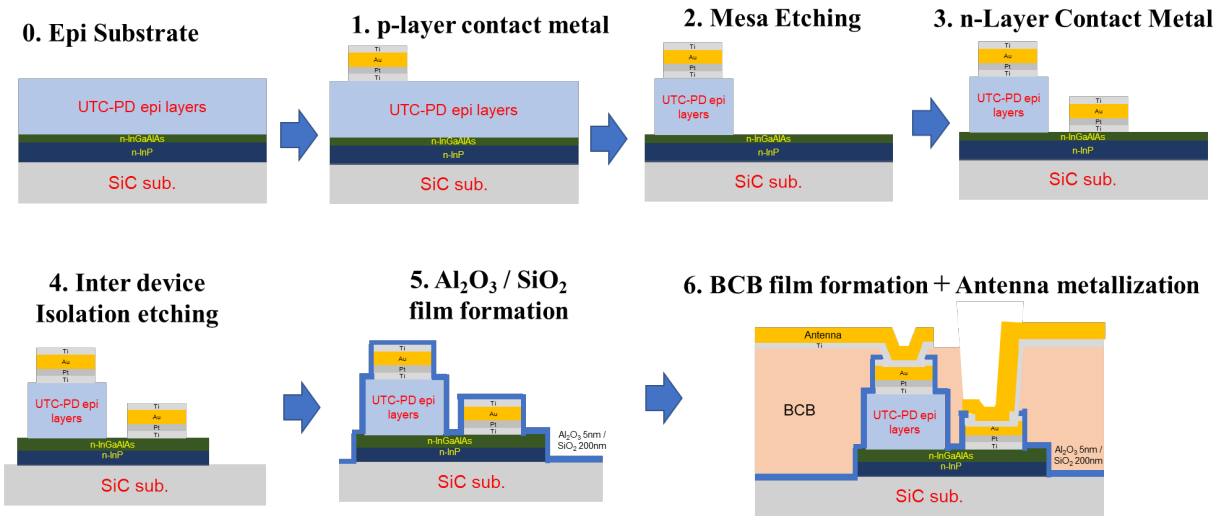

Figure 4.40: UTC-PD fabrication process

At first, the wafer surface was cleaned using conc NH_4OH and de-ionized H_20. This was followed by two-layer photoresist spin-coating using LOR3A and PFI89B4 and photolithography with an i-line stepper mask. The p- and n- device ohmic electrodes were formed using the electron beam vacuum evaporation equipment followed by the lift-off process using Acetone and hot N-methyl pyrrolidone (NMP). The electrodes were made of 250 nm gold (Au) and for optimal contact between the metal and the InGaAs layer, a 15 nm titanium (Ti) layer was deposited. However, since Ti is used as an adhesion layer while gold is a metal, Ti tends to diffuse into Au. To avoid this, we used a 15 nm Platinum (Pt) as a diffusion barrier between Ti and Au. Before the n electrode was formed, mesa etching was done and it involved lithography, photoresist hydrophilizing by O_2 ashing and wet etching. After the n electrode formation, inter-device isolation was done using the same process as mesa etching.

To reduce current leakage and improve performance, 5 nm Al_2O_3 and 200 nm SiO_2 films were deposited by Atomic Layer Deposition (ALD) and Plasma Chemical Vapor Deposition (CVD) respectively. This was followed by a 2 μm BCB (Cyclotene 6505) film formation to have a flat and smooth surface and the process was finalized with antenna metallization by electron beam vacuum evaporation equipment followed by the lift-off process.

4.2 BOW-TIE ANTENNA INTEGRATION

To ensure effective emission of electromagnetic waves from a photodiode (PD) while preserving the essential signal characteristics, it is imperative to meticulously choose the integrated antenna configuration. This selection process must account for several key factors, including the radiation pattern, polarization of the emitted signals, ease of fabrication, and the ability to introduce optical signals to the PD's active region.

Furthermore, to effectively exploit the notably broad bandwidth of photonics devices, a broadband antenna can be used, as it allows for the coverage of the full bandwidth with a single device. Among various antenna options, the self-complementary bow-tie antenna [8] shown in figure 4.3 stands out for its superior bandwidth characteristics, maintaining a constant input impedance regardless of the source frequency [9]. Consequently, it exhibits a fundamentally broad bandwidth, with the frequency dependence of the output power being dictated by the characteristics of the photodiode (PD). The configuration of the self-complementary antenna is inherently simple and well-suited for the fabrication process, while its polarization can be effectively controlled through the utilization of an axially symmetric antenna pattern. The UTC-PD was monolithically integrated with a bow-tie planar antenna designed for 300 GHz (500 µm half-wavelength). The distance L and diameter D of the UTC-PD mesa are important for the device operation, and they are discussed in section 4.4.

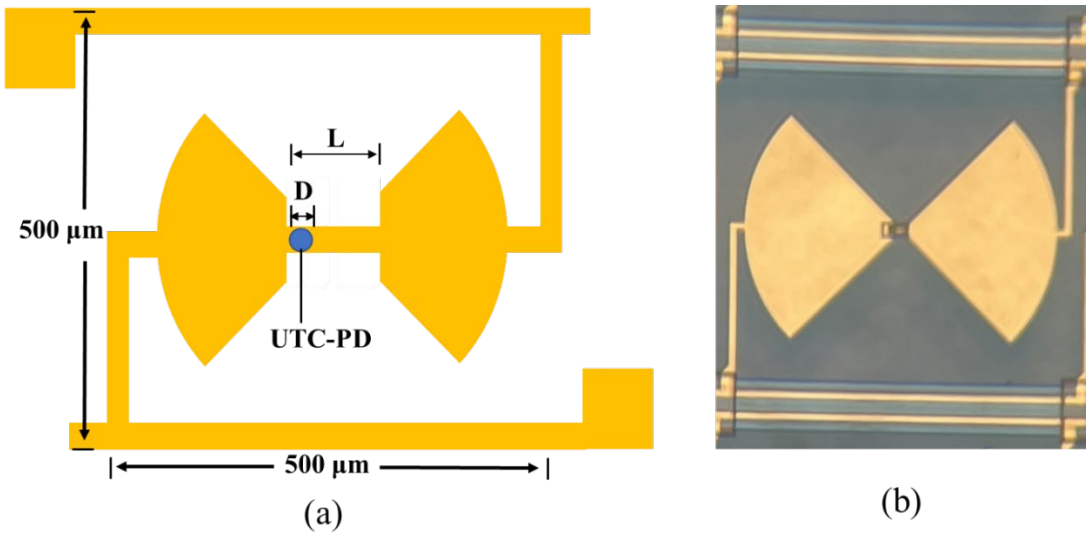

Figure 4.41: (a) Schematic of the device, (b) Fabricated device.

Back illumination is used in this work since the diode junction dimensions need to be small (typically a few μm in size) to reduce capacitance. Although evanescent coupling by using a vertical structure having a photodiode (PD) with an optical waveguide coupling provides better optical coupling and responsivity [10], the PD length (and capacitance) tends to be large to have sufficient effect. Hence, the difference between the back illumination and the evanescent coupling methods is smaller if the diode dimensions are reduced.

4.3 EXPERIMENTAL SETUP

The experimental setup to characterize the device is shown in figure 4.4. A pair of wavelength tunable laser diodes, LD1 and LD2, emitted two lightwaves with a power of 10 dBm and frequencies of 193.1 and 193.4 THz, respectively. The lightwaves were combined by an optical coupler (OC), modulated at 1 MHz by an intensity modulator (IM), and then amplified by an Erbium doped fiber amplifier (EDFA). An attenuator was used to control the optical power irradiated on the UTC-PD. A lens was used to couple the optical signal to the UTC-PD chip. A 300 GHz alternating current (AC) was generated by the UTC-PD. The radiated THz wave from the upward direction was detected using a Fermi-level managed barrier diode (FMBD) [11,12,13] equipped with a 25-mm aperture THz lens at 50 mm atop the device. The relative intensity of the 1 MHz component of the detected THz wave was measured using a lock-in amplifier (LIA). It should be noted that although more THz intensity is radiated from the bottom side of the chip, the upward THz wave intensity is measured in this work due to setup constraints.

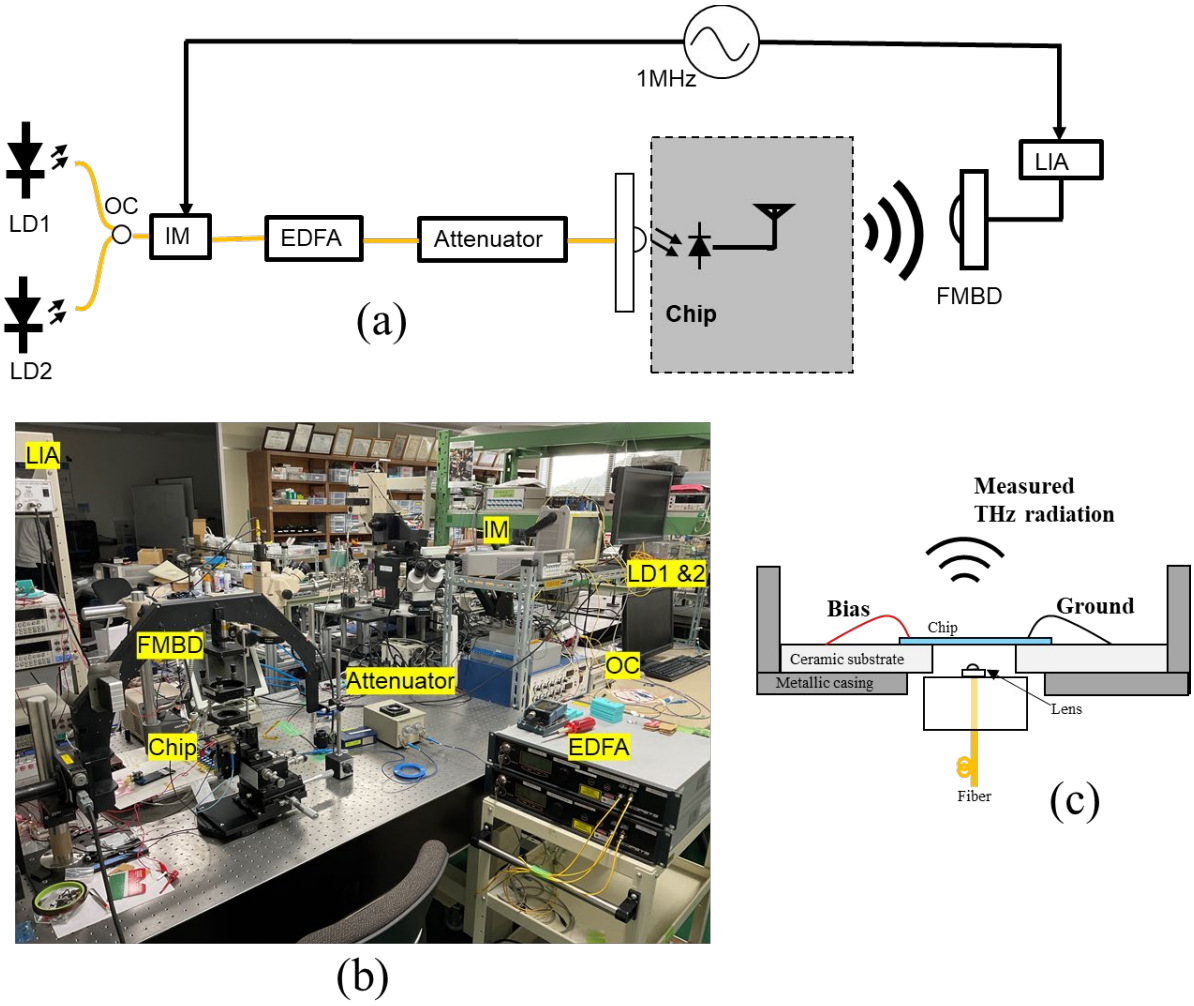

Figure 42.4: Experimental setup; (a) Schematic illustration, (b) photo of the setup, (c) chip irradiation configuration.

4.4 MEASUREMENT RESULTS

Initially the device frequency response in the J-band (220 GHz – 350 GHz) was measured for D = 7 μm and 8 μm, at a bias voltage of -1 V and 5 mA photocurrent when the length L = 20 μm. As depicted in figure 4.5, the device exhibited multiple peaks at 225 GHz, 295 GHz, and 340 GHz. These peaks are a function of the antenna impedance a well as the UTC-PD impedance and they occur at frequencies when the antenna impedance is a conjugate of the UTC-PD impedance. This concept will be further discussed in Chapter 5. Additionally, the D = 7 μm device gave a higher intensity than the D = 8 μm device and this was due to the smaller capacitance with the smaller device that leads to a better frequency response as explained in the next paragraphs.

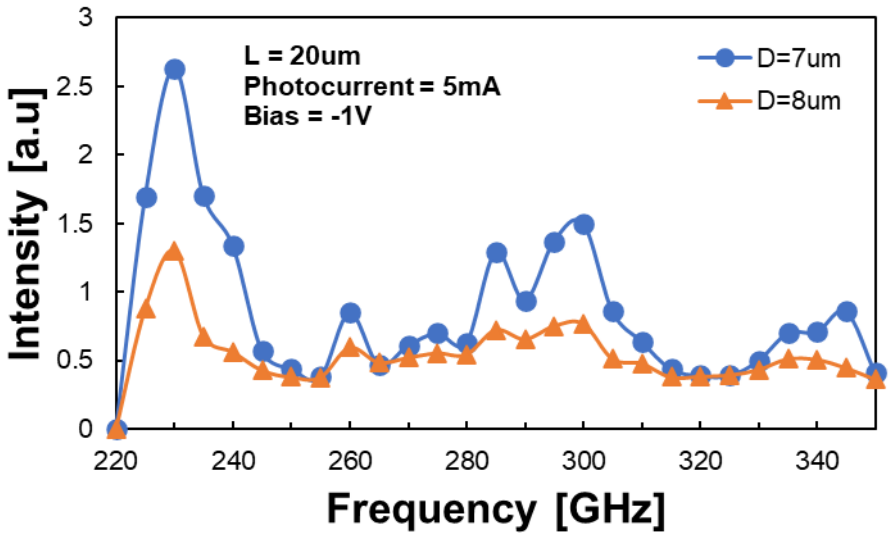

Figure 4.43: Measured bow-tie antenna integrated device frequency response (THz wave intensity versus frequency).

Considering a circular mesa structure, as the mesa diameter D increases, the area of the light absorption layer increases, allowing for more light to be absorbed, but the intensity of the terahertz waves decreases due to degradation of the response characteristics. Figure 4.6 shows the measurement results at 225 GHz and 295 GHz with mesa diameters of 6, 7 and 8 μm for L = 20 μm. From these results, it can be seen that the larger D resulted in a higher photocurrent especially at low voltages. Furthermore, it can be observed that as the bias voltage increases, the difference in the generated photocurrent decreases. This could be due to the fact that around these voltages (> 1 V), the device is starting to saturate due to space charge since the electron velocity is no longer increasing with increased electric field.

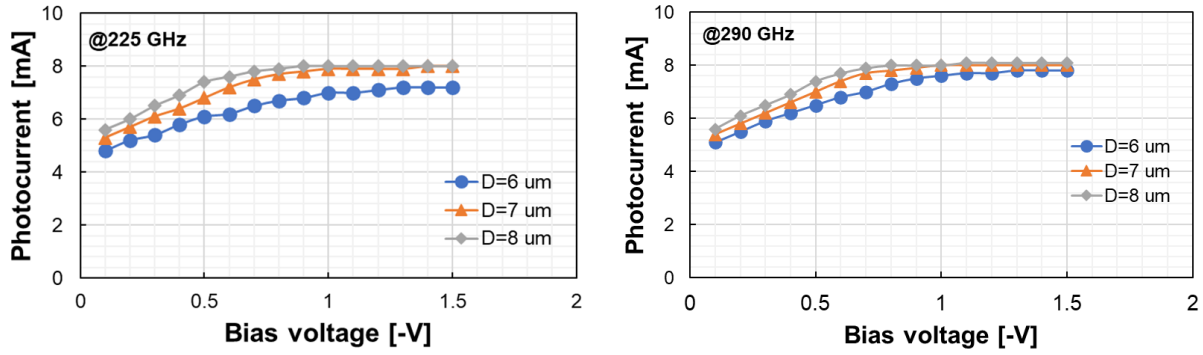

Figure 4.44: Measured photocurrent against negative bias voltage for different device mesa diameters at 225 GHz and 290 GHz.

Moreover, the performance of a UTC-PD may deteriorate due to the time constant formed by the load resistance and the capacitance of the UTC-PD. This is normally referred to as the RC (Resistance-Capacitance) time constant. The UTC-PD 3dB bandwidth (f_{3dB}) is a function of this time constant and the capacitance component is a function of the absorption layer area which is determined by the mesa size. As illustrated in figure 4.7, when the absorption layer area increases, the capacitance increases leading to a deteriorated THz output.

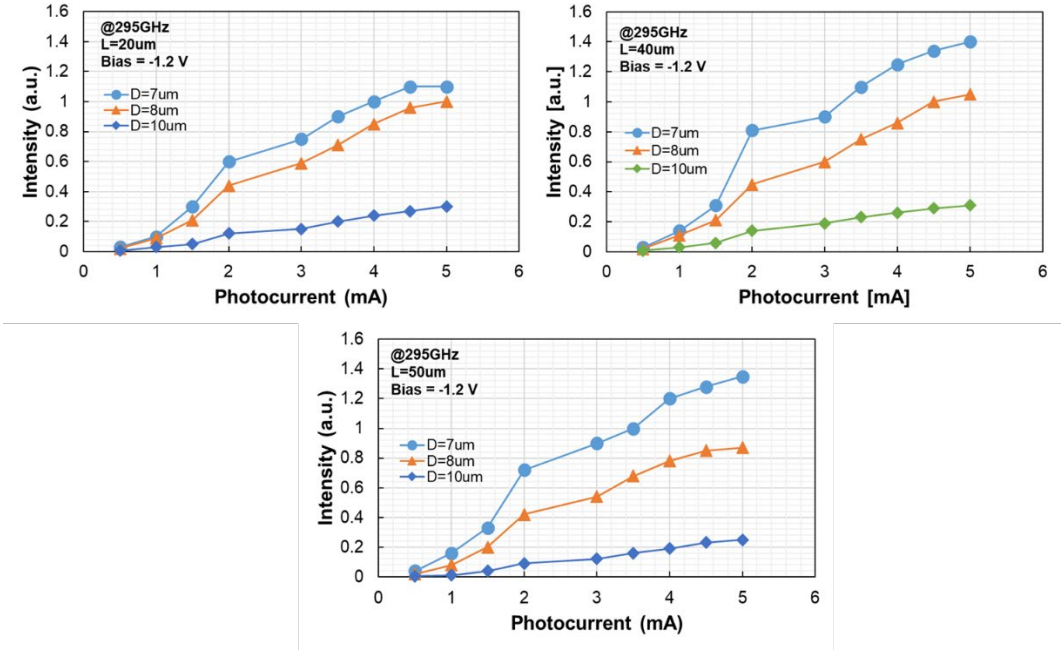

Figure 4.45: Measured THz wave intensity against photocurrent for different mesa diameters for L = 20 µm, 40 µm and 50 µm.

Furthermore, the device performance is also a function of length L that brings about an inductance thereby affecting the frequency response of the device. The THz wave intensity was measured as a function of frequency for different L at 295 GHz.

It can be depicted from figure 4.8 that there is an optimal L that gives the highest intensity for a given mesa diameter. The measured results suggest that L = 40 µm gives the highest intensity for 7 µm, 8 µm and 10 µm mesa diameters. The results further suggest that L = 20 µm, gives higher intensity than L = 50 µm for 8 µm and 10 µm mesa diameters whereas L = 50 µm gives higher intensity than L = 20 µm for 7 µm mesa diameter.

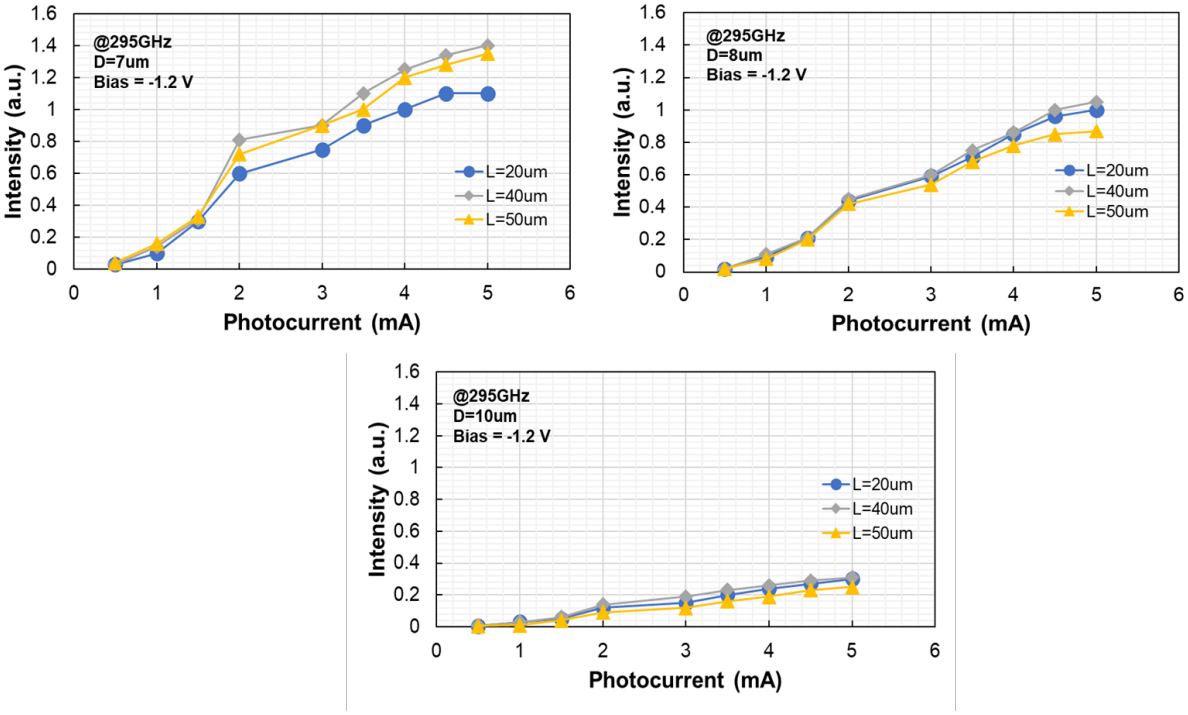

Figure 4.46: Measured THz wave intensity against photocurrent for different L for mesa diameters D = 7 µm, 8 µm and 10 µm

The device output linearity was assessed by analyzing the relationship between the photocurrent and the output power at a DC bias voltage of -1.5 V up to a point where the device saturates. Figure 4.9 shows the measurement results at 290 GHz with a bias voltage of -1.5 V for devices with mesa diameters of 6, 7, 8 and 10 µm when L = 40 µm.

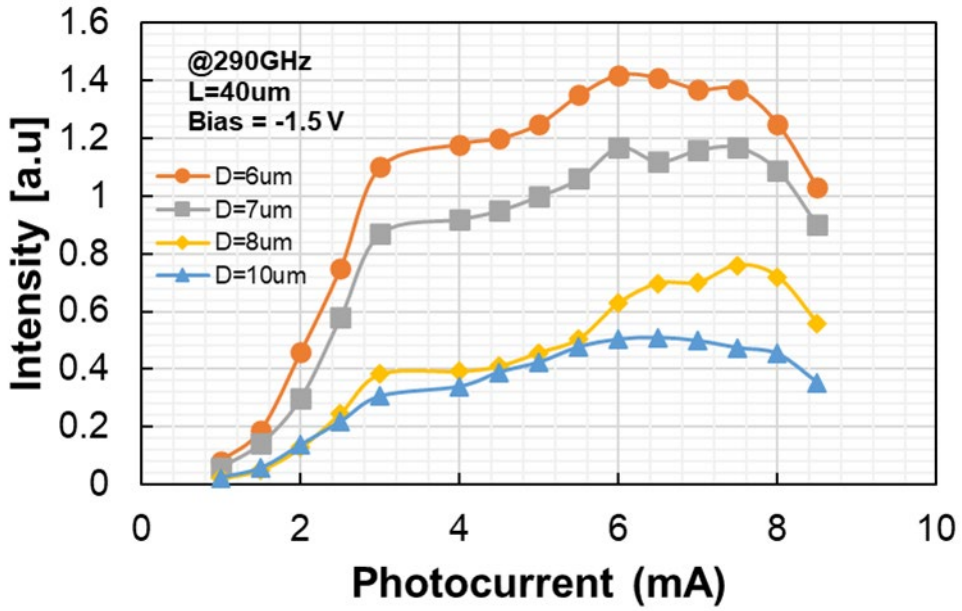

Figure 4.47: Measured THz wave intensity against photocurrent for different mesa diameters for L = 40 μm to determine the saturation photocurrent at 290 GHz.

The results show that the output power is directly proportional to the photocurrent up to around 7.5 mA for all devices, assuming the AC current is proportional to the DC current. However, there may be a slight discrepancy due to bias dependency in the UTC-PDs, thereby causing variations in the actual bias at the photodiodes at a fixed external bias voltage as the photocurrent changes. Beyond 7.5 mA of the total photocurrent from the two UTC-PDs, the output saturates as a result of space charge effect whereby with increasing photocurrent, the current density increases in the depletion layer until it reaches a critical value J_{max} that modulates the electric field profile causing a non-linear response and output saturation. This phenomena will be further discussed in Chapter 5.

4.5 Conclusion

A detailed account of the fabrication process and characterization of a UTC-PD integrated with a bow-tie antenna on Silicon Carbide (SiC) substrate to generate THz waves at high photocurrent has been given. The successful fabrication of UTC-PDs on SiC substrate highlights a promising approach to thermal management in high-power photonic devices.

The device characterization entails assessing the device frequency response, the effect of the fabricated device area by considering the mesa diameter, the length between the two *arms* of the bow-tie antenna as well as the device output linearity. Measurement results have shown that the device exhibits multiple peaks. These peaks are a function of the antenna impedance a well as the UTC-PD impedance and they occur at frequencies when the antenna impedance is a conjugate of the UTC-PD impedance. It is also depicted from the results that larger area devices give less intensity due to series resistance effects, increased capacitance, and increased carrier transit time. Conversely, they give higher photocurrent due to more photons being absorbed, generating more electron-hole pairs.

REFERENCES

[1] T. Sanjoh et al, “Thermal properties of III–V on a SiC platform for photonic integrated circuits,” Jpn. J. Appl. Phys. 58 SBBE06, 2019.

[2] Y. Shiratori, T. Hoshi, M. Ida, E. Higurashi and H. Matsuzaki, “High-Speed InP/InGaAsSb DHBT on High Thermal-Conductivity SiC Substrate,” IEEE Electron Device Letters, vol. 39, no. 6, pp. 807-810, June 2018.

[3] M. Takenaka and S.Takagi, “InP-based photonic integrated circuit platform on SiC wafer,” Opt. Express 25, 29993-30000 2017.

[4] M. Naftaly, J. F. Molloy, B. Magnusson, Y. M. Andreev, and G. V. Lanskii, “Silicon carbide—a high-transparency nonlinear material for THz applications,” Opt. Express 24, 2590-2595 2016.

[5] M. Mehregany, C. A. Zorman, “SiC MEMS: opportunities and challenges for applications in harsh environments,” Thin Solid Films, vol. 355–356,1999.

[6] Y. Muramoto and T. Ishibashi, “InP/InGaAs pin photodiode structure maximizing bandwidth and efficiency,” Electron. Lett. 39(24), 1749-1750 2003.

[7] Ito, H.; Shibata, N.; Nagatsuma, T.; Ishibashi, “T. Terahertz-wave detector on silicon carbide platform,” Appl. Phys. Express, 15, 2022.

[8] Y. Mushiake, [Self-Complementary Antennas], Springer-Verlag, London, 25-30 (1996).

[9] T. Ishibashi, A. Wakatsuki, and S. Kodama, “Development of photodiode technologies for millimeter/terahertz-wave signal generation,” Proc. Asia-Pacific Microwave Photonics Conference, FA-1.1.FA1.1.4 (2012).

[10] E. Rouvalis, C. C. Renaud, D. G. Moodie, M. J. Robertson, and A. J. Seeds, “Traveling-wave uni-traveling carrier photodiodes for continuous wave THz generation,” Opt. Exp., vol. 18, pp. 11105–11110, 2010.

[11] H. Ito, T. Ishibashi, “InP/InGaAs fermi-level managed barrier diode for broadband and low-noise terahertz-wave detection,” Jpn. J. Appl. Phys., vol. 56, 2016.

[12] H. Ito, T. Ishibashi, “Novel Fermi-level managed barrier diode for broadband and sensitive terahertz-wave detection,” in Proceedings of the 40th International Conference on Infrared, Millimeter, and Terahertz waves (IRMMW-THz), Hong Kong, China, 23-28 August 2015.

[13] H. Ito, T. Ishibashi, “Fermi-level managed barrier diode for broadband and low-noise terahertz-wave detection,” Electron. Lett., vol. 51 2015.

CHAPTER 5

MICROSTRIP PATCH ANTENNA AND COMBINER INTEGRATED DEVICES

In this chapter, a detailed account of the fabrication and characterization of arrayed UTC-PDs integrated with a patch antenna and a combiner on SiC substrate to verify the concept of on-chip power combining for enhanced radiated THz power is given. The characterization entails assessing the performance of the fabricated T-junction and Wilkinson combiner and antenna co-design with 2×1, 4×1, and 8×1 configurations.

5.1 T-JUNCTION COMBINER-ANTENNA INTEGRATED DEVICES

At first, a 2×1 T-junction combiner-antenna integrated device was characterized. Figure 5.1 (a) shows the schematic and photo of the fabricated device. The UTC-PD fabrication process described in Chapter 4 was followed. The p-metal of the PD was coupled to the microstrip 50 Ω lines of the T-junction combiner by a microstrip taper that was 22 µm long that acted as an impedance transformer between the 4 µm p-metal and the 30.6 µm 50 Ω lines . In contrast, the n-metal was coupled to the low pass filter by a 3.8 µm taper. The stepped impedance low pass filters (LPF) and the radial stubs as described in Chapter 3 were used as RF chokes in the biasing circuits of the UTC-PDs to prevent leakage of the RF signal into the DC bias lines.

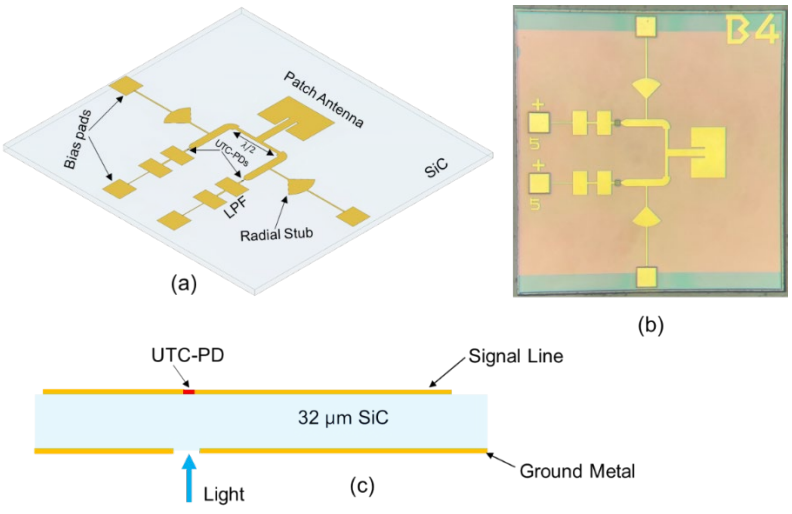

Figure 5.48: Device design. (a) Schematic of the monolithically integrated active and passive com-ponents (b) Photo of fabricated device (c) Schematic cross sectional view.

5.1.1 Experimental Setup

The experimental setup to characterize the device is shown in figure 5.2. The power combiner chip requires a module with holes on the back side when packaging because light is injected from the back side of the module. The chip was set up on a gold-deposited glass slide of 150 µm thickness with a slit of about 0.3 mm as shown in figure 5.3. Using gold-deposited glass slides enables chips to be mounted without eliminating the function of the chip's ground conductor plate. A voltage was applied to the chip via bonding wires. Furthermore, the bonding wires were connected through a capacitor to avoid damage to the UTC-PD due to static electricity. A pair of wavelength tunable laser diodes, LD1 and LD2, emitted two lightwaves with a power of 10 dBm and frequencies of 193.1 and 193.4 THz, respectively. The lightwaves were combined by an optical coupler (OC), modulated at 1 MHz by an intensity modulator (IM), and then amplified by an Erbium doped fiber amplifier (EDFA). The amplified optical signal was split into two optical paths by an optical splitter (OS). The lengths of the two paths were tuned using optical delay lines (ODLs). The two optical signals were then introduced to two UTC-PDs through a micro-lens array (MLA). At each UTC-PD, an alternating current (AC) with a frequency of 300 GHz was generated. These currents were combined by a T- junction power combiner and fed to a rectangular microstrip patch antenna to radiate the 300 GHz wave. The radiated wave was detected using a Fermi-level managed barrier diode (FMBD) [1, 2, 3] equipped with two 25 mm aperture THz lenses that are 50 mm apart at 18 mm away from the FMBD and 32 mm away from the device. The relative intensity of the 1 MHz component of the detected THz wave was measured using a lock-in amplifier (LIA).

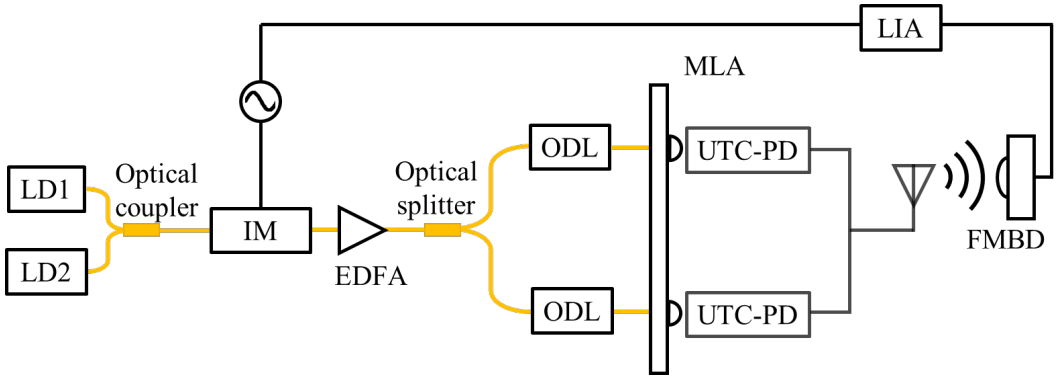

Figure 5.49: Experimental setup

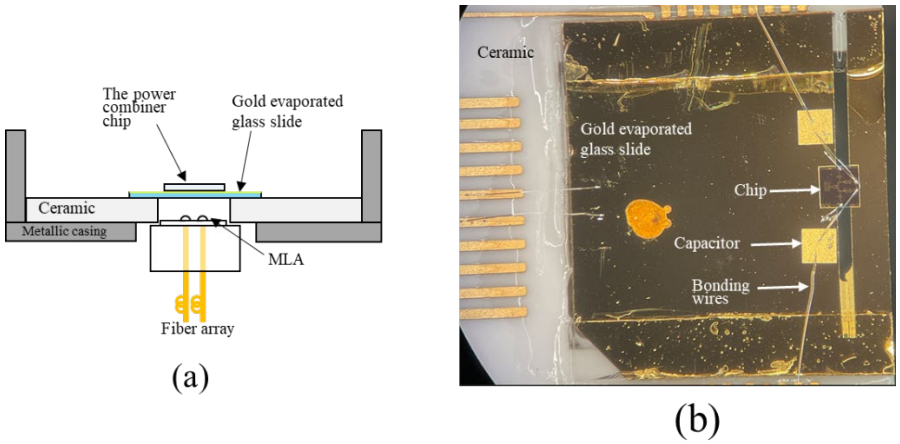

Figure 5.50: (a) Chip irradiation configuration, (b) chip photo on gold evaporated glass slide.

5.1.2 Device Characterization

To assess the feasibility of power enhancement by combining currents at the MSL-based T-junction combiner, the device frequency response, the coherency of combined photocurrents, the UTC-PD bias voltage effect on output power, output linearity and radiation pattern.

5.1.2.1 Frequency Response of a 2 by 1 T-junction Combiner Integrated Device

The THz wave intensity emitted by the device in figure 5.4, was measured between 200 GHz and 400 GHz at a photocurrent of 7 mA and a -1 V bias voltage.

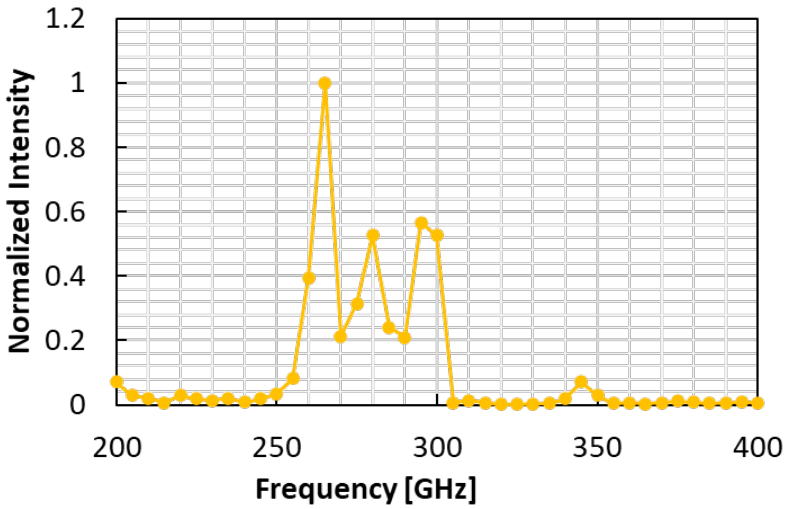

Figure 5.51: Measured frequency response of a 2 × 1 T-junction combiner integrated device.

The emitted power of an antenna is influenced by two factors: the efficiency of energy coupling with the driving source and the radiation efficiency. The former refers to the proportion of power provided by the source that is effectively utilized by the antenna, while the latter determines the proportion of power received by the antenna that is transmitted into free space. On the other hand, the antenna directivity describes the distribution of power in different angles when it is radiated. The optimal transfer of power between the source and antenna occurs when the impedance of the antenna is equal to the complex conjugate of the source impedance [4], [5]. Consequently, we can anticipate local peaks in the radiated power at frequencies where the reactance of the source and antenna have similar absolute values but opposite signs, and the real parts of their impedances are comparable. Figure 5.5 shows the simulated device Z-parameters. The UTC-PD impedance can be approximated to be

$$Z_{UTCPD} \approx R - j2\pi fC, \tag{5-1}$$

where the resistance R and capacitance C are approximated as [6], [7]

$$R \approx \frac{d}{q\mu A n_0}, \tag{5-2}$$

$$C \approx \frac{\varepsilon_0 \varepsilon_r A}{d}. \tag{5-3}$$

In the above equations, d is the thickness of the depletion region that is about 1 μm, q is the electron charge (1.6×10^{-19} C), μ is the electron mobility estimated to be 5000 cm^2/Vs, and the carrier density $n_0 \approx 10^{16} cm^{-3}$, area $A \approx 21\ \mu m^2$, $\varepsilon_0 = 8.85 \times 10^{-12} F/m$ and $\varepsilon_r = 12$.
Although the above equations give $R \approx 6\ \Omega$ and $C \approx 20\ fF$, we assume that the resistance can be higher, $R \approx 25\ \Omega$ and the capacitance can be lower, $C \approx 10\ fF$.

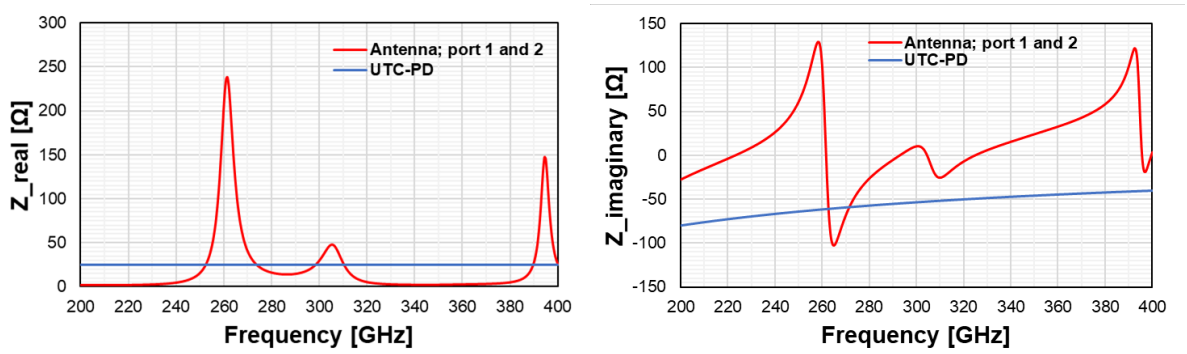

Figure 52.5: Simulated Z-parameters for the 2 × 1 T-junction combiner integrated device.

Figure 5.6 shows the calculated radiated power, without considering the antenna properties such as gain, directivity and radiation efficiency which could be referred to as the accepted power by the antenna.

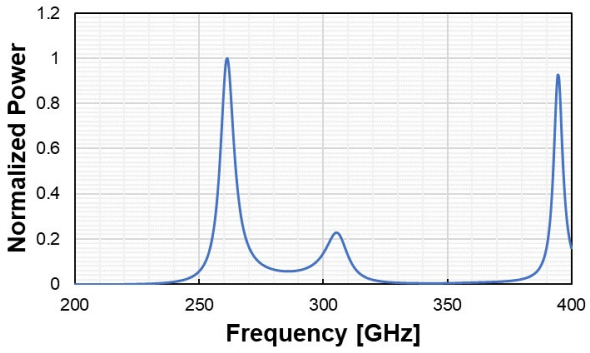

Figure 5.53: Calculated radiated power as a function of impedance matching between the antenna and the UTC-PD.

The peaks for calculated power at 261 GHz and 305 GHz seem to correspond with the measured power peaks at 265 GHz and 300 GHz. The measured peak at 280 GHz is not observed in the calculated results and it could be because of the antenna characteristics which are not accounted for in the calculation or measurement. Conversely, the calculated power peak at 395 GHz, is not observed in the measured power and this could be because of the low directivity at 395 GHz as shown in figure 5.7 when the receiver (FMBD) is in the upward direction (theta = 0 degrees) and measurements taken in the xz direction (phi = 0 degrees).

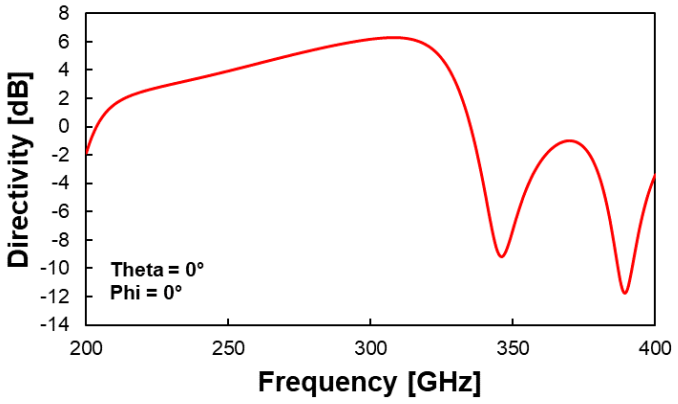

Figure 5.54: Directivity versus Frequency for the 2 × 1 T-junction combiner integrated device.

The radiated power level is influenced by various factors such as radiation efficiency, directivity (solid angle considered for power calculation), and transit-time limited response of the UTC-PD. Given the complexity of predicting the absolute power radiated by a system with numerous variables, the agreement between experimental and numerical results presented can be considered highly satisfactory.

5.1.2.2 Coherency of Combined Photocurrent by the T-junction Combiner

In order to achieve coherent signal combining in a T-junction combiner, it is necessary that the phases of the currents being fed into the combiner to be the same. This means that the peaks and dips of the two alternating currents align with each other, which results in constructive interference thus leading to effective signal combining. To vary the phases for the two lightwaves in different optical paths, a manually operated optical delay line (ODL) was used. By varying the optical path length, the phase of the two alternating currents was changed. This allowed for controlling the interference pattern that would be observed when the two currents were combined. Figure 5.8, illustrates the power plot of the 300 GHz wave detected by the FMBD. The graph depicted a clear interference pattern at a fitted sinusoidal curve. The period of this curve is about 1 mm, corresponding to the interference period of the two 300 GHz currents. Also, since power decreases down to zero, it is confirmed that the T-junction combiner provides an ideal coherent current combining.

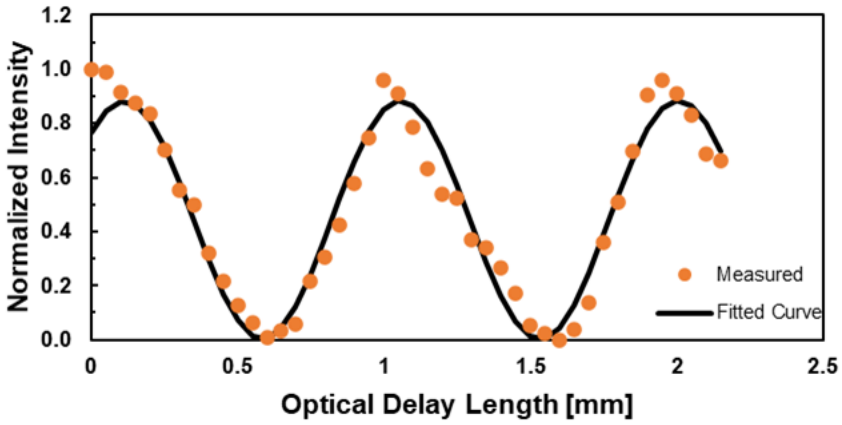

Figure 5.55: 300 GHz wave intensity as a function of delay length in the optical path.

5.1.2.3 UTC-PD Bias Voltage Effect on Output Power

The THz-wave output power changes significantly with respect to the bias voltage as shown in figure 5.9. At 300 GHz, the output starts to build up at +0.25 V bias voltage with an optical input power of 20 dBm. As the negative bias voltage increases, there's a rapid increase in output. The optimal bias voltage (V_{opt}) that produces the highest output is -1.1 V, and beyond this point, the output decreases. It should be noted that at a photocurrent of 7 mA for each UTC-PD, the output is linear and so, the space charge effect is not causing the output degradation beyond V_{opt}. Thus, the output variation is possibly due to the electron velocity overshoot effect, that is sensitive to the electric field intensity [8,9] whereby a certain range of electric field intensities within the depletion layer can cause electrons to exceed their saturation velocity which affects the response of the UTC-PD, which is determined by the carrier transit time, thereby affecting the output. The optimum field intensity E in a 0.23 μm depletion layer corresponding to a bias voltage of −1.1 V at 300 GHz is calculated to be 80 kV/cm using

$$E = \frac{(V_{bu} - V_{bias})}{W_C} \qquad (5-4)$$

where the built in voltage $V_{bu} = 0.75\,V$ and the depletion layer width $W_c = 0.23\,\mu m$. This field intensity can lead to an electron velocity between 3×10^7 - 6×10^7 cm/s. This assertion is in agreement with the experimental and theoretical results reported in [8,9], where −1.2 V (80 kV/cm), −0.8 V (67 kV/cm) and −0.4 V (50 kV/cm) gave the maximum output at 250 GHz, 500 GHz, and 1 THz respectively.

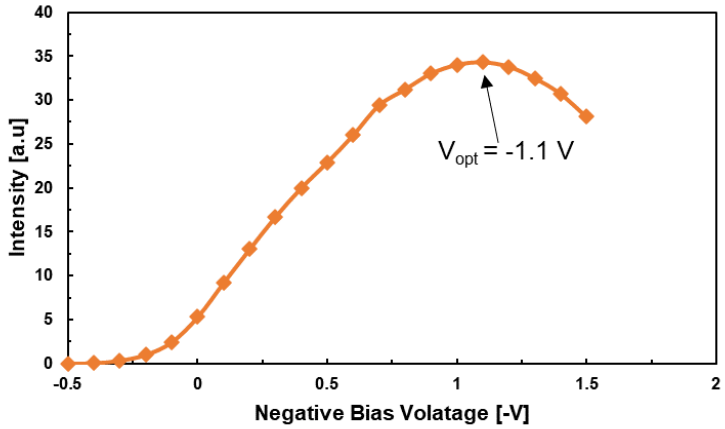

Figure 5.56: Measured THz wave intensity with respect to applied negative bias voltage at 20 dBm optical input power.

5.1.2.4 Output Linearity with Respect to Photocurrent due to Space Charge Effect

One of the most important characterization parameters of a UTC-PD based photomixer for THz application is the output linearity range which alludes to the device saturation output. The device output linearity was assessed by analyzing the relationship between the square of the total photocurrent produced by the UTC-PDs and the output power at a -1 V bias voltage. Before conducting the measurements, the ODL was carefully adjusted to ensure optimal output power. To avoid any damage or negative effects to the photodiode, measurements were taken up to an optical input power of 24 dBm, resulting in a photocurrent of 11 mA from each UTC-PD. Figure 5.10 shows that the results align with the theoretical assertion that the output power is proportional to the square of the photocurrent up to around 10 mA from each UTC-PD, assuming the AC current is proportional to the DC current. However, there may be a slight discrepancy due to bias dependency of the UTC-PDs, leading to variations in the actual bias at the photodiodes despite a fixed external bias voltage as the photocurrent changes. Beyond 20 mA of the total photocurrent from both UTC-PDs, the output saturates as a result of space charge effect whereby with increasing photocurrent, the current density increases in the depletion layer until it reaches a critical value J_{max} that modulates the field profile therein causing a non-linear response and output saturation. The UTC-PD used has an absorption area of about ~19 μm^2 defined by wet mesa etching, hence, the peak photocurrent of 10 mA suggests that the critical current density is ~53 kA/cm^2. Considering inevitable measurement inconsistencies and errors, to a great extent, this is consistent with the theoretical J_{max} estimated to be about 48 – 96 kA/cm^2 using

$$J_{max} = qn_c v_s \qquad (5-5)$$

where the carrier density $n_c = 10^{16}$ and v_s can be estimated to be about 3×10^7 - 6×10^7 cm/s [28].

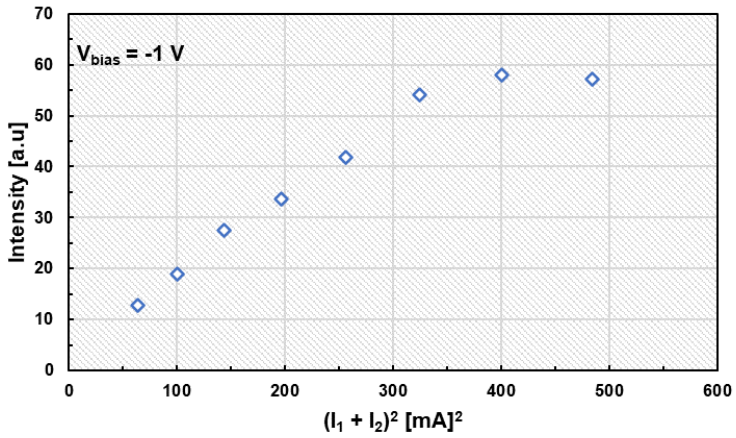

Figure 5.57: THz wave intensity versus the square of the total photocurrent.

5.1.2.5 2 by 1 T-junction Combiner Integrated Device Radiation Pattern

The power combining capability of the 2×1 device was examined with a radiation pattern of 80 degrees beamwidth with a -1 V bias voltage and a photocurrent of 7 mA. As depicted in figure 5.11, when both UTC-PDs were irradiated, the measured power was about 5.8 dB higher relative to a single UTC-PD irradiation over all the angles. These results were consistent with the theoretical explication that doubling the number of UTC-PDs results in a fourfold increase in the emitted power. The difference of 0.2 dB from the expected power gain of 6 dB is thought to be due to the slight disparity in the photocurrents from the two UTC-PDs. It is important to highlight that this technique of combining THz waves by parallel connection of UTC-PDs to an antenna, allows for isotropic amplification of the THz radiation intensity, making it more efficient in converting optical-to-THz-wave power without necessarily narrowing the beam width compared to using the method of arrayed antennas with UTC-PDs. Although the latter approach is also highly effective in enhancing the peak power of the radiated THz wave, it necessitates an alignment of the beam towards the receiver due to its highly directional radiated pattern.

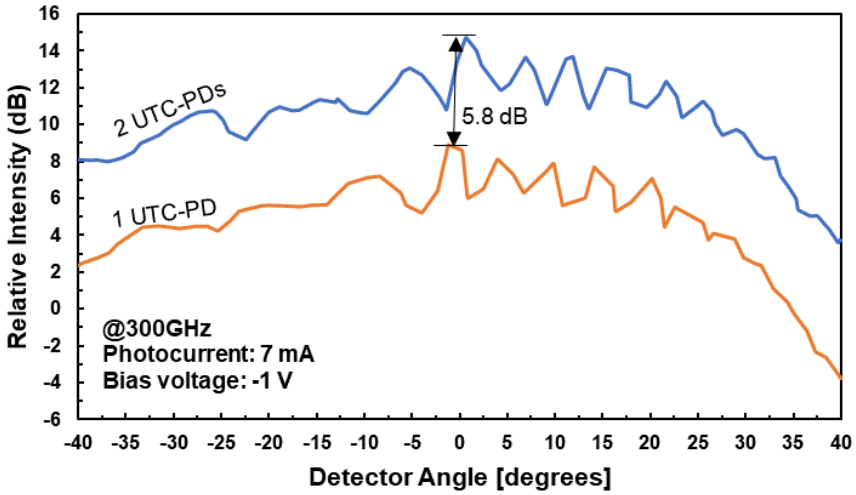

Figure 5.58: Radiation pattern for single and double UTC-PD irradiation.

5.1.3 Frequency Responses for 4 by 1 and 8 by 1 T-junction Combiner Integrated Devices

Moreover, the 4 × 1 and 8 × 1 T-junction combiner integrated devices shown in figure 5.12, were also characterized in terms of their frequency responses.

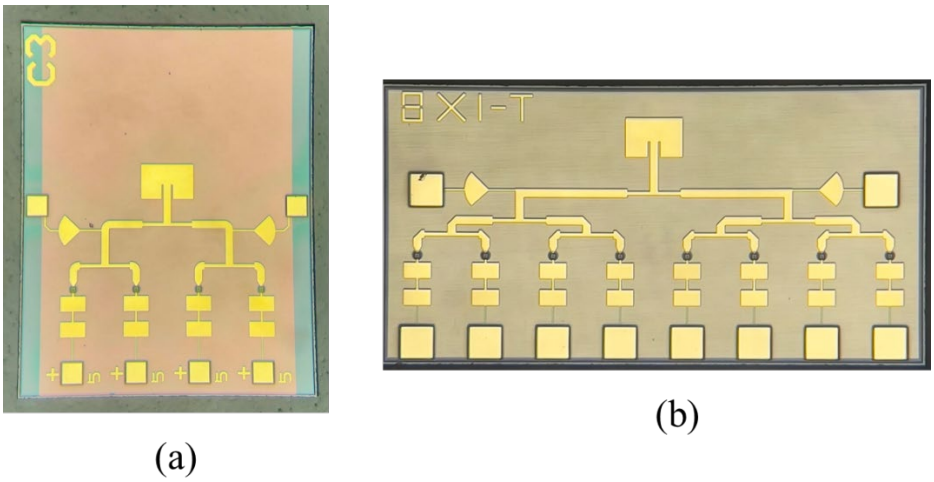

Figure 5.59: Photo of fabricated T-junction combiner integrated devices; (a) 4 × 1 (b) 8 × 1.

As explained with the 2 × 1 T-junction combiner integrated device, local peaks in the radiated power were realized at frequencies where the reactance of the source (UTC-PD) and antenna have similar absolute values but opposite signs, and the real parts of their impedances are comparable. Figure 5.13 shows the measured frequency response for both devices.

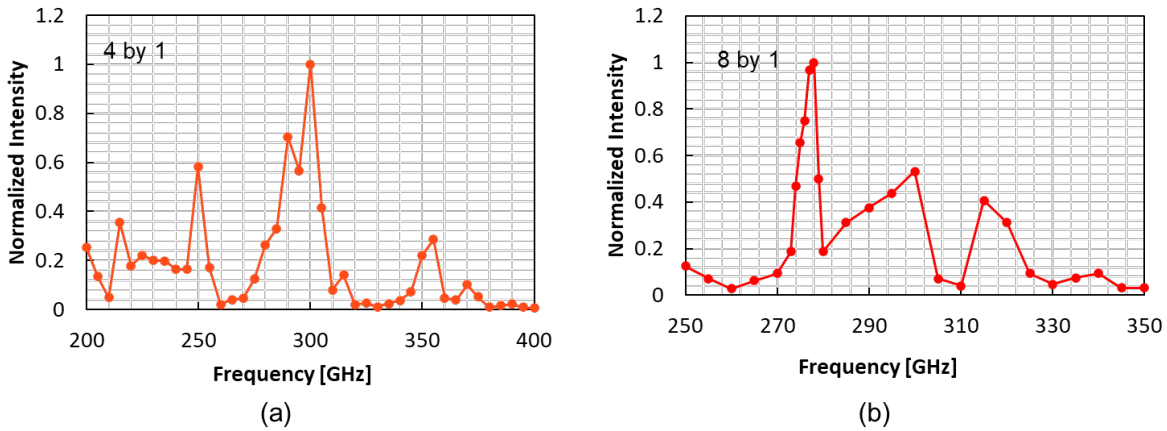

Figure 5.60: Measured frequency response; (a) 4 × 1, (b) 8 × 1.

Figure 5.14 shows the simulated Z-parameters and figure 5.15 shows the calculated radiated power without considering the antenna properties such as gain, directivity and radiation efficiency.

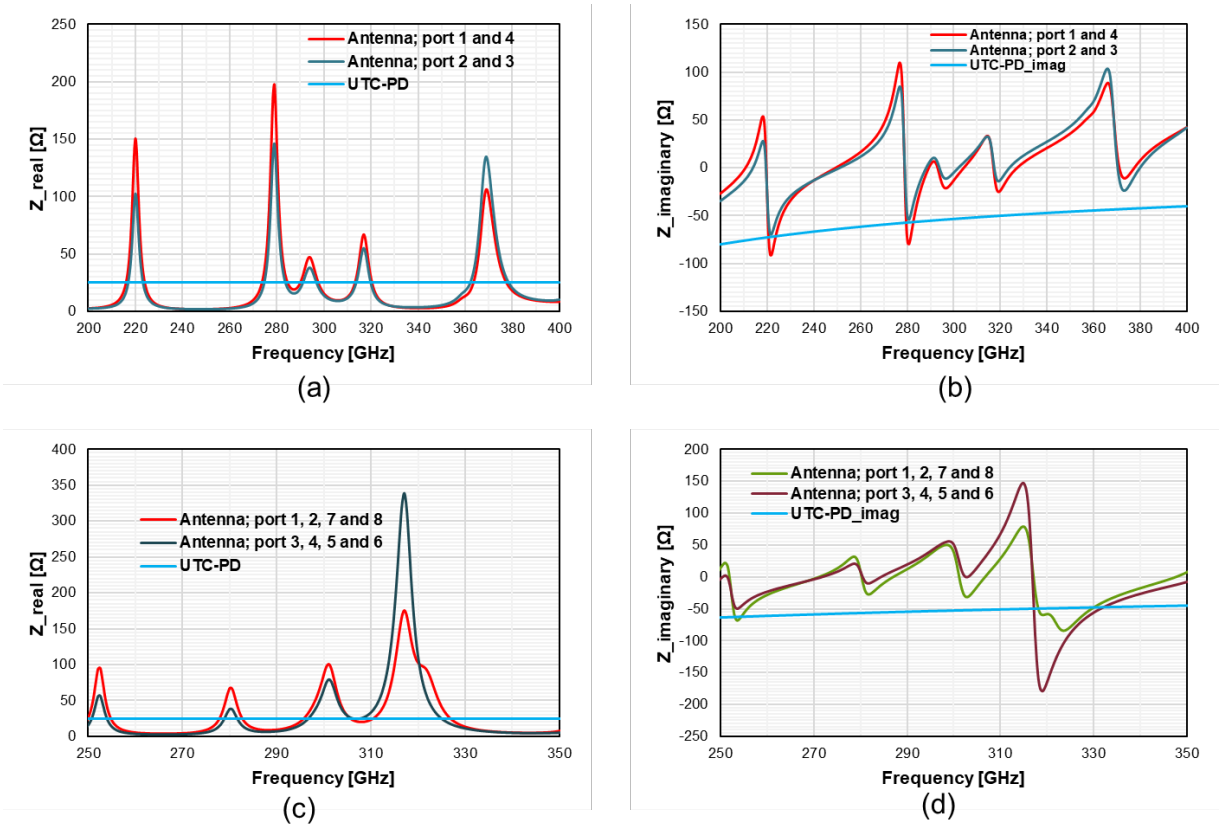

Figure 5.61: Simulated Z-parameters for the T-junction combiner integrated device: (a) 4 × 1 real impedance part, (b) 4 × 1 imaginary impedance part, (c) 8 × 1 real impedance part, (d) 8 × 1 imaginary impedance part.

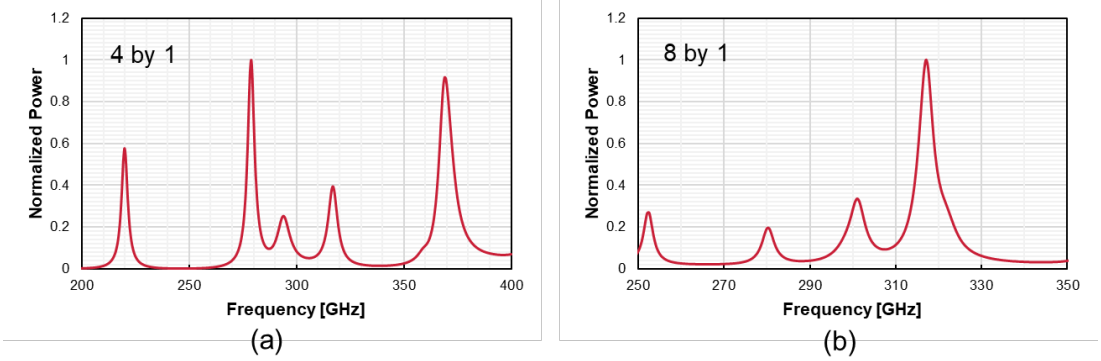

Figure 5.62: Calculated radiated power as a function of impedance matching between the antenna and the UTC-PD T-junction combiner integrated device; (a) 4 × 1, (b) 8 × 1.

For both devices, peaks in the radiated power were realized at frequencies where the reactance of the source (UTC-PD) and antenna have similar absolute values but opposite signs, and the real parts of their impedances are comparable.

5.1.4 4 by 1 and 8 by 1 T-junction Combiner Integrated Devices Radiation Patterns

The 4 × 1 device radiation pattern was measured in a 60 degrees beamwidth with a -1 V bias voltage and a photocurrent of 7 mA, at 300 GHz. Figure 5.16 shows that the radiated THz wave intensity was enhanced by 11.4 dB (fourteenfold). This is consistent with the theoretical assertion that when the number of UTC-PDs is increased by a factor of n, the power is multiplied by n^2. In the case 4 UTC-PDs, the expected increment would be 12 dB and the 0.6 dB loss is due to the inevitable device losses and systematic errors.

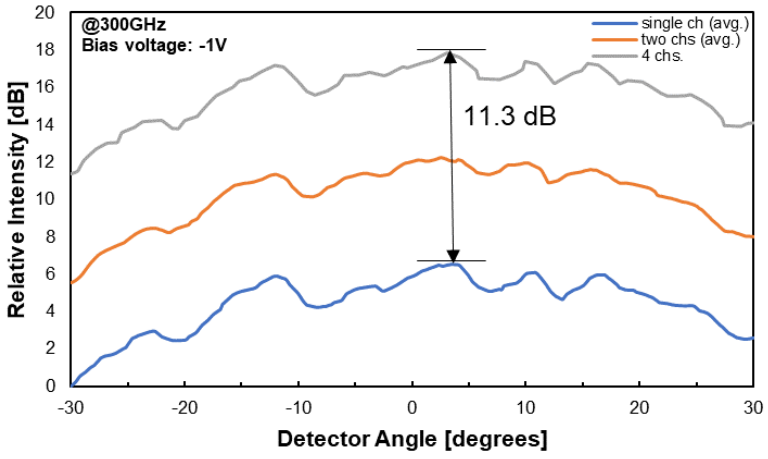

Figure 5.63: 4 × 1 T-junction combiner integrated device radiation pattern.

Furthermore, an 8 × 1 device was also characterized at 278 GHz with a radiation pattern of 60 degrees beamwidth with a -1 V bias voltage and a photocurrent of 4 mA. Results shown in figure 5.17 indicate that the device can enhance the radiated THz wave intensity by 16.4 dB (forty four times). Although the ideal enhancement would be 18 dB, the results are largely in agreement with the theoretical assertion.

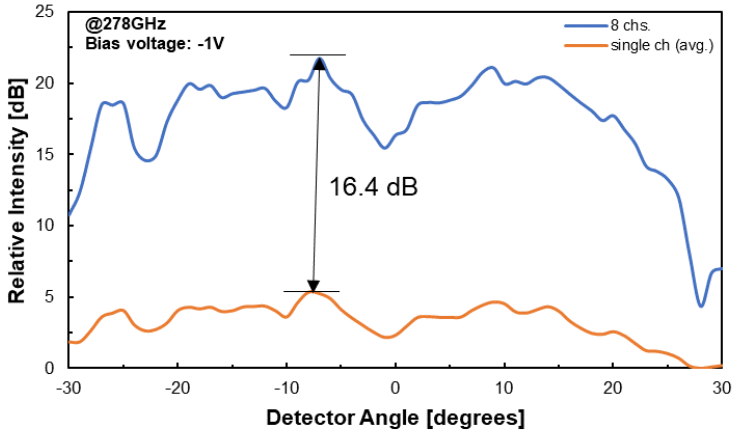

Figure 5.64: 8 × 1 T-junction Combiner Integrated Device Radiation Pattern.

5.2 WILKINSON COMBINER-ANTENNA INTEGRATED DEVICES

The experimental setup and measurements for the characterization of the T-junction combiner device were used to characterize the Wilkinson combiner device. At first, a 2 × 1 Wilkinson combiner-antenna integrated device was characterized. Figure 5.18 shows the schematic and photo of the fabricated device. The UTC-PD fabrication process described in Chapter 4 was followed.

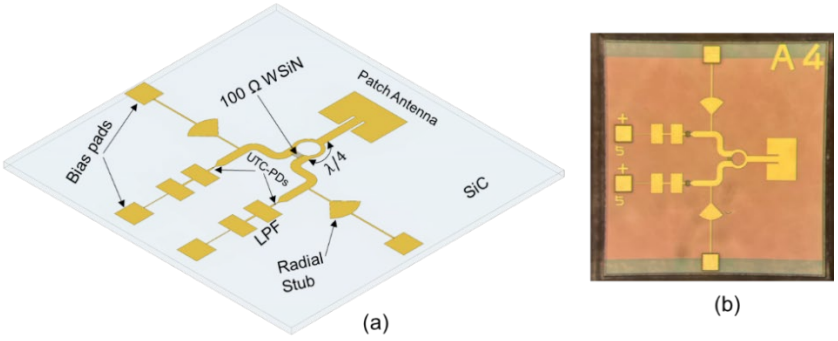

Figure 5.65: 2 × 1 Wilkinson divider Device design; (a) Schematic of the monolithically integrated active and passive com-ponents (b) Photo of fabricated device.

On the 32 µm thick SiC substrate, the Wilkinson combiner was fabricated comprising two 50 Ω input microstrip lines that are 30.6 µm wide and 250 µm apart which corresponds to the fiber array pitch used in this work, and two 70.71 Ω $\lambda/4$ transformer lines that are 13.3 µm wide. The Wilkinson power combiner provides relatively better matching between ports and high isolation compared to alternative combiners like a T-junction combiner because of the resistor between the two input ports. A Tungsten Silicon Nitride (WSiN) sheet layer was used to achieve the 100 Ω isolation resistance which corresponds to $2Z_0$ where Z_0 is the input lines characteristic impedance. The resistor does not dissipate power hence making the Wilkinson power combiner to be lossless theoretically. However, practically, there may be some minimal losses.

5.2.1 Frequency Response of a 2 by 1 Wilkinson Combiner Integrated Device

The THz wave intensity emitted by the device in figure 5.19, was measured between 200 GHz and 400 GHz.

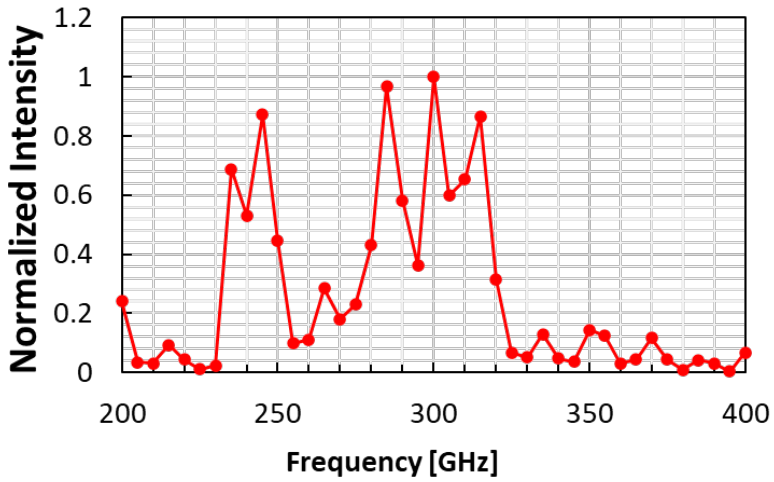

Figure 5.66: Measured frequency response of a 2 × 1 Wilkinson combiner integrated device.

Figure 5.20 shows the simulated Z- parameters and figure 5.21 shows the calculated radiated power, without considering the antenna properties such as gain, directivity and radiation efficiency. Peaks in the radiated power were realized at frequencies where the reactance of the source (UTC-PD) and antenna have similar absolute values but opposite signs, and the real parts of their impedances are comparable.

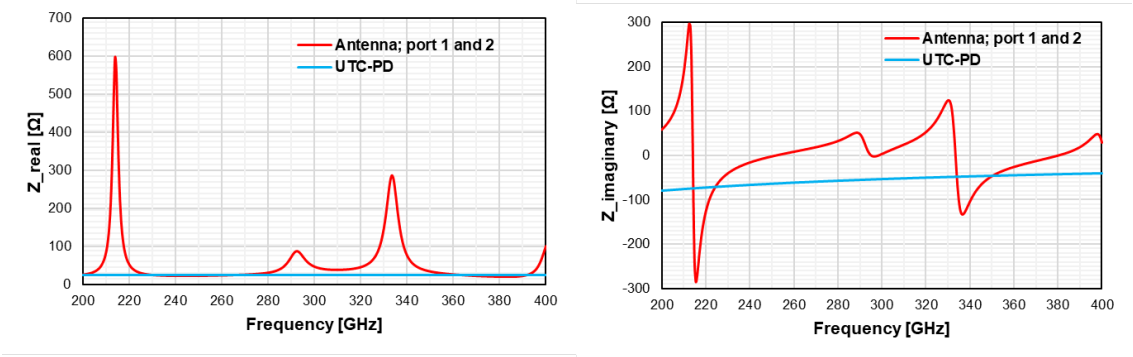

Figure 5.67: Simulated Z-parameters for the 2 × 1 Wilkinson combiner integrated device; (a) real impedance part, (b) imaginary impedance part.

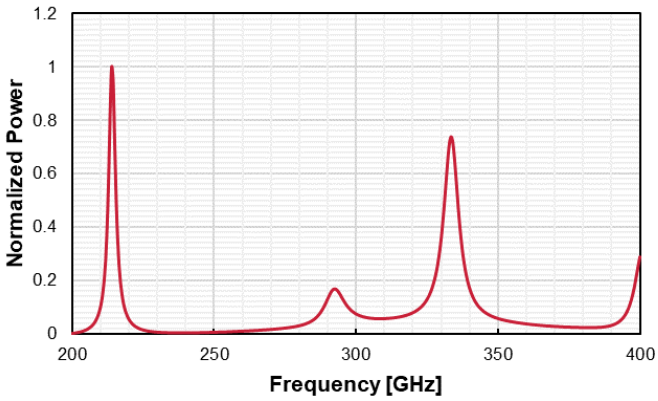

Figure 5.68: Calculated radiated power as a function of impedance matching between the antenna and the UTC-PD for the 2 × 1 Wilkinson combiner integrated device

5.2.2 Coherency of Combined Photocurrent by the Wilkinson Combiner

The coherent combining of photocurrents from the two UTC-PDs by a 2 × 1 Wilkinson power combiner was examined. In figure 5.22, the power of the 300 GHz wave detected by the FMBD is plotted. The resulting graph showed a clear interference pattern with a period of 1 mm, which corresponds to the expected interference period between two 300 GHz alternating currents. Additionally, the fact that the power decreases to zero confirms that the Wilkinson combiner enables an ideal coherent combining of the two 300 GHz alternating currents generated at the UTC-PDs.

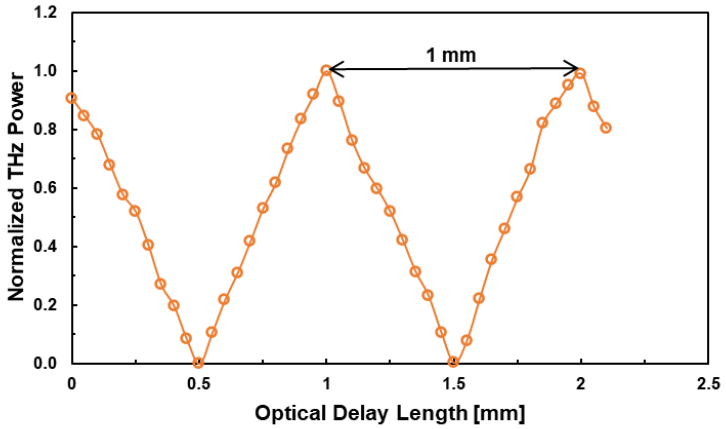

Figure 5.69: Measured power at 300 GHz as a function of optical delay length for the 2 × 1 Wilkinson combiner integrated device.

To confirm the output linearity with respect to photocurrent due to space charge effect, the relationship between the square of the total photocurrent produced by the UTC-PDs and the output power at a DC bias voltage of -1 V was analyzed as it was the case with the T-junction combiner device. The results as depicted in figure 5.23, confirmed output saturation beyond 20 mA total photocurrent due to space charge effect. This effect is related to the critical current density J_{max} for a given voltage (-1 V) which modulates the electric field profile leading to output saturation. It is needful to note that because of the electron velocity overshoot effect, the field modulation by space charge effect is significantly less in a UTC-PD. As a result, UTC-PDs can deliver greater output saturation levels as compared to conventional pin-PDs.

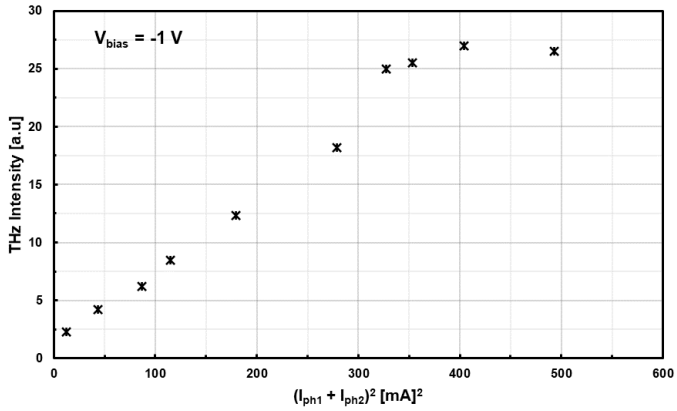

Figure 5.70: THz Power versus the square of the combined photocurrents for the 2 × 1 Wilkinson combiner integrated device.

5.2.3 2 by 1 Wilkinson Combiner Integrated Device Radiation Pattern

Figure 5.24 depicts the results of the relative radiated power measurement for a 2×1 device. The minimum detected power at a beamwidth of 60 degrees from the vertical axis when activating one UTC-PD was established as a reference (0 dB). At approximately -1 degree, the measured relative peak power was 7.5 dB when UTC-PD1 with a photocurrent of 8 mA was activated and 10.4 dB for UTC-PD2 with a photocurrent of 10 mA. Upon activating both UTC-PDs (18 mA), the relative peak power reached 14.8 dB, depicting a 7.3 dB increase in power relative to the power obtained with UTC-PD1 (8 mA) and a 4.4 dB increase in power relative to the power obtained with UTC-PD2 (10 mA). This suggests that a 2.25-fold increase in photocurrent results in a 5-fold increase in radiated power, while a 1.8-fold increase in photocurrent leads to a 2.75-fold increase in radiated power. Despite some losses, these findings are largely consistent with the theory that a factor of n increase in photocurrents corresponds to a factor of n^2 increase in radiated power.

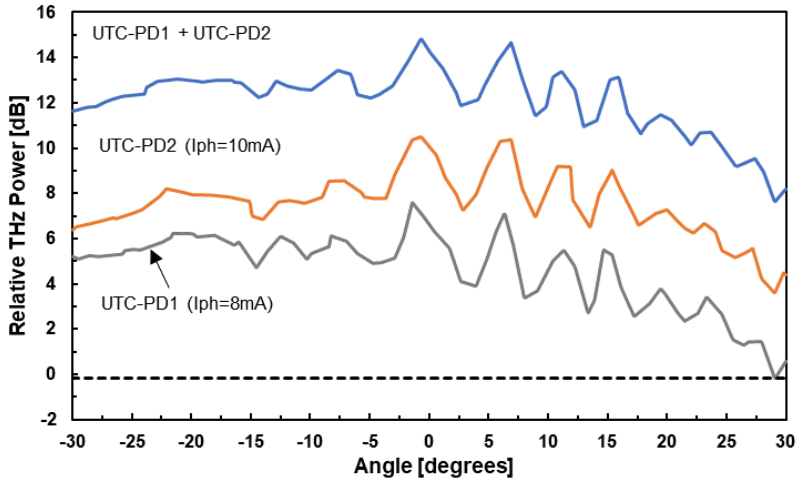

Figure 5.71: 2 × 1 Wilkinson Combiner Integrated Device Radiation Pattern.

5.2.4 4 by 1 Wilkinson Combiner Integrated Device

Moreover, a 4 × 1 device shown in figure 5.25, was also assessed in terms of its frequency response. As depicted in figure 5.26, the peaks at different frequencies are realized when the antenna impedance is a conjugate of the UTC-PD impedance as shown in figure 5.27.

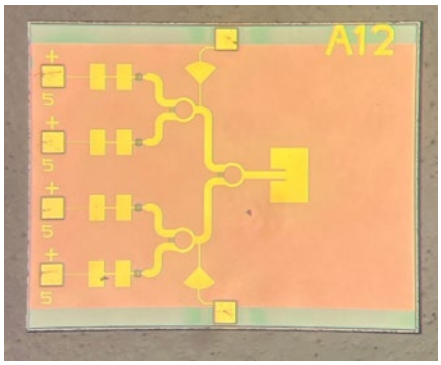

Figure 5.72: Photo of fabricated 4 × 1 Wilkinson Combiner Integrated Device.

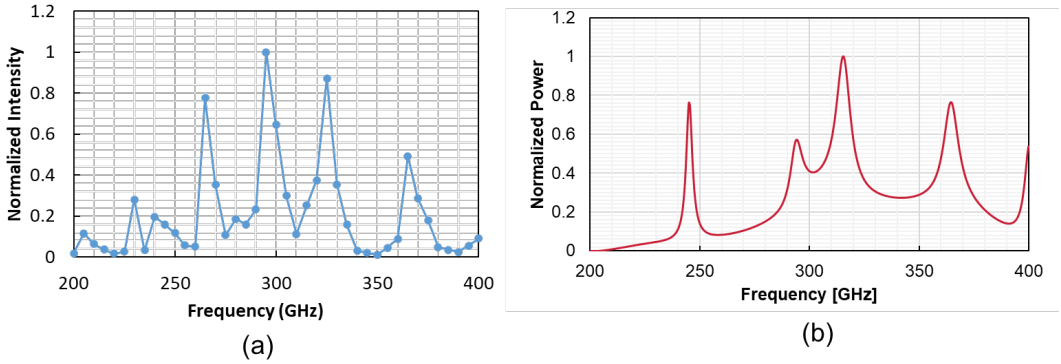

Figure 5.73: 4 × 1 Wilkinson Combiner Integrated Device Frequency response; (a) measured, (b) calculated.

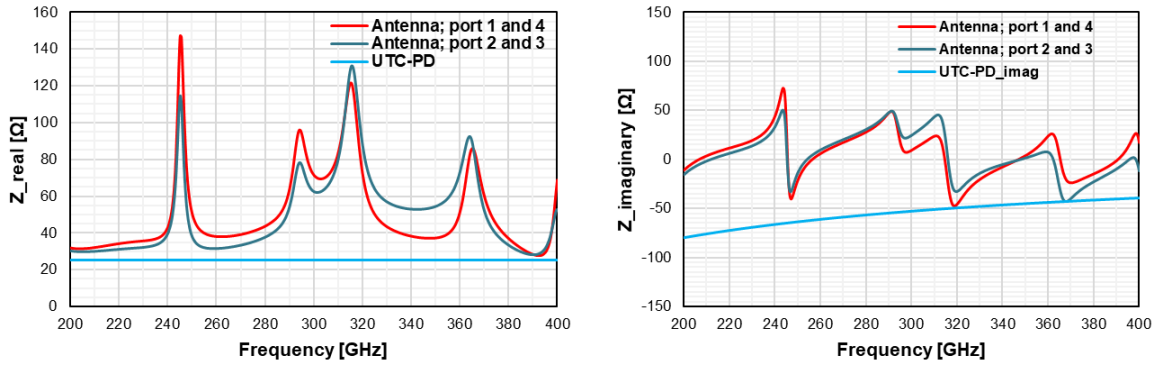

Figure 5.74: Simulated Z-parameters for the 4 × 1 Wilkinson combiner integrated device; (a) real impedance part, (b) imaginary impedance part.

In terms of the radiation pattern, the radiated THz wave intensity at 300 GHz as depicted in figure 5.28 was enhanced by 11 dB which is consistent with the theoretical assertion that when the number of UTC-PDs is increased by a factor n, the power is multiplied by n^2.

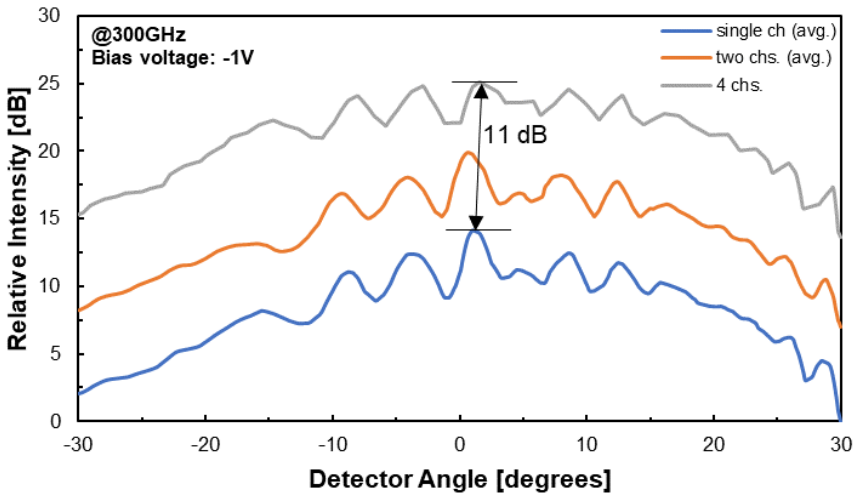

Figure 5.75: 4 × 1 Wilkinson Combiner Integrated Device Radiation Pattern.

5.3 8 by 1 COUPLED LINE WILKINSON COMBINER-ANTENNA INTEGRATED DEVICE

Furthermore, the concept of on-chip power combining was verified by an 8 × 1 Coupled line Wilkinson combiner-Antenna integrated device. The fabricated device is shown in figure 5.29. It's important to note that the combiner is easier to fabricate than the conventional Wilkinson combiner since during the semiconductor fabrication process, it's always easier to fabricate straight microstrip transmission lines than curved ones. Also, it's $\lambda/4$ lines cover a half area of 0.1 × 0.055 mm^2 compared to the conventional Wilkinson combiner. Thus, the coupled line Wilkinson combiner can be a better choice for monolithic integration of components at THz frequencies.

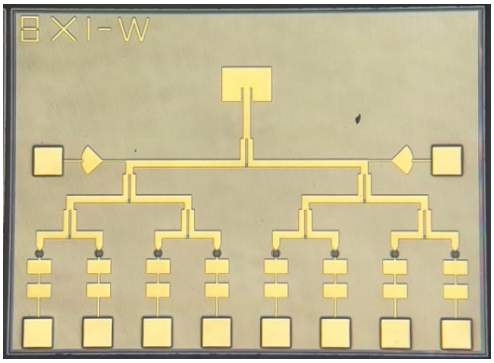

Figure 5.76: Photo of fabricated 8 × 1 coupled line Wilkinson combiner integrated device.

The measured and calculated frequency response is depicted in figure 5.30. The peaks at different frequencies are realized when the antenna impedance is a conjugate of the UTC-PD impedance. The simulated Z-parameters and the calculated power are shown in figure 5.31.

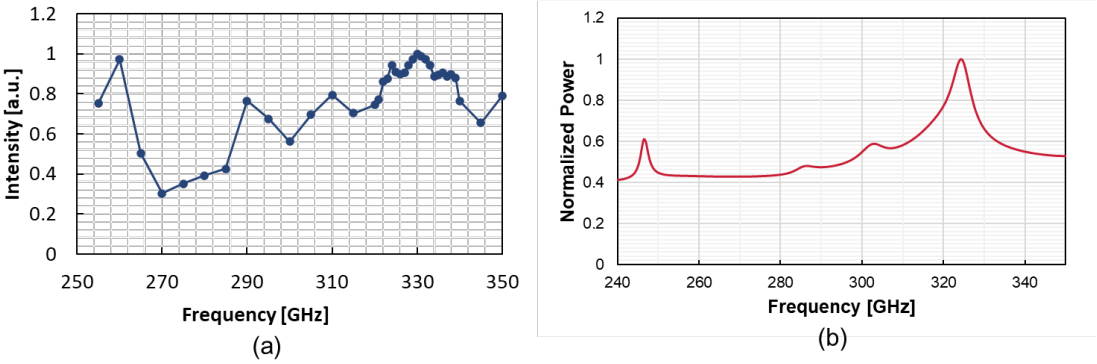

Figure 5.77: 8 × 1 coupled line Wilkinson combiner integrated device frequency response; (a) measured, (b) calculated

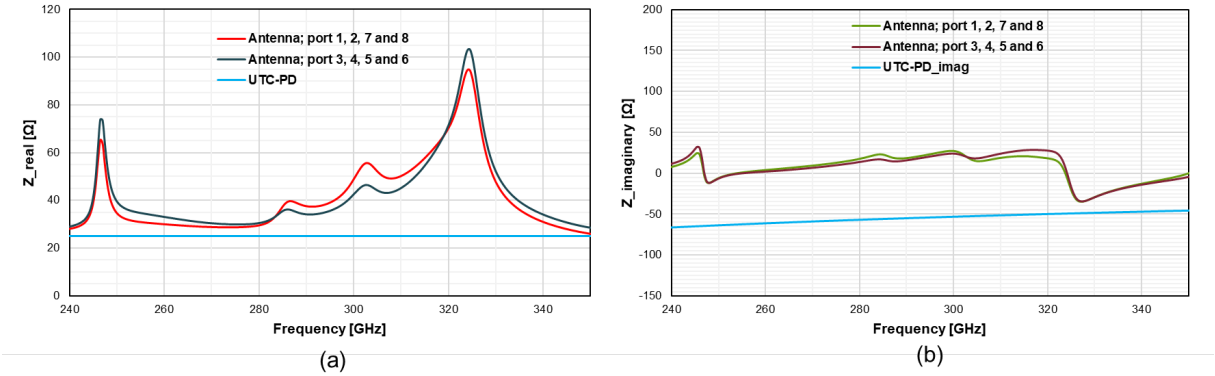

Figure 5.78: Simulated Z-parameters for the 8 × 1 coupled line Wilkinson combiner integrated device; (a) real impedance part, (b) imaginary impedance part.

The radiation pattern of 60 degrees beamwidth with a -1 V bias voltage and a photocurrent of 4 mA at 330 GHz as illustrated in figure 5.32. The radiated THz wave intensity can be enhanced by 15.7 dB (thirty seven times) relative to a single UTC-PD. Notably the results indicate that the device exhibit more losses than an 8 by 1 T-junction combiner device.

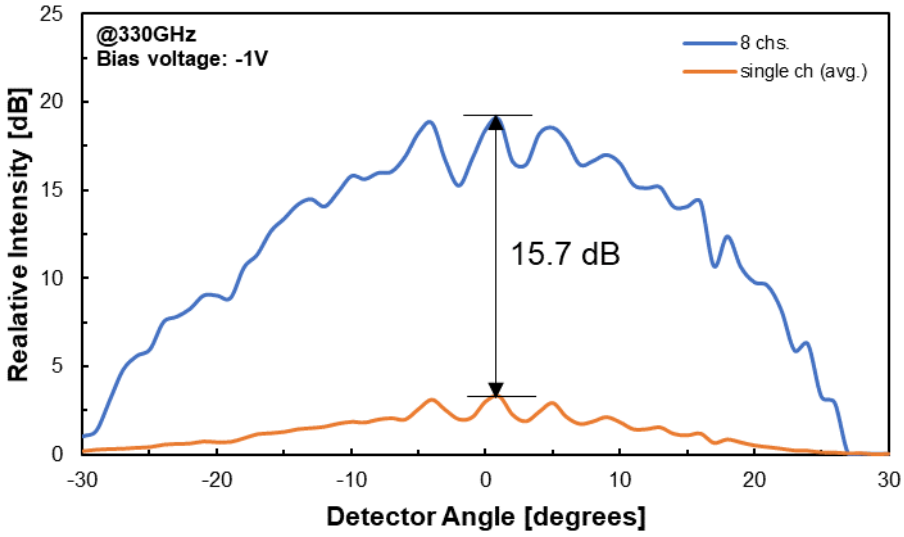

Figure 5.79: 8 × 1 coupled Wilkinson combiner integrated device radiation pattern.

5.4 DEVICE APPLICATION IN WIRELESS DATA TRANSMISSION

In this section, an account is given on the device application in wireless data transmission using two devices; a 4 × 1 T-junction combiner and a 2 × 1 Wilkinson combiner.

5.4.1 4 by 1 T-junction Combiner Integrated Device

Figure 5.33 illustrates the configuration of the data transmission experiment. A 300 GHz carrier signal is generated by photomixing using two laser diodes (LD1 and LD2) of 193.4 THz and 193.1 THz, an optical coupler, and the integrated UTC-PD and antenna device. An electro-optic modulator (EOM) modulates the two optical signals with a stream of NRZ data from a pulse pattern generator (PPG), hence leading to on-off keying (OOK) modulation scheme. The EDFA allows to control the optical power to the UTC-PDs thereby tuning the photocurrent and eventually the radiated THz wave power. The bias voltage in this experiment is kept at -1 V. The radiated THz wave by the antenna is detected by the FMBD equipped with two 25-mm aperture THz lenses that are 50 mm apart at 18 mm away from the FMBD and 32 mm away from the device and the bit error rate (BER) is measured by the bit error rate tester (BERT).

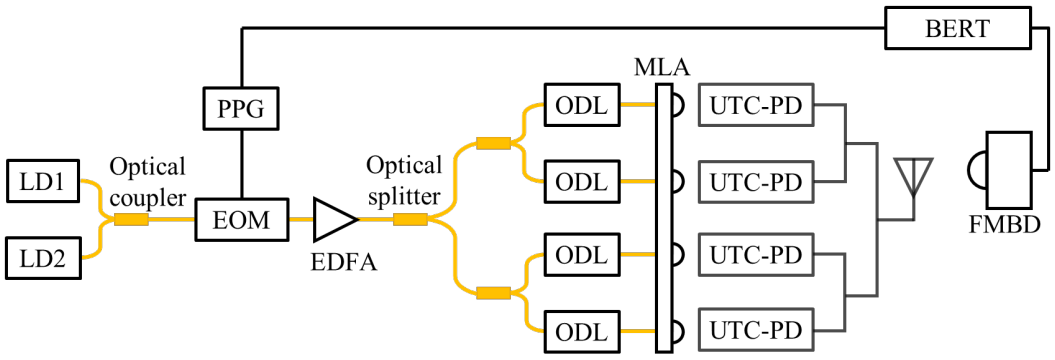

Figure 5.80: Data transmission experimental setup.

Data transmissions of 2 Gbps, 3 Gbps and 4 Gbps were conducted. The performance in terms of bit error rate (BER) against radiated power is given in figure 5.34. Bit error rates below the FEC (Forward Error Correction) requirement (10^{-3}) were successfully obtained for all the three data rates. The lowest BER for the highest data rate measured (4 Gbps) was in the order of (10^{-10}) with a photocurrent (I_{ph}) of 8 mA resulting in -24.7 dBm radiated power at -1 V bias voltage (V_{bias}). Additionally, an open eye diagram is obtained as shown in the inset of figure 5.34.

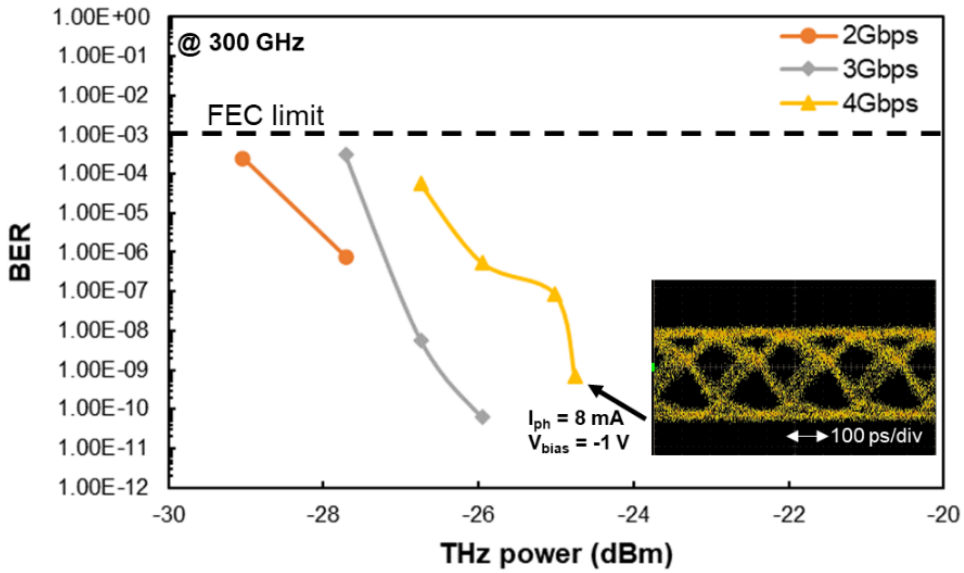

Figure 5.81: BER versus THz power for the 4 × 1 T-junction combiner integrated device.

5.4.2 2 by 1 Wilkinson Combiner Integrated Device

The same data transmission experimental set up shown in figure 5.33 was used for the 2 by 1 Wilkinson combiner integrated device except that two ODLs and two MLAs were used. Also, 285 GHz was used as the carrier frequency.

Data transmissions of 1 Gbps, 1.6 Gbps and 2 Gbps were conducted. The performance in terms of bit error rate (BER) against radiated power is given in figure 5.35.

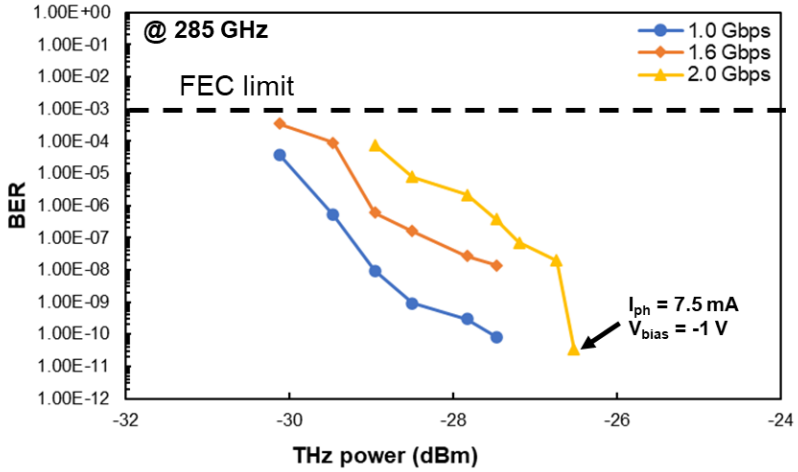

Figure 5.82: BER versus THz power for the 2 × 1 Wilkinson combiner integrated device.

Bit error rates below the FEC (Forward Error Correction) requirement (10^{-3}) were successfully obtained for all the three data rates. The lowest BER for the highest data rate measured (2 Gbps) was in the order of (10^{-11}) with a photocurrent (I_{ph}) of 7.5 mA resulting in -26.5 dBm radiated power at -1 V bias voltage (V_{bias}). From these results, it can be said that the proposed photonic emitter can find applications in high speed communications systems.

5.5 Conclusion

This chapter has given a thorough account on the fabrication and characterization of arrayed UTC-PDs integrated with a patch antenna and planar combiners on SiC substrate. This was to verify the concept of on-chip power combining for enhanced radiated THz power. The characterization involved assessing the performance of the fabricated T-junction and Wilkinson combiner, as well as the antenna co-design with 2 by 1, 4 by 1, and 8 by 1 configurations. It has

been experimentally demonstrated that if the phases of the photocurrents fed to the combiner are the same, they will be coherently combined by the planar integrated combiner and that if the photocurrent being fed to the antenna is multiplied by a factor of N, the radiated power will be enhanced byN^2.

Additionally, it has been shown from the experiment at 300 GHz that the device output is a function of electron velocity overshoot in the depletion layer of the UTC-PD that depends on an optimum bias voltage (-1 V) that corresponds to an optimal electric field. Furthermore, the UTC-PD output saturation is a function of space charge effect that is as a result of a critical charge density. The charge density modulates the field profile in the photodiode depletion region causing to a nonlinear response and device performance degradation. Moreover, measurement results have shown that the device exhibits multiple peaks that are a function of the antenna impedance a well as the UTC-PD impedance and they occur at frequencies when the antenna impedance is a conjugate of the UTC-PD impedance. Lastly, the chapter has demonstrated up to 4 Gbps data transmission rate with a 4×1 T-junction combiner integrated device and 2 Gbps for a 2×1 Wilkinson combiner integrated device depicting potential application of the developed devices in wireless communication systems.

REFERENCES

[1] H. Ito, T. Ishibashi, “InP/InGaAs fermi-level managed barrier diode for broadband and low-noise terahertz-wave detection,” Jpn. J. Appl. Phys., vol. 56, 2016.

[2] H. Ito, T. Ishibashi, “Novel Fermi-level managed barrier diode for broadband and sensitive terahertz-wave detection,” in Proceedings of the 40th International Conference on Infrared, Millimeter, and Terahertz waves (IRMMW-THz), Hong Kong, China, 23-28 August 2015.

[3] H. Ito, T. Ishibashi, “Fermi-level managed barrier diode for broadband and low-noise terahertz-wave detection,” Electron. Lett., vol. 51 2015.

[4] M. Natrella, C-P. Liu, C. Graham, F. Van Dijk, H. Liu, C. C. Renaud, and A. J. Seeds, “Modelling and measurement of the absolute level of power radiated by antenna integrated THz UTC photodiodes,” Opt. Express 24, 11793-11807 2016.

[5] C. C. Renaud, M. Natrella, C. Graham, J. Seddon, F. Van Dijk and A. J. Seeds, “Antenna Integrated THz Uni-Traveling Carrier Photodiodes,” IEEE Journal of Selected Topics in Quantum Electronics, vol. 24, no. 2, pp. 1.11, March-April 2018.

[6] J. Li, B. Xiong, C. Sun, D. Miao, and Y. Luo, “Analysis of frequency response of high power MUTC photodiodes based on photocurrent-dependent equivalent circuit model,” Opt. Express vol. 23, 21615-21623 2015.

[7] M. Grzeslo, C. Biurrun-Quel and A. Stöhr, “Impedance Modelling for High Frequency Unitraveling-Carrier Photodiodes,” in Proc. 2021 International Topical Meeting on Microwave Photonics (MWP), Pisa, Italy, 2021.

[8] T. Ishibashi, Y. Muramoto, T. Yoshimatsu, and H. Ito, “Uni-travelingcarrier photodiodes for terahertz applications,” IEEE J. Sel. Topics Quantum Electron., vol. 20, no. 6, Nov./Dec. 2014.

[9] T. Ishibashi and H. Ito, “Uni-traveling-carrier photodiodes,” J. Appl. Phys., 127, 2020.

CHAPTER 6

CONCLUSION

6.1 SUMMARY OF FINDINGS

This thesis has investigated the integration of arrayed Uni-traveling Carrier Photodiodes (UTC-PDs) with microstrip planar combiners, focusing on the conventional and coupled line Wilkinson Combiner as well as the T-Junction combiner, to enhance the power of emitted Terahertz (THz) waves. By combining photocurrents from multiple UTC-PDs, the research aimed to overcome the power limitations of single UTC-PDs. Extensive design, simulation, fabrication, and characterization demonstrated the potential of microstrip line-based combiners and patch antennas, leading to several key advancements and findings. This chapter summarizes our findings, implications, and potential future directions for this research area.

1. Power Enhancement by Photocurrent Combining

This research successfully demonstrated that combining photocurrents from multiple UTC-PDs using microstrip planar combiners significantly increases the overall photocurrent, leading to higher emitted THz power. Specifically, it was observed that increasing the number of UTC-PDs by n factor, increased the radiated THz power proportionally to the square of the number of combined UTC-PDs (n^2). Table 6.1 summarizes the performance of each fabricated device in terms of power increase relative to a single UTC-PD. The T-junction combiner integrated device proved to be more efficient than the Wilkinson combiner integrated device.

Table 6.1: Device performance in terms of power increase relative to a single UTC-PD

Antenna Integrated Device	Power increase in dB
2 × 1 T-junction	5.8
4 × 1 T-junction	11.3
8 × 1 T-junction	16.4
2 × 1 conventional Wilkinson	n/a
4 × 1 conventional Wilkinson	11
8 × 1 coupled line Wilkinson	15.7

The measured absolute power of the devices was in the μW range. This relatively low power can be attributed to losses within the measurement setup, particularly on the receiver side, and the low directivity of the antenna, which causes power to scatter over a broader area, resulting in low power being captured by the receiver. Although the output power for the on chip power combining technology reported in this work is still insufficient for practical transmission distances that requires milliwatt power levels, this technology presents a holistic and cutting edge platform for further power multiplication by further increasing the number of arrayed UTC-PDs which is promising for realizing the required power levels for practical wireless communication.

2. Device Characteristics

i) Frequency response

This thesis has elaborated that the frequency response of an antenna integrated UTC-PD device is a function of the impedance matching between the UTC-PD and the antenna. Thus, to optimize the antenna and planar combiners, it's imperative to ascertain the impedance of the UTC-PD. This is because the emitted power of an antenna is influenced by the efficiency of energy coupling with the driving source (UTC-PD) and the radiation efficiency. The former refers to the proportion of power provided by the source that is effectively utilized by the antenna, while the latter determines the proportion of power received by the antenna that is transmitted into free space. On the other hand, the antenna directivity describes the distribution of power in different angles when it is radiated. The optimal transfer of power between the source and antenna occurs when the impedance of the antenna is equal to the complex conjugate of the source impedance. Eventually, we can anticipate local peaks in the radiated power at frequencies where the reactance of the source and antenna have similar absolute values but opposite signs, and the real parts of their impedances are comparable.

ii) Biasing voltage effect on UTC-PD performance

The research has demonstrated that the UTC-PD output is a function of the electron velocity overshoot effect, that is sensitive to the electric field intensity whereby a certain range of electric field intensities within the depletion layer can cause electrons to exceed their saturation velocity which affects the response of the UTC-PD, which is determined by the carrier transit time,

thereby affecting the output. Hence there is an optimum bias voltage (-1 V for the device used in this work) that gives this field intensity below and beyond which the device performance degrades.

iii) UTC-PD Output Saturation

Furthermore, this thesis has demonstrated that the output linearity of the UTC-PD depends on the space charge effect whereby with increasing photocurrent, the current density increases in the depletion layer until it reaches a critical value J_{max} that modulates the field profile therein causing a non-linear response and output saturation. For the device used in this work, the space charge effect was realized at 10 mA.

iv) Fabrication of UTC-PDs on SiC Substrate

The UTC-PDs were successfully fabricated on a silicon carbide (SiC) substrate due to its superior thermal conductivity compared to the traditional indium phosphide (InP) substrate. This choice significantly mitigated thermal issues, enabling higher output photocurrents.

3. Applications in Wireless Communication

The potential application of the developed devices in wireless communication systems have been explored. The enhanced THz power output achieved through the proposed combining technique can facilitate the development of high-capacity, high-speed wireless communication networks. This research has demonstrated up to 4 Gbps data transmission rate with a 4×1 T-junction combiner integrated device and 2 Gbps for a 2×1 Wilkinson combiner integrated device.

6.2 RESEARCH IMPLICATIONS

The findings from this research have several important implications for the field of THz wave generation and its applications:

1. Enhanced THz Wave Emitters

The developed UTC-PD-based THz wave emitters with integrated microstrip combiners present a viable solution for generating higher power THz waves. This advancement is crucial for applications requiring high-power THz sources, such as wireless communication. The

demonstrated power enhancement through photocurrent combining offers a scalable and efficient solution for increasing THz power output, which is critical for overcoming the inherent power limitations of conventional single UTC-PDs. The integration of microstrip planar combiners and a patch antenna with UTC-PDs on the same substrate represents a step forward in developing compact, high-performance THz optoelectronic devices.

2. Thermal Management Solution

The successful fabrication of UTC-PDs on SiC substrate highlights a promising approach to thermal management in high-power photonic devices which paves the way for the development of more robust and efficient photonic devices where thermal dissipation is a critical concern.
The enhanced thermal management capabilities provided by SiC can lead to longer device lifetimes and better reliability, which are critical factors for practical applications.

3. Compact and Scalable Designs

The microstrip line transmission technology used in this thesis offers a compact and scalable solution for power combining. This characteristic is advantageous for developing portable and integrated THz systems, facilitating their adoption in various practical applications.

6.3 FUTURE WORK

While this thesis has made significant strides in improving the performance of UTC-PD-based THz emitters, several avenues for future research remain:

1. Optimization of Combiner Designs

Further optimization and use of different geometries for the power combiner designs can be explored to enhance efficiency and reduce losses.

2. Impedance matching

For optimal power transfer from the UTC-PD to the microstrip lines, impedance matching circuits or stubs can be integrated. This would require knowledge of the source (UTC-PD)

impedance so that the impedance matching circuits can realize complex-conjugate matching between the combiner-antenna design and the UTC-PD.

3. Integration with Advanced Antennas

Integrating the combined UTC-PD structures with advanced antenna designs, such as phased array antennas or meta-surface-based antennas, could enhance the directivity and gain of the emitted THz waves.

4. Integration with Other Photonic Components

Integrating the enhanced THz emitters with other photonic components, such as optical sources, couplers and splitters, modulators, and amplifiers, could pave the way for developing fully integrated THz communication systems. This integration would enhance the overall system performance and enable new applications in high-speed wireless communications.

5. Exploration of Alternative Substrates

While SiC proved to be effective in our research, exploring other substrates with superior thermal and electrical properties could further enhance the performance of THz photonic devices. Materials like diamond or graphene might offer additional benefits for specific applications.

In conclusion, this thesis has demonstrated the feasibility and effectiveness of using microstrip planar combiners and patch antennas to enhance the power of emitted THz waves from arrayed UTC-PDs. The integration of these components on SiC substrates addresses the key challenges of power combining and thermal management, paving the way for the development of high-power THz photonic devices. The findings contribute to the advancement of THz communication technologies and provide a foundation for future research in this rapidly evolving field. As we continue to explore and optimize these technologies, the potential for transformative impacts on wireless communications and other applications becomes increasingly apparent.

LIST OF PUBLICATIONS

A) Journals

1. **H. Ssali**, Y. Kamiura, R. Doi, H. Agemori, M. Che, Y. Mikami and K. Kato, "THz Wave Power Enhancement Using a Microstrip Line-based Combiner Integrated with Arrayed UTC-PDs." Electronics 2024, 13(13), 2661, doi: 10.3390/electronics13132661.
2. **H. Ssali**, Y. Kamiura, R. Doi, H. Agemori, M. Che, Y. Mikami and K. Kato, "Terahertz Wave Power Multiplication by Combining Photocurrents From Arrayed UTC-PDs." International Journal of High Speed Electronics and Systems, 2024, doi:10.1142/S0129156424400251.
3. Y. Kamiura, **H. Ssali**, R. Doi, H. Agemori, M. Che, Y. Mikami and K. Kato, "Terahertz power enhancement by combining photocurrent from arrayed UTC-PDs using Wilkinson power combiner." Japanese Journal of Applied Physics (Special Issues), 63(4), 2024, doi: 10.35848/1347-4065/ad37c4.

B) Conference Proceedings

4. **H. Ssali,** M. Che and K. Kato, "300-GHz-Band Power Combiner-Radiator Complex Designed for Arrayed Photomixers." 2023 XXXVth General Assembly and Scientific Symposium of the International Union of Radio Science (URSI GASS), Sapporo, Japan, 2023, doi: 10.23919/URSIGASS57860.2023.10265384.
5. **H. Ssali,** M. Che and K. Kato, "Coupled Line Wilkinson Combiner-Antenna Integrated Design for 300-GHz Arrayed UTC-PDs." 2023 Opto-Electronics and Communications Conference (OECC), Shanghai, China, 2023, pp. 548-551, doi: 10.1109/OECC56963.2023.10209621.
6. **H. Ssali** and K. Kato, "Terahertz Wave Power Enhancement Using T-Junction Connected UTC-PDs on SiC Substrate." 10th International Symposium on Terahertz-Related Devices and Technologies (TeraTech), Aizu-Wakamatsu, Japan, 2023, pp. 114-115.
7. **H. Ssali,** M. Che and K. Kato, "Performance Analysis of a Wilkinson Power Combiner-Fed Patch Antenna for 300-GHz Arrayed Photomixers." 2022 10th International Japan-Africa Conference on Electronics, Communications, and Computations (JAC-ECC), Alexandria, Egypt, 2022, pp. 202-205, doi: 10.1109/JAC-ECC56395.2022.10043902.
8. Y. Kamiura, **H. Ssali,** H. Agemori, R. Doi, M. Che, Y. Mikami and K. Kato, "Design and Evaluation of On-Chip Terahertz Wave Power Combiner for Beyond 5G/6G." 2024 International Conference on Electronics Packaging (ICEP), Toyama, Japan, 2024, pp. 261-262, doi:10.23919/ICEP61562.2024.10535617.
9. Y. Kamiura, **H. Ssali,** H. Agemori, R. Doi, Y. Mikami and K. Kato, "Novel terahertz wave power combining technique by arrayed photomixers." 2023 28th Microoptics Conference (MOC), Miyazaki, Japan, 2023, pp. 269-270, doi: 10.23919/MOC58607.2023.10302740.